PIEZOCERAMIC INDUCED STRAIN ACTUATION OF ONE- AND TWO-DIMENSIONAL STRUCTURES

by

Eric Harold Anderson

S.B., Aeronautics and Astronautics
Massachusetts Institute of Technology
(1986)

Submitted to the Department of Aeronautics and Astronautics
in partial fulfillment of
the requirements for the degree of
Master of Science in Aeronautics and Astronautics

at the

Massachusetts Institute of Technology
June 1989

Signature of Author_____
Department of Aeronautics and Astronautics
April 28, 1989

Certified by_____
Prof. Edward F. Crawley
Thesis Supervisor

Accepted by_____
Prof. Harold Y. Wachman
Chairman, Department Graduate Committee

Piezcceramic Induced Strain Actuation of One- and Two-Dimensional Structures

by

Eric Harold Anderson

Submitted to the Department of Aeronautics and Astronautics
on April 28, 1989 in partial fulfillment of
the requirements for the degree of
Master of Science in Aeronautics and Astronautics

ABSTRACT

Techniques for modeling induced strain actuation of beam- and plate-like components of intelligent structures are developed. The specific characteristics of one type of induced strain actuator, piezoceramic materials, are discussed, and implications for practical use of piezoceramic actuators are outlined. The presentation is based on a series of tests conducted to characterize piezoceramic actuation strain. Two analytical models and one numerical model describing the detailed mechanics of general induced strain actuators bonded to and embedded in one-dimensional structures are presented. The models illustrate the extension, bending, and localized shearing deformations induced. The range of parameters for which the simpler analytical models are valid is established, based on finite element models and experimental results. The one-dimensional models are extended to two-dimensional structures. Integration of induced strain actuation with laminated plate theory is illustrated. A general model for two-dimensional plate structures is formulated in terms of energy expressions. An approximate Rayleigh-Ritz model, based on the energy formulation, is used in conjunction with experimental results to verify the two-dimensional model.

Thesis Supervisor: Edward F. Crawley
Associate Professor, Department of Aeronautics and Astronautics

ACKNOWLEDGEMENTS

I would like to thank NASA and the National Science Foundation for their generous support of this research. I am also grateful to the Department of Aeronautics and Astronautics for providing me with a fellowship covering my first year of graduate study. I extend special thanks to Professor Ed Crawley for his steady direction, sage advice, and, during one phase of the research, his able assistance in the laboratory. Thanks to my fellow graduate students in the Space Engineering Research Center for making it an enjoyable place to work. I greatly appreciate the laboratory aid provided by Kevin Tow and Shawn Birchenough. Finally, I would like to thank my parents, whose nurturing and enduring support has allowed me to progress this far.

TABLE OF CONTENTS

LIST OF FIGURES

LIST OF TABLES

CHAPTER ONE: INTRODUCTION

One possible approach tc controlling structural deformation is to incorporate into the structure distinct elements in which strain can be regulated. The strain component which can be regulated will be defined the actuation strain, *i.e.*, that component of the strain due to stimulus other than mechanical stress. Actuation strain occurs in piezoelectric materials (Forward and Swigert, 1981, Hanagud *et al.*, 1987, and Burke and Hubbard, 1987), electrostrictive materials (Uchino, 1986, and Cross, *et al.*, 1987), magnetostrictive materials (Butler, 1988), shape-memory metal alloys (Schetky, 1979, Shimizu, *et al.*, 1986, and Rogers, 1989), and thermally controllable materials (Edberg, 1987). It is possible to model the constitutive properties of these materials by incorporating into the constitutive equations a generalized actuation strain, which will be denoted Λ. The total strain is

$$\varepsilon = \varepsilon_m + \Lambda \tag{1.1}$$

(total strain = mechanical strain + actuation strain)

When a material in which actuation strain can be regulated is coupled to a structure, the induced strain which results in the structure can be modeled irrespective of the details of the actuation strain mechanism.

The study of induced strain actuation is driven by an increasing number of applications involving control of flexible structures and an increasing emphasis on control/structures interaction. In a rational controlled structure design, the inherent dependence of the control system on the structural configuration is recognized early in the design process. The traditional types of actuators normally conceived of or used for active structural control (proof-mass dampers, gas jets) are however not integrated with the structure. They are separate elements attached after construction, which may change overall structural properties such as frequencies and mode shapes. In contrast, induced strain actuators may be built into the structure. Induced strain actuators are appealing, because they directly influence the strains, curvatures, and strain energy of the structure.

The potential applications for induced strain actuators include their use as the highly distributed actuators in *intelligent structures* (Crawley, *et al.* 1988). With such distributed actuators, it is possible to design structures with intrinsic vibration and shape control capabilities. A highly distributed network of actuators, sensors, and microprocessors allows a structure to be reconfigured to meet various requirements. This provides the structure with the inherent capability to adjust to uncertainties or to compensate for partial failure.

With increasing use of induced strain actuators likely, it is necessary to address the unique structural and material issues associated with this form of actuator. In control applications it is desirable to have accurate models of the mechanics of induced strain actuation, as well as a realistic understanding of the limits in actuation strain which can be achieved with real materials. For a given thermal, electrical, magnetic, or other input to a material, the nature of the strain which results must be described with a high degree of certainty and perhaps linearity. This is both a material question and a structural and control one. Other structural issues include basic models of induced strain actuation, as well as concerns over the effect of the introduction of actuators on overall structural performance in terms of strength, stiffness, and longevity.

The objective of this study is to develop accurate detailed models of the interaction between induced strain actuators and one and two-dimensional structures to which they are bonded, or in which they are embedded. The models are derived so as to be expressed in terms of the generalized actuation strain and therefore to be applicable to any type of induced strain actuation. In addition, the detailed nature of the actuation strain of one commonly used type of induced strain actuator, piezoceramic material, will be presented.

The previous work on induced strain actuation is limited. However, this area is one of much current research. Of the known methods for accomplishing induced strain actuation, piezoelectric materials have been utilized most often. These materials convert electrical to mechanical energy and *vice versa*. In the linear piezoelectric relations, the electric charge generated is proportional to the imposed stress. Conversely, the piezoelectric actuation strain is directly proportional to the applied electric field. Thus, piezoelectrics, like other induced strain actuators, may be used as both sensors (Hzou and Pandita, 1987) and

actuators in beam (Fanson and Caughey, 1987), plate (Crawley and Lazarus, 1989) and truss (Hagood and Crawley, 1988) applications. Both piezoceramics and piezoelectric films have been used as sensors in structural vibration problems. Piezoceramics, particularly lead zirconate titanate (PZT), have most often been used in actuation applications.

Electrostrictive materials, which also produce strain due to electrical input, have been used less frequently. With an actuation strain approximately proportional to the square of the applied electric field, there is potential for high strains. Electrostrictive actuators have been developed, and this area is the subject of materials research which is likely to lead to more effective actuators in the near future (Uchino, 1986). Electrostrictive materials have some potentially undesirable temperature-dependent properties (Cross, 1980). Less well developed are actuation due to magnetostriction, shape memory alloys, and thermal gradients. Of these, shape memory alloys are capable of high actuation strains (up to 8%), but are limited in bandwidth, and require rapid heat dissipation for high bandwidth operation.

Piezoelectric materials have been used in applications other than as induced strain actuators for several decades. These include sonar transducers, phonograph pickups, tweeters for audio speakers, and accelerometers. In many of these applications, piezo*ceramics* have been utilized. In the earliest uses of piezoceramics, barium titanate, $BaTiO_3$, was employed most often. Lead zirconate titanate (PZT) is used in the majority of current applications. In addition, there is work underway to further develop piezoelectric-electrostrictive hybrid materials.

The moderately strong nonlinear behavior of piezoceramics, for example in the actuation strain due to an applied field, has been tolerated because of other inherent advantages. This behavior is not addressed in most studies which have used piezoceramic actuators. But the real piezoceramic behavior has been apparent to experimenters in the field (Berlincourt, *et al.*, 1964 and Jaffe, *et al.*, 1971). A few have attempted to model (Martin, 1974) or correct for that behavior (Newcomb and Flinn, 1982, Bryant and Keltie, 1986). A characterization of the nonlinearities allows for an improved understanding of piezoceramic actuation strain.

In this study, all structural models incorporating induced strain actuation are derived for general actuation strain. Experiments conducted in order to test the validity of the models were conducted using piezoceramics. This means of induced strain actuation was chosen because of material availability and ease of use. In order to properly integrate piezoceramics with structures it was necessary to characterize accurately the nature of the piezoelectric actuation strain. Thus, Chapter 2 contains a description of the traditional linear constitutive relations for piezoelectric and piezoceramic materials, and details the limits of these simple relations through a macromechanical study of the actuation strain. The results of a series of experiments illustrating the nonideal behavior of piezoceramics are presented. Implications of the real piezoceramic actuation strain characterization are discussed and practical guidelines for addressing the problems are outlined.

In Chapter 3, analytical and finite element models are developed for general induced strain actuation of one-dimensional structures. The results from the models of Crawley and de Luis (1987) are presented and compared to the results obtained for finite element and alternative analytical models. The real piezoceramic properties are used in analyzing experimental data from static and dynamic induced strain experiments on cantilevered beams. The comparison of the models and experimental results lead to the conclusion that a simple analytical model, coupled with an awareness of real piezoceramic behavior, is adequate for most applications where actuators are either embedded or surface mounted.

In Chapter 4, models are derived for induced strain actuation of two-dimensional structures (plates) for arbitrary laminates with actuators embedded or surface-mounted. Specialization to the one-dimensional models is demonstrated. An energy formulation and approximate solution technique are described. Models are again correlated with experimental results. Finally, the study is summarized, with guidelines developed for the use of simple or more complex models, incorporation of nonideal actuator strain, and recommendations for future study of induced strain actuation.

CHAPTER TWO: PIEZOCERAMIC ACTUATION STRAIN

2.0 INTRODUCTION

The physical effects which cause actuation strain may be based on piezoelectricity, electrostriction, magnetostriction, or thermoelasticity. However, while the method of inducing strain differs, all strain actuators share common mechanical features. This commonality allows for a general treatment of induced strain, presented in Chapters 3 and 4. In the current study, all experimental results are based on tests in which piezoelectric materials were used as actuators. The manner in which the physical property of piezoelectricity is harnessed to induce strain and the nonlinearities and nonidealities of that piezoelectric actuation strain are the focus of this chapter.

Piezoelectric properties are found in range of materials, including natural piezoelectric crystals, polymeric films, and ceramics. Piezoceramics (see note on material hierarchy in Appendix A) were used exclusively in the experiments conducted in this investigation. Some of the undesirable nonlinearities associated with the ceramics are not as prevalent in natural crystals. However, ceramics are much easier to shape and are commercially available in a convenient range of sizes. The relative sparseness of the piezoelectric electromechanical coupling matrix **d** (Section 2.1) is another advantage of ceramics over crystals. Ceramics were chosen over polymers because they can transfer more strain energy for a given field due to their relatively high modulus. While not critical in this study, piezoceramics also have a much higher Curie Point - the elevated temperature at which a material loses its ferroelectric properties. Crawley, *et al.* (1988) includes a more complete comparison of the relative merits of several piezoelectric materials.

In this chapter, some of the advantages and concerns associated with the use of piezoelectric ceramics as induced strain actuators are described. A macromechanical representation of piezoceramic properties is presented and the basic linear piezoelectric constitutive relations for piezoceramics are discussed. The remainder of the chapter is then devoted to discussion of "nonidealities" in piezoceramic actuation strain. If a field-strain relation which may be represented by a single constant is considered "ideal," departures from that may be described

by the general label "nonidealities." Experimental data indicate the presence of field-strain nonlinearities, hysteresis, and creep. Frequency dependence of the field-strain relationship is investigated. High field behavior and depoling are also discussed. In addition, the departure from isotropic inplane strain response and the effect of large mechanical strain on piezoelectric properties are documented. The chapter concludes with a discussion of the implications of the observed nonideal behavior for piezoceramic induced strain actuators.

2.1 MACROMECHANICAL MODEL OF PIEZOELECTRIC BEHAVIOR

Approaches to Characterization

There are several ways to characterize the constitutive behavior of piezoelectric materials and piezoelectric behavior. These include electrical, micromechanical, thermodynamic, and macromechanical approaches. Each has advantages that make it appropriate for different applications.

The first practical studies of piezoelectric crystals were carried out by electrical engineers, who used equivalent electrical circuit models to represent the piezoelectric properties. This method is still extensively employed in the electrical engineering community and elsewhere. It is the preferred way of characterizing piezoelectric behavior when the primary objective is to consider the influence of a piezoelectric on an electrical system. The approach was not used in this study because the primary concern is with mechanical effects. When dealing with piezoelectricity, electrical effects must be addressed, but appropriate mechanical models which implicitly incorporate accurate dielectrical models can be used instead of a full electrical representation. Appendix B contains a description of some common electrical circuit and impedance models.

A second approach takes a materials science or micromechanical perspective. The chemical composition and microstructure of the material are studied. Such a micromechanical view of piezoelectric crystals has been taken by crystallographers and materials scientists. This approach is primarily applicable in the development of new and better materials where, for example, a small amount of another element or compound is added to the common piezoceramic lead zirconate titanate (PZT) to achieve a desired effect. The material mechanism of poling a ceramic so it gains a permanent polarization and thus acquires

piezoelectric properties is a fundamental process for all piezoceramics. Micromechanics provides insight on poling and depoling, as well as on possible material loss mechanisms. In general, however, micromechanics is usually not of primary concern to a structural or control engineer because the information provided about the mechanics of the material is too detailed.

A third method involves the use of thermodynamic state formulation (see Appendix C). This method is general and can easily incorporate mechanical, electrical, thermal, magnetic, and other effects in materials and systems. The thermodynamic description is especially useful in representing interactions between physical effects as well as in determining appropriate boundary conditions for the solution of compiex coupled problems. While it has been and continues to be employed in many theoretical studies (Tiersten, 1969 and Adam, *et al.*, 1988), it sometimes unnecessarily complicates relatively simple problems. When one set of physical effects is of primary concern, a less general approach can be substituted.

The fourth approach, and the one taken in this study, is a macromechanical one. It is a simplification and linearization of the thermodynamic approach. A proper macromechanical model is sufficiently general because it incorporates electrical effects and sufficiently specific because mechanical behavior is clearly highlighted. This is the most useful way of studying general induced strain actuation because it is concerned primarily with and formulated in terms of mechanical quantities such as strain. If a model of the behavior of piezoelectric materials is macromechanical, the mechanical interaction between a piezoelectric and a structure, including the strain induced in the structure by the piezoelectrics, can be described easily. The macromechanical approach will be developed in the remainder of the chapter.

Piezoelectric Constitutive Relations

In this section, the mechanical and electrical variables relevant in the macromechanical study of piezoelectricity will be presented. The general linear relationships between those variables, termed the "piezoelectric constitutive relations," will be shown, and specialized to the case of piezoceramics. The piezoceramic constitutive matrix will then be discussed and important features of the matrix will be highlighted.

The macromechanical description of piezoceramic behavior begins with the four quantities of concern in piezoelectricity. There are two mechanical and two electrical variables involved in the characterization. The mechanical variables are stress (T) and strain (S) and the electrical are field (E) and electric displacement (D). Electric displacement is sometimes called "electric flux density." It is a vector with direction which, on the flat surface of a dielectric material, may be thought of as the charge density. Stress and strain are second order tensors, while field and electric displacement are first order.

When there is no electromechanical coupling, the electrical (or dielectric) and mechanical problems are uncoupled. In the mechanical problem, stress and strain are related by the elastic modulus or stiffness matrix ($\mathbf{c}$) or, its inverse the elastic compliance matrix ($\mathbf{s}$). In the electrical problem, the electric field and displacement are related by the permittivity or dielectric matrix (ε) or its inverse the impermittivity matrix (β)

$$\begin{aligned} \mathbf{T} &= \mathbf{c}\,\mathbf{S} \\ \mathbf{E} &= \beta\mathbf{D} \end{aligned} \quad \text{or} \quad \begin{aligned} \mathbf{S} &= \mathbf{s}\,\mathbf{T} \\ \mathbf{D} &= \varepsilon\,\mathbf{E} \end{aligned} \tag{2.1}$$

Piezoelectricity connects the mechanical and electrical problems. The coupled electromechanical constitutive relations for a piezoelectric are

$$\begin{aligned} \mathbf{D} &= \varepsilon^{\mathbf{T}}\,\mathbf{E} + \mathbf{d}\,\mathbf{T} \\ \mathbf{S} &= \mathbf{d}'\,\mathbf{E} + \mathbf{s}^{\mathbf{E}}\,\mathbf{T} \end{aligned} \tag{2.2}$$

These are just the uncoupled relation from (2.1) with the piezoelectric coupling terms $\mathbf{d}$ and $\mathbf{d}'$ added. The $(\,)'$ indicates transpose. The superscripts T and E signify that these are quantities taken at constant (or zero) stress (also known as "free") and constant (or zero) field (also known as "short circuit"). In the uncoupled mechanics problem, there is no distinction between the short and open circuit compliances or stiffnesses. Similarly, in the uncoupled dielectric problem, there is no difference between clamped and free permittivity or impermitivitty. However, it is important to include these qualifications when a problem is electromechanically coupled.

Equation 2.2 is one of four possible ways of representing the coupling between the four variables of interest. The format for writing the relations depends on which two variables are considered independent and which two are

considered dependent. There are four possible forms of the equations and therefore four piezoelectric coefficient matrices (**d**,**e**,**g**,**h**). Likewise, there are two forms of the mechanical (**c**,**s**), and two forms of the electrical (ε,β) coefficients. Appendix C presents the various arrangements of electromechanical coupling in tensor form and details the relationship between the piezoelectric, mechanical, and dielectric coefficients. The focus in this study is on **d**, which relates strain to applied field and is therefore most relevant in induced strain actuation. A high **d** coefficient implies a larger amount of strain per field can be achieved.

Constitutive Relations Specialized to Piezoceramics

For the special case of a piezoceramic, the full matrices for the form of the constitutive equations in Eq. 2.2 are

$$\begin{bmatrix} D_1 \\ D_2 \\ D_3 \\ S_1 \\ S_2 \\ S_3 \\ S_4 \\ S_5 \\ S_6 \end{bmatrix} = \begin{bmatrix} \varepsilon_1^T & 0 & 0 & 0 & 0 & 0 & 0 & d_{15} & 0 \\ 0 & \varepsilon_1^T & 0 & 0 & 0 & 0 & d_{15} & 0 & 0 \\ 0 & 0 & \varepsilon_3^T & d_{31} & d_{31} & d_{33} & 0 & 0 & 0 \\ 0 & 0 & d_{31} & s_{11}^E & s_{12}^E & s_{13}^E & 0 & 0 & 0 \\ 0 & 0 & d_{31} & s_{12}^E & s_{11}^E & s_{13}^E & 0 & 0 & 0 \\ 0 & 0 & d_{33} & s_{13}^E & s_{13}^E & s_{33}^E & 0 & 0 & 0 \\ 0 & d_{15} & 0 & 0 & 0 & 0 & s_{55}^E & 0 & 0 \\ d_{15} & 0 & 0 & 0 & 0 & 0 & 0 & s_{55}^E & 0 \\ 0 & 0 & 0 & 0 & 0 & 0 & 0 & 0 & s_{66}^E \end{bmatrix} \begin{bmatrix} E_1 \\ E_2 \\ E_3 \\ T_1 \\ T_2 \\ T_3 \\ T_4 \\ T_5 \\ T_6 \end{bmatrix} \tag{2.3}$$

where the 9x9 matrix is a block matrix made up of ε^T, **d**, **d'**, and $\mathbf{s}^E$, and field and stress are put on the right hand side as the independent variables. The condensed notation for stress, strain, and compliance, with subscripts 1-6 is used.

The constitutive matrix in Eq. 2.3 contains a great deal of information. It is worth discussing in more detail some of the significant points. Figure 2.1 defines the coordinate system used in defining the entries in the matrix above and in the discussion which follows.

First, the x_3 axis is assigned to the direction of the initial polarization of the piezoceramic. The x_1 and x_2 axes are arbitrarily defined in the plane

perpendicular to the x_3 direction. In an actual specimen, the x_1 and x_2 directions are usually defined so they align with the principal or physical axes of symmetry of the manufactured ceramic.

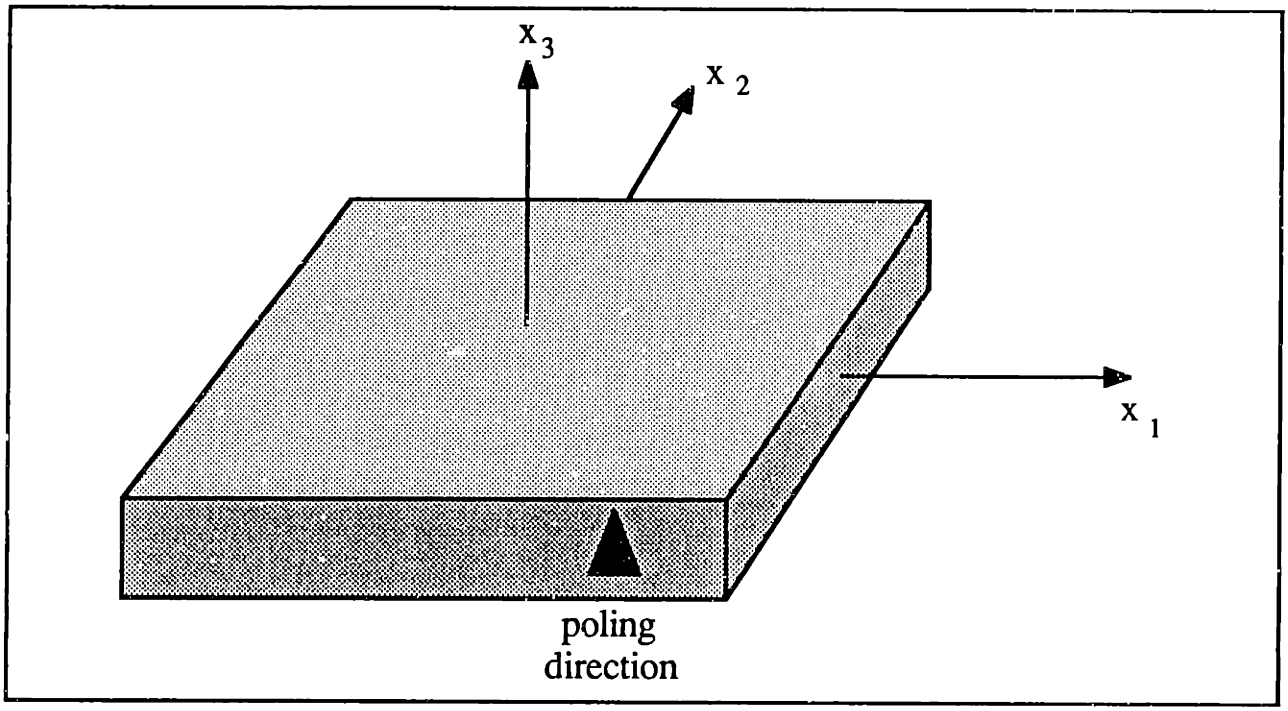

Figure 2.1: Coordinate System for Piezoceramics

Second, there are three dielectric and six mechanical variables. The '1,' '2,' and '3' subscripts correspond to properties along the x_1, x_2, and x_3 axes. The '4,' '5,' and '6' subscripts correspond to shear properties in the x_2-x_3, x_3-x_1, and x_1-x_2 planes (Jones, 1975). The mechanical part of the problem includes shear coupling. There is no analogous behavior with the dielectric variables. In fact, the dielectric matrix block ε^T is diagonal, indicating that there is no dielectrical coupling between properties in different directions.

It is a convention in the piezoelectric matrices, including the **d** matrix, to write the subscript corresponding to the electrical variable first. This convention is based on the more common reference to the *direct* piezoelectric effect, as the electric charge developed upon application of a mechanical stress. In induced strain applications, the less commonly utilized *converse* effect, in which a mechanical strain is developed due to an applied electric field, is important. By common convention the strain in x_1 due to field in x_3 is written

$$S_1 \propto d_{31} E_3 \quad \text{not} \quad S_1 \propto d_{13} E_3 \tag{2.4}$$

Ideally, piezoceramics are transversely isotropic with respect to electrical, mechanical, and piezoelectric properties. That is, the properties are modeled as being identical in any direction in the x_1-x_2 plane. Prior to polarization, the ceramic is completely isotropic. The process of poling distinguishes the x_3 direction from the others. Because of the transverse isotropy, the subscripts '1' and '5' are substituted for '2' and '4.' Shear strain in the x_1-x_2 plane, perpendicular to the x_3 poling direction (S_6), cannot be piezoelectrically induced in a piezoceramic.

As a result of these features, there are only 10 independent material coefficients (2 electrical, 5 elastic, and 3 piezoelectric) listed in the 9×9 matrix of Eq. 2.3. Six compliances are listed, but for a transversely isotropic material, there is one additional constraint

$$s_{66} = 2(s_{11} - s_{12}) \tag{2.5}$$

The matrix is sparsely populated compared to constitutive matrices for some natural piezoelectric crystals. This feature is a desirable one. The degree of coupling between strains, for example, adds to the complexity when a model of piezoelectric strain actuators as part of a larger structure is constructed.

Thus far, the basic framework of the linear macromechanical model has been presented. The format necessary to describe any linear electromechanically coupled problem is contained in Eq. 2.3. We now focus briefly on the specific part of the piezoelectric coefficient matrix most relevant to induced strain actuation - the strain-field relation contained in the **d** matrix block.

Piezoelectric Strain Coefficients

Because of the symmetries inherent in a piezoceramic, there are only three independent coefficients in the **d** matrix. As a group, d_{33}, d_{31}, and d_{15} are often termed "piezoelectric strain coefficients." There are no commonly used descriptive terms for each of the coefficients. Occasionally, the words "longitudinal," "transverse," and "shear" are applied to the three respective strain coefficients. However, because these terms have other implications in mechanics, they will be avoided. Some typical numerical values of the d coefficients (reported in m/V) are given in Appendix D.

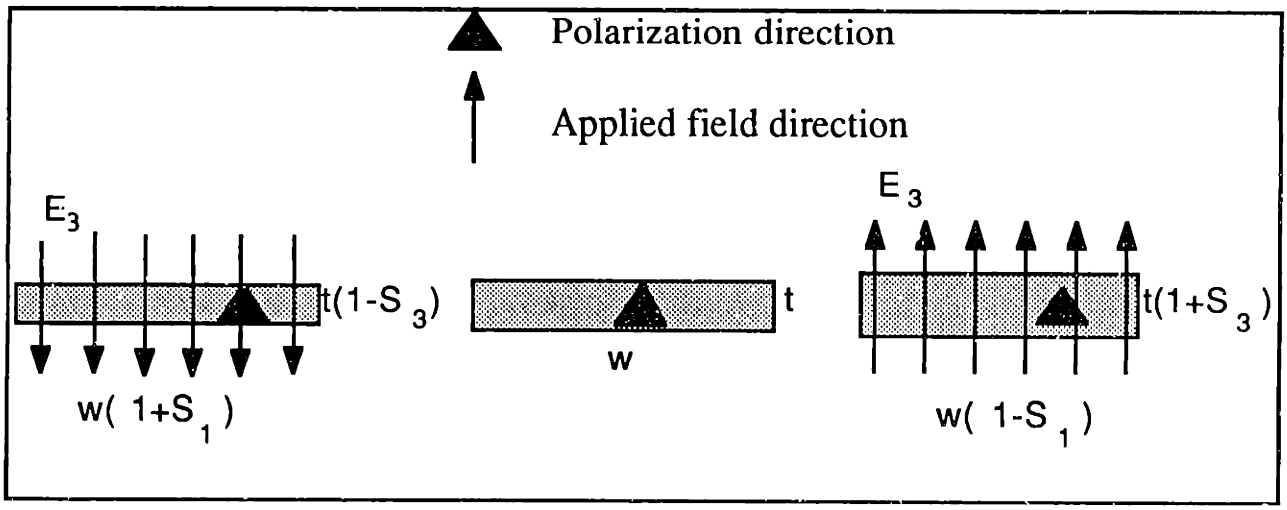

Figure 2.2: Illustration of d_{33} and d_{31} Coefficients

The coefficient with the most straightforward definition is d_{33}. When a field is applied parallel to the x_3 direction, the piezoceramic strains in that direction as well. Figure 2.2 illustrates the results of applied fields. Thin electrodes cover the top and bottom faces of the piezoceramics. When a voltage is applied across the two surfaces, the differential produces an electric field. The field is assumed to be constant between the two electrodes, and thus throughout the piezoceramic. A field aligned with the polarization direction gives a positive strain S_3. An opposite field of the same magnitude gives a compressive strain S_3. The total displacement is the strain multiplied by the thickness. The strain is defined by

$$\frac{\Delta t}{t} = d_{33}\frac{V_3}{t} \quad \text{or} \quad S_3 = d_{33}E_3 \tag{2.6}$$

The thickness of a single piezoceramic is limited by two concerns. First, the manufacturer must be able to initially polarize the ceramic. This requires a large field, typically at least 1000V/mm. Second, even if the manufacturer has the capability to apply large fields, in actual use it will still be necessary to apply fields nearly as high to obtain maximum strains from the ceramic. That may not be achievable or practical in an application. This motivates the use of stacked piezoceramics, in which a number of individual ceramic pieces are placed in a stack. Their displacements add, but when the individual ceramics are electrically connected in parallel, large fields are not necessary because the same voltage is applied across each component.

The d_{31} coefficient characterizes strain perpendicular to the poling direction (that is, in the x_1 and x_2 directions) due to an electric field (E_3) aligned with the poling (x_3) direction. It is often reported as a negative value because it is considered a secondary, Poisson-like effect which results when there is strain due to d_{33}. Under a positive E_3, there results a positive S_3 and negative S_1 and S_2. Figure 2.2 also shows the strain attributed to d_{31} as the piezoceramic thickness changes due to d_{33}. The strain in the x_1 (or x_2) direction is

$$\frac{-\Delta w}{w} = d_{31}\frac{V_3}{t} \quad \text{or} \quad S_1 = d_{31}E_3 \tag{2.7}$$

Just as with d_{33}, the displacements which can be obtained when d_{31} is used are relatively small. In order to amplify the effect of the strain in induced strain actuation, the piezoceramics are typically provided with a mechanical advantage. Figure 2.3 shows an arrangement used for inducing bending strain in beams and plates. By expanding one ceramic and contracting the other, bending can be induced in a structure. The actuators in the figure are shown mounted on the surface of the structure. They may also be embedded within it. By extending or contracting both ceramics, extensional strain can also be induced. In the case

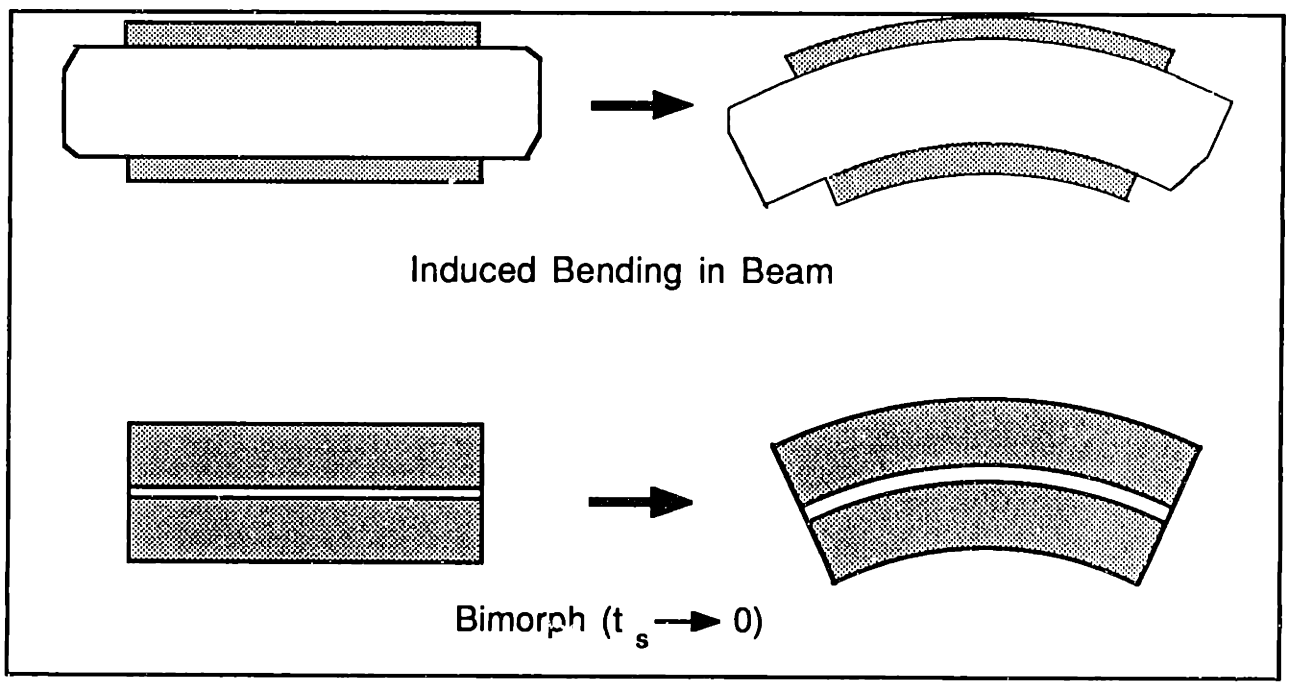

Figure 2.3: Induced Bending Using d_{31}Coefficient

where the thickness of the structure, t_s, approaches zero, the resulting actuator is called a "bimorph" or "bender." A bimorph consists of two flat sheet ceramics

separated by a thin metal shim. Typically, one end of the bimorph is clamped and the other left free, or both ends are pinned on hinges. A relatively large deflection of many times the thickness of the bimorph is possible with proper mounting. Bimorphs were used in a low frequency aeroelastic application by Spangler (1989).

The third piezoelectric strain coefficient, d_{15}, is the least utilized. The electrode faces used to pole the ceramic are not used for actuation. Instead, electrodes are placed on the other surfaces, perpendicular to the poling direction, and an electric field is applied in the x_1 or x_2 direction. Shear strains in the x_1-x_3 or x_2-x_3 plane result. Figure 2.4 shows the physical deformation due to d_{15}. The shear strain is

$$\frac{dx}{t} = d_{15}\frac{V_1}{t} \quad \text{or} \quad S_5 = d_{15}E_1 \tag{2.8}$$

The value of d_{15} is higher than d_{33} and d_{31}, but in order to induce large net displacements, a large voltage is required. This is particularly true of d_{15} use because a large polarization field must be applied initially during manufacture, then a large field must be applied to obtain a perpendicular strain. Thus, the overall size of the piezoceramic is severely limited. A stack of piezoceramic elements using d_{15} can increase the total displacement.

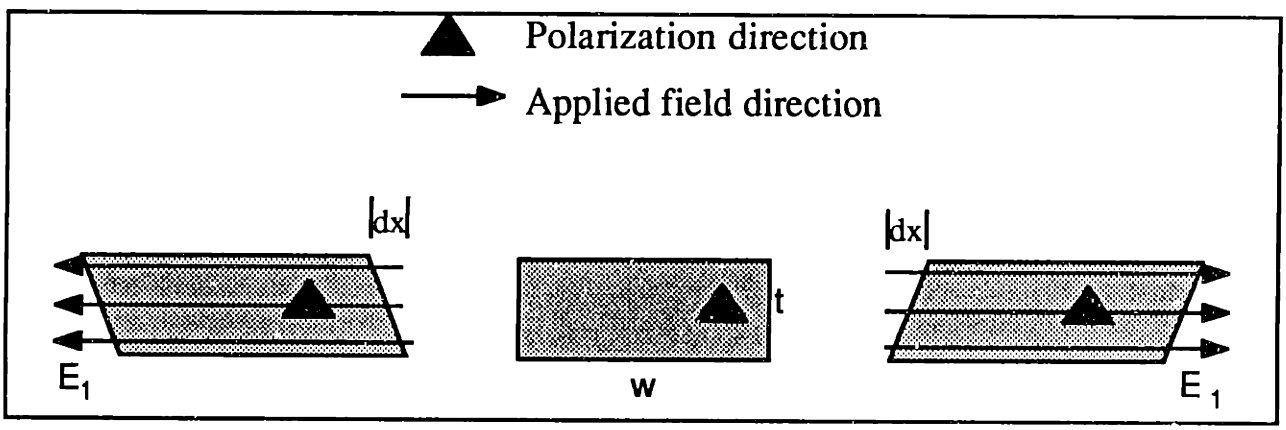

Figure 2.4: Illustration of d_{15} Coefficient

The basic equations of piezoelectric actuation have been described in linear macromechanical terms with important features highlighted. The piezoelectric strain coefficients have been described and some methods for amplifying the piezoelectric effect were noted. The remaining portion of this chapter will focus on quantifying the effects associated with the d_{31} coefficient and several features

not captured by the simple linear model where d_{31} is represented by a single constant will be presented.

2.2 STRAIN IN PIEZOCERAMICS

The behavior of piezoceramic materials, specifically the strain response to an applied field, departs from being ideal. Instead of modeling ideal performance and ignoring departures from it, it is important to address the nonidealities and examine them more carefully. The term "nonideality" is used here to refer to a broad range of phenomena in which the linear relationship (Eqs. 2.3 and 2.7) between two variables of interest (strain and field) cannot be represented by a single constant for all values of those variables. Some of the phenomena discussed may be termed nonlinearities. All are properties not represented by a single d_{31} constant.

After this brief introduction, the remaining portion of this chapter is organized as follows. One nonideality, such as the field-strain relation, will be introduced. A simple test to determine the degree of nonideality will be described and results presented. The results will then be analyzed for their significance. Then the next nonideality will be similarly treated. There are six separate properties addressed. These are: the basic field-strain relation; hysteresis; strain rate dependence and creep; depoling; orthotropic inplane response; and the effect on piezoceramic performance of imposed mechanical strain. When the nonidealities are characterized and understood, their relative importance and the limits they impose on the performance of the piezoceramics can be understood as well.

Most of the modeling presented in the literature on piezoelectrics makes use of simple linear models of behavior. In the *IEEE Standard on Piezoelectricity* (1978) and many earlier texts and articles (Mason, 1950, Cady, 1964, and Berlincourt, *et al.*, 1964) dealing with piezoelectrics the theoretical focus is mainly on piezoelectric *crystals*. Prior to the publication of the Standard, and since, a few authors have addressed some of the nonlinear behavior of piezoceramics. *Piezoelectric Ceramics* (Jaffe, *et al.*, 1971) presents some data which illustrate the real properties of all piezoceramics. Several have recognized the presence of some nonlinear relations and have employed a complex representation of mechanical, dielectric, and piezoelectric properties. A brief outline of that

modeling technique and its limits will be presented at the end of the section on hysteresis. In addition, the piezoceramic manufacturers have also characterized many nonidealities, to a somewhat greater extent.

Any careful research will discover the many previous references to these phenomena. In fact, the authors of the IEEE Standard were well aware of some departures from linear behavior exhibited by piezoceramics, but it was necessary to exclude these phenomena from their Standard. On page 1 of the Standard (IEEE, 1978) they state

> All results are based on linear piezoelectricity in which the elastic, piezoelectric, and dielectric coefficients are treated as constants independent of the magnitude and frequency of the applied mechanical stresses and electric fields.

In experimental study, the presence of nonidealities cannot be avoided. In any practical use the strict linear assumptions must be relaxed to accurately represent the realistic material behavior.

What follows is a report of real behavior of mainly one type of lead zirconate titanate (PZT) piezoceramic, G-1195, manufactured by Piezoelectric Products. The relative magnitude of the various properties varies depending on the specific piezoceramic used. However, the properties discussed here are believed to be representative.

2.2.1 Nonlinear Field-Strain Relation

The most basic nonlinearity of a free piezoceramic is in the relation between applied electric field and mechanical strain. In the linear theory, for a field applied in the x_3 direction to a stress-free piezoceramic, the strain in the x_1-x_2 plane is related to the field by the piezoelectric coefficient d_{31}

$$S_1 = d_{31} E_3 \tag{2.9}$$

If d_{31} were a constant, as the linear theory assumes, the field-strain relationship would be linear.

However, the actual relationship is not. It is an industry standard to report the single measure of d_{31} based on the IEEE Standard, which realistically covers a range of applied field only up to a less than 10 V/mm. But the single

value provided for d_{31} does not capture the full field-strain relationship over the entire range of applied field, often up to 1000V/mm or more.

A plot of the field vs. strain is analogous to the mechanical "stress-strain curve." Just as the mechanical relationship is determined by loading a specimen and measuring the stress and strain, the piezoelectric one is found by applying a known field and measuring the strain. For materials which are not perfectly elastic, a single modulus or compliance is not adequate to describe the stress-strain relationship. For real piezoceramic materials, field and strain are not related by a constant.

A set of field-strain tests was conducted to characterize the actual relationship of field to strain. The results are shown in Fig. 2.5. In the tests, a single piezoceramic plate, with silver-nickel electrodes completely covering its upper and lower faces, was placed on a electrically grounded aluminum jig plate. The x_1 and x_2 axes were defined in the same plane as the piezoceramic sheet. A single electrical connection was made with the top of the piezoceramic and an electric field (E_3) was applied across the PZT material. The field was assumed to be constant throughout the piezoceramic. It was further assumed that the piezoceramic was stress-free. The inplane strain in the x_1 direction was measured with a strain gage mounted on the upper surface. Unless otherwise noted, all tests were carried out on 63.5mm x 25.4mm x .254mm plates of G-1195 ceramics.

In plotting a field-strain curve, the directions of field and strain are defined in order to make d_{31} a positive quantity. This reduces confusion in presentation of the data and allows easy analogy to the stress-strain relation.

The field-strain behavior for different specimens of the same material was found to be nearly identical. Although a thorough statistical study was not done, the majority of the samples had curves which varied by a total of less than 5 percent in strain for a given field. Figure 2.5 shows the field-strain curve for a typical G-1195 piezoceramic with measurements taken at a frequency of 0.1Hz. Peak values of the field and strain are reported. The strain shown is referred to as the *actuation strain*, defined as the strain in response to an applied field when the material is not mechanically constrained and, therefore, is stress free. Field and strain values were recorded at each of the indicated data points and the data were fit with a cubic function shown. Also shown is the linear small-signal

model with a constant slope. The maximum field which may be applied limits the maximum strain and is governed by the value of the breakdown field. Breakdown will be discussed in the section on depoling (2.2.4). In this test, the maximum field used was roughly 90% of the breakdown value.

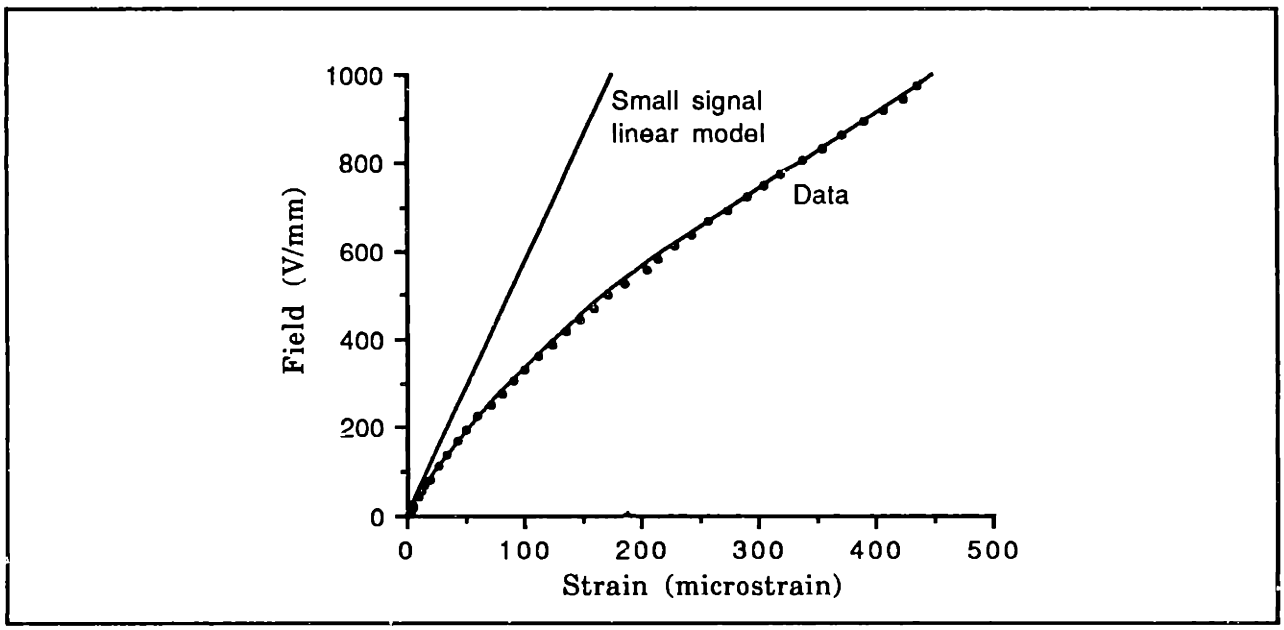

Figure 2.5: Field-Strain Curve (E_3 vs. S_1) for Unconstrained G-1195 (0.1Hz)

The field-strain plot for a piezoceramic is analogous to the stress-strain curve for a material which softens as stress (or strain) is increased. In this case, while the nonlinearity complicates modeling, simply extending the linear relation with constant d_{31} to higher fields could underestimate the strain achievable at higher fields by a factor of two or more. In induced strain actuation applications, this extra strain could be beneficial.

From Fig. 2.5, it is obvious that d_{31} is not in fact a constant. We therefore will use the symbol d^*_{31} to indicate that the coefficient can take on different values depending on the amplitude of the field and strain. The d^*_{31} coefficient is defined as the total strain divided by the total applied field. It is similar to the "secant compliance" in mechanics. A "tangent " d_{31} based on the local slope of the field-strain curve could also be defined. The definitions are written

$$\text{secant definition:} \qquad d^*_{31} \equiv \frac{S_1}{E_3}$$

tangent definition: $$\bar{d}_{31} \equiv \frac{\partial S_1}{\partial E_3} \tag{2.10}$$

The secant definition of d^*_{31} is used in this study.

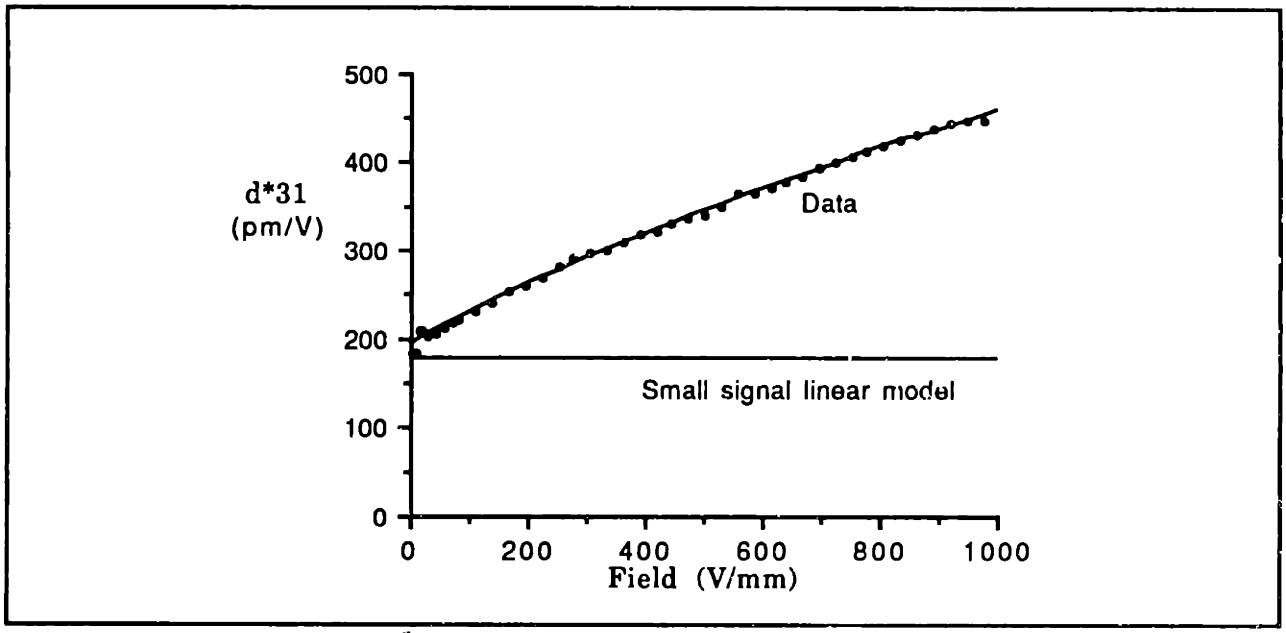

Figure 2.6: d^*_{31} vs. Field (E_3) for Uncontrained G-1195 (0.1Hz)

Figure 2.6 shows the d^*_{31} coefficient as a function of field. The d^*_{31} values were determined directly from the data in Fig. 2.5 then again fit with a cubic. For reference, the constant d_{31} of the small-signal linear model is shown.

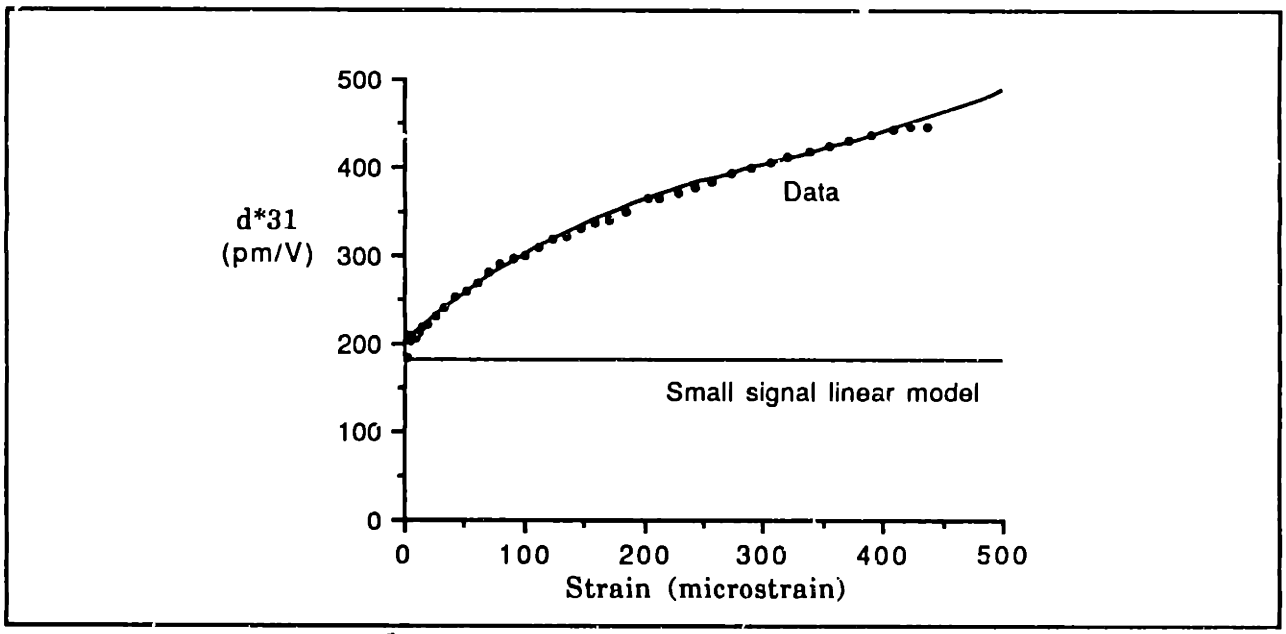

Figure 2.7: d^*_{31} vs. Strain (S_1) for Unconstrained G-1195 (0.1Hz)

An alternative to the d^*_{31} vs. field of Fig. 2.6 is to plot d^*_{31} as a function of piezoelectric strain (Fig. 2.7). This distinction proved important in predicting the strain response with the piezoceramic no longer stress-free, but elastically constrained, as will be discussed.

With the field-strain behavior of a stress-free piezoceramic characterized by the figures above, the next step is to determine whether that behavior is the same when the piezoceramic is free or elastically constrained by being incorporated into an elastic structure.

The simplest "structure" possible which involves a single piezoceramic and uncouples extension and bending is a sandwich structure. A test article comprised of a single sheet of 63.5mm x 25.4mm x .254mm G-1195 was bonded with Devcon cyanoacrylate adhesive between two similarly-sized sheets of aluminum. Electrical contact was made with both faces of the ceramic.

The expected induced strain in the sandwich by the piezoceramic depends on two things. These are the relative stiffnesses and geometry of the actuators and structure, and the commanded *actuation* strain. The stiffness/geometry influence can be thought of as a knockdown factor which is always less than unity. In this case, it is assumed that the epoxy layer provides a "perfect" bond between components (see Section 3.1), and the strain is

$$S_1 = \frac{(EA)_a}{(EA)_a + (EA)_s} d^*_{31} E_3 \tag{2.11}$$

where $(EA)_a$ is the extensional stiffness of the actuator, $(EA)_s$ the extensional stiffness of the aluminum structure, and $d^*_{31}E_3$ the piezoelectric actuation strain. In this case, with the structure having twice the cross-sectional area and elastic moduli of 63 GPa and 70 GPa for the PZT and aluminum, the stiffness/geometry term is equal to .310.

It is obvious that d^*_{31} in the term representing actuation strain is not constant. In view of the nonlinear field-strain behavior of Fig. 2.5, it might be postulated that the d^*_{31} is a function of field, as would be suggested by Fig. 2.6, or of strain as would be suggested by Fig. 2.7. Using the field-dependent approach the predicted induced strain in the sandwich structure is

$$S_1 = \frac{(EA)_a}{(EA)_a + (EA)_s} d_{31}^*(E_3) E_3 \tag{2.12}$$

where the appropriate d^*_{31} is found from a stress-free d^*_{31} vs. E plot similar to Fig. 2.5. This method was used to predict the induced strain in the sandwich structure. The result is plotted in Fig. 2.8 and labeled the 'prediction (field level).' When compared to the test results, the prediction consistently overestimates the measured strain data, by an increasing percentage as a larger field was applied.

From this result it can be inferred that d^*_{31} is not dependent on field. If however, the micromechanics of the situation are considered, it might be concluded that correlating d^*_{31} with the strain is more logical. The fundamental nonlinearity depends more on the deformation of microstructure of the piezoceramic than the externally applied stimulus.

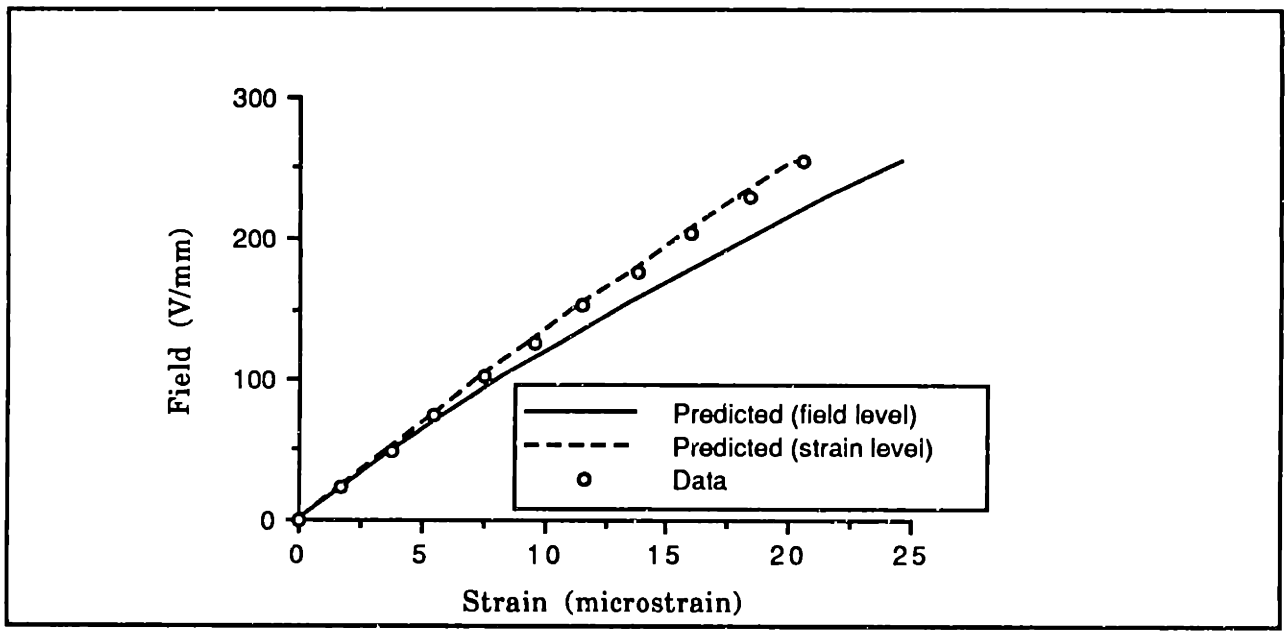

Figure 2.8: Induced Sandwich Strains

Thus, the alternative expression for predicted strain has d^*_{31} as a function of strain

$$S_1 = \frac{(EA)_a}{(EA)_a + (EA)_s} d_{31}^*(S_1) E_3 \tag{2.13}$$

Unfortunately, the value for d^*_{31} depends on strain, which is the unknown of the problem. There are two basic ways to overcome this implicit description. One alternative is to fit a function to the d^*_{31} vs. strain data and solve the resulting algebraic relation for S_1. The other is to start with an assumed value for S_1 and then iterate to find the correct strain. The latter method was used for the prediction in this report.

Figure 2.8 shows the correlation between predicted strain using the strain-dependent d^*_{31} and data. The deviation between prediction and data is within 2%, approximately the measurement error (.25 μS) for the strain. This strain-based approach is used to determine the correct d^*_{31} for the beam and plate structures in Chapters 3 and 4 and agrees with results found by Lazarus (1989).

It is believed that part of the reason for the discrepancy between the predictions and results for the glass/epoxy beam with embedded piezoceramics in Crawley and de Luis (1987) was the use of a d_{31} which was too high. The d_{31} coefficient for the piezoceramics used in experiments was tested stress-free at one field level at which many of the beam experiments were conducted. The value used for d_{31} was 50% higher than the manufacturer's reported value. However, the structure did not allow strains near the free level, so a lower d^*_{31}, still greater than the manufacturer's value, but based on the actual strain level should have been used in the prediction.

The use of a d^*_{31} dependent on the strain instead of a constant d_{31} is a significant step towards accurately representing strain in piezoceramics and should be considered in any model for piezoceramics inducing strain in structures.

2.2.2 Hysteresis

Hysteresis is a mechanical effect encountered in cyclical stress-strain relationships of plastic materials. Usually, an initially linear elastic relationship becomes plastic at a certain stress (or strain) level. If the material is returned to a stress-free state, a residual strain remains. Upon application of a stress in the opposite direction, the material deforms elastically, then the plastic deformation eventually begins. When the stress is again returned to zero, a residual strain in the opposite direction remains. When the cycle is repeated, the resulting locus forms a hysteresis loop.

The previous section discussed only the peak amplitudes of field and strain measured. If the commanded field and resulting strain response are plotted over one cycle, the resulting plot shows hysteresis. Figure 2.9 illustrates the real free field-strain relationship for three different levels of applied field. The data is taken from the same experiment which yielded the peak values of Fig. 2.5. Again, the reported strain is free strain in the x_1 direction in the unconstrained piezoceramic material due to a field in x_3 (E_3).

There are several important points to note regarding the hysteresis loop. The loops, as shown in Fig. 2.9, are traversed in a clockwise direction, and the same path is duplicated for repeated cycles at the same field level. Hysteresis was found to be present at all frequencies, including DC, and at all measurable ranges of field or strain. The hysteresis was observed at field strengths as low as 20V/mm and peak strains as low as 2 μS. For all tests conducted, the loop appeared to be very close to symmetric. The inverse slope of the hysteresis curve, measured by peak-to-peak strain divided by peak-to-peak field, is the value of d^*_{31} reported previously for the corresponding peak fields and strains. The slope of the loops decreases with amplitude, consistent with the increase in d^*_{31} with higher strains (Fig. 2.7).

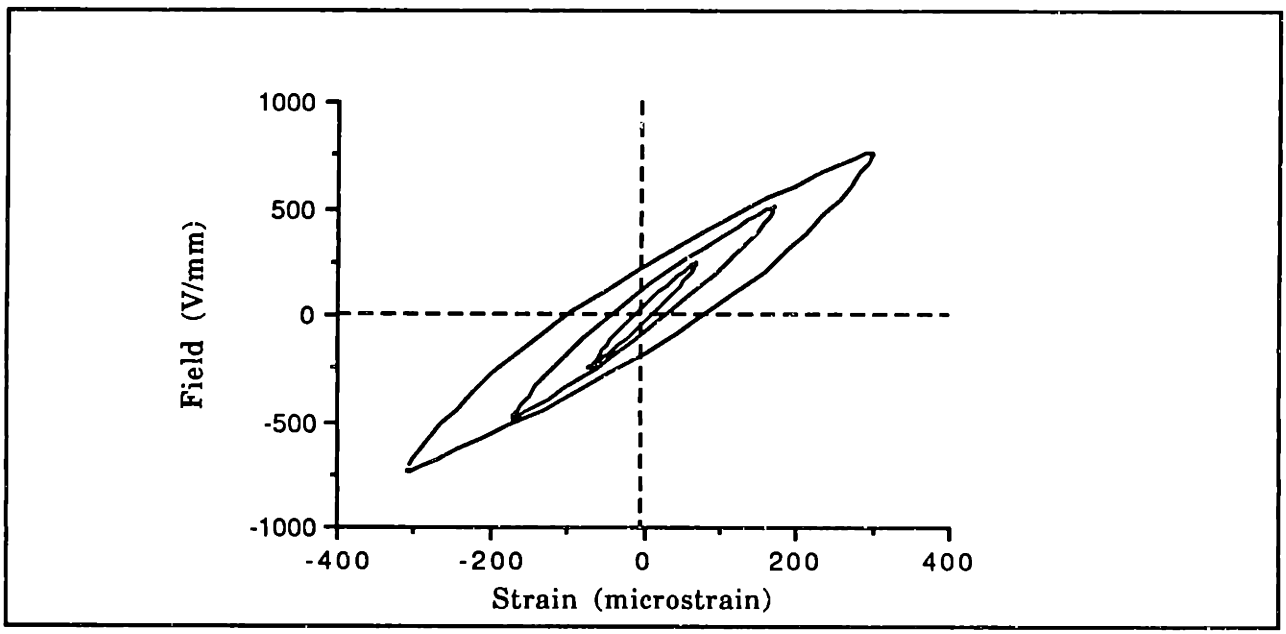

Figure 2.9: Field-Strain Hysteresis for Unconstrained G-1195 (0.1Hz) Illustrating Difference in Phenomenon for Three Different Peak Strain Levels

It is also apparent from Fig. 2.9 that the relative width or "aspect ratio" of the hysteresis loops increases with higher strains. The aspect ratio is defined as

the difference in the two strain values corresponding to zero applied field (the residual strains) divided by the peak-to-peak strain. Figure 2.10 shows how the aspect ratio grows with the amplitude of the peak strain. A cubic curve is fit to the data. The basic shape of the loop at all strain amplitudes is similar. The field-strain behavior can therefore be characterized reasonably well by d^*_{31} (the inverse slope) and the aspect ratio.

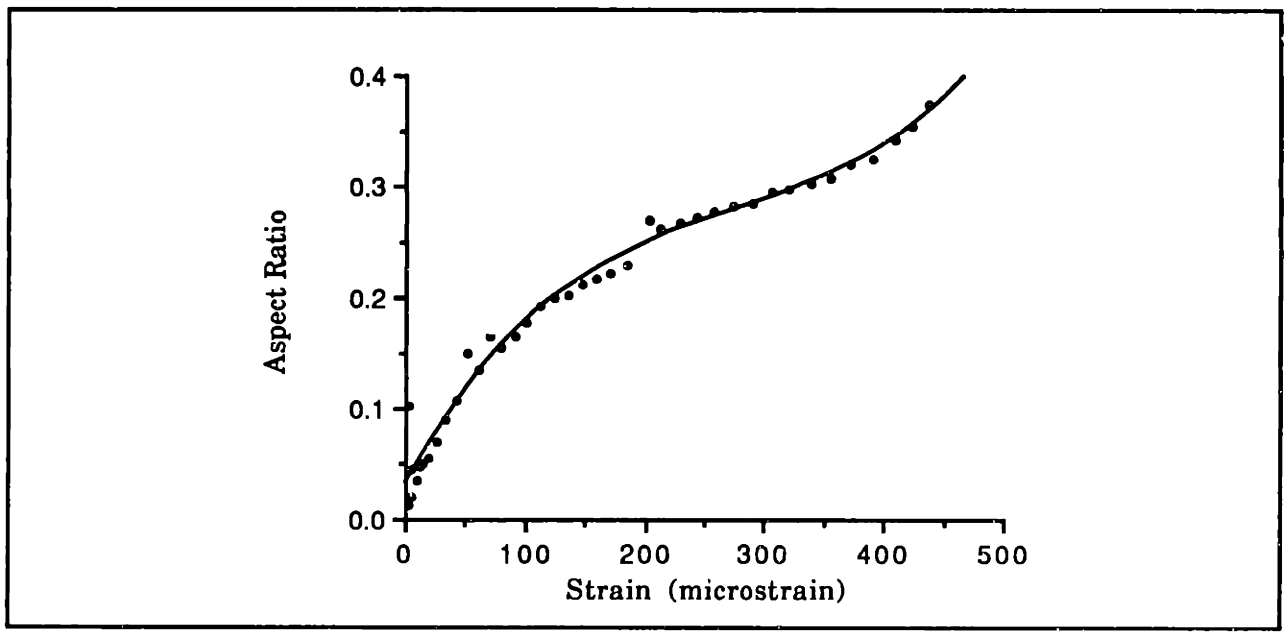

Figure 2.10: Field-Strain Hysteresis Loop Aspect Ratio vs. Peak Strain for Unconstrained G-1195 (0.1Hz)

Although hysteresis is present at all frequencies, it was found to be a particular problem for static tests. It was established that all experiments to determine the static capability of the actuators had to be carried out as hysteresis loops in order to capture all the relevant information. There are two specific problems for static operation brought about by the hysteresis: the presence of residual strains and the apparent "directionality" of d^*_{31}. From Fig. 2.9 it is apparent that on each loop there is a range of possible strain states for zero field. In the worst case (largest loop) shown in Fig. 2.9, when the applied field is zero, a strain variation of up to ±90μS can result. The presence of residual strain is a greater problem when operating at higher strain levels.

The apparent "directionality" of d^*_{31} can also lead to confusion. By again considering the largest loop in Fig. 2.9, in changing the field from 0 to +750V/mm, the change in strain can range from 305μS to 215μS. Hence, the apparent d^*_{31} depends on the residual strain state. These are valid concerns in

static applications, since a full loop will not always be completed. An application may require one-way actuation, followed by an actuation in the opposite direction some time later. Therefore, in static applications, care must be taken to note the residual strain state.

In vibration problems, recognition of the hysteresis is important, but is not as great a concern. The d^*_{31} coefficient, which represents the inverse of the (nonconstant) slope of the loop, can be used to adequately describe the field-strain behavior. However, the hysteresis appears as a small and variable phase lag whose presence may disrupt control functions. At very high frequencies, energy from the related mechanical losses can generate enough heat to affect the operation of the actuators (by heating epoxies or surroundings or possibly even depoling the piezoceramic). In general, however, the designer working at typical structural frequencies in applications which are not highly temperature sensitive can be less concerned about hysteresis.

Several studies (Martin, 1974, Smits, 1976, and Bondarenko, *et al.*, 1982) have tried to model the nonlinear hysteretic behavior of piezoceramics by using complex quantities to represent the mechanical, dielectric, and piezoelectric coefficients. These studies do not generally use the word "hysteresis" to describe the behavior, but instead refer to "loss parameters." Equation 2.14 shows a typical representation used by these authors

$$\begin{aligned} s_{11}^E &= s_{11}^{E\,(\mathrm{Re})} + j s_{11}^{E\,(\mathrm{Im})} \\ \varepsilon_3^T &= \varepsilon_3^{T\,(\mathrm{Re})} + j \varepsilon_3^{T\,(\mathrm{Im})} \\ d_{31} &= d_{31}^{(\mathrm{Re})} + j d_{31}^{(\mathrm{Im})} \end{aligned} \tag{2.14}$$

The first two equations are commonly used in the study of mechanics or dielectrics. The complex compliance is often used to represent mechanical losses or damping in a material. Because the mechanical damping has been measured and is not exceedingly high (approximately 1%) for the piezoceramic, the mechanical compliance is only slightly complex. The complex dielectric constant is usually referred to by the loss tangent, $\tan\delta = (\mathrm{Im}(\varepsilon)/\mathrm{Re}(\varepsilon))$. It can have values of 0.1 or higher at high fields where dielectric losses increase.

The complex coefficient models are convenient, but do not capture all the details of the hysteresis phenomena. They should at least be augmented to

include a d^*_{31} which changes with amplitude. In addition, the apparent phase lag is actually variable with respect to amplitude because the hysteresis loop is not a pure ellipse. Best suited for vibration applications, it is difficult to apply such complex analysis to static problems.

A description of the hysteretic behavior based on the rate of domain switching (Chen and Montgomery, 1980) provides a better physical explanation for the phenomenon. Such a description, which includes time- and field-dependent dipole realignment is useful for modeling both hysteresis and the creep phenomenon discussed below.

Without physically changing the field-strain hysteresis behavior it is possible to obtain a significant reduction in the apparent hysteresis by commanding *charge* versus strain (Comstock, 1981, and Newcomb and Flinn, 1982). The nonlinearities of the field-charge and field-strain relations are roughly proportional because they are due to the same phenomena. Bryant and Keltie (1986) show evidence of this for an actuator which uses a piezoceramic cylinder for axial force and displacement. In applications, the charge on the actuator can be required to be proportional to a charge which corresponds to the input signal magnitude. This "charge control" may reduce possible multi-valued strains encountered in static operation. A simple version of this scheme was easily implemented in the laboratory in conjunction with this study.

For vibration problems, if the variable slope of the field strain curve is used, the hysteresis effect can present itself as small phase lag between the field commanded and the resulting strain. "Charge control" will significantly reduce the lag. The underlying hysteresis is still present and can still cause heating at high frequencies and amplitudes, but its presence is conveniently masked. Other control methods for "flattening" the loop are also possible. Such schemes may be necessary in applications with very tight performance requirements. Discussion of them is beyond the scope of this study. General recommendations for dealing with hysteresis are presented in Section 2.3.

2.2.3 Strain Rate Dependence and Creep

In using piezoceramics as induced strain actuators for structural control it is important to know if the actuation strain produced by the actuators for a given field shows any strain rate or frequency-dependent effects. Closely related is

another phenomenon encountered in very low frequency and static situations, creep. Both effects will be discussed in light of experimental results.

There is no known model which explicitly addresses the strain rate-dependence of d^*_{31}. It is recognized in the IEEE Standard on Piezoelectricity (1978) that "nonlinearities are most pronounced under static and quasistatic conditions." Chen and Montgomery (1980) present a model which includes rate-dependent properties. But, much of the literature is concerned with high frequency applications where frequency-dependence is not characterized.

In order to measure the level of strain-rate dependence, a series of stress-free actuation strain tests was conducted. Three free strain measurements per decade of frequency were made on 63.5mm x 25.4mm x .254mm piezoceramics over the frequency range of .01Hz-100Hz. The tests were conducted at peak field levels of 278V/mm and 557V/mm, and d^*_{31} was calculated. The test could also have been done at two *strain* levels. But, it is more convenient to command field in the laboratory, especially in low frequency applications.

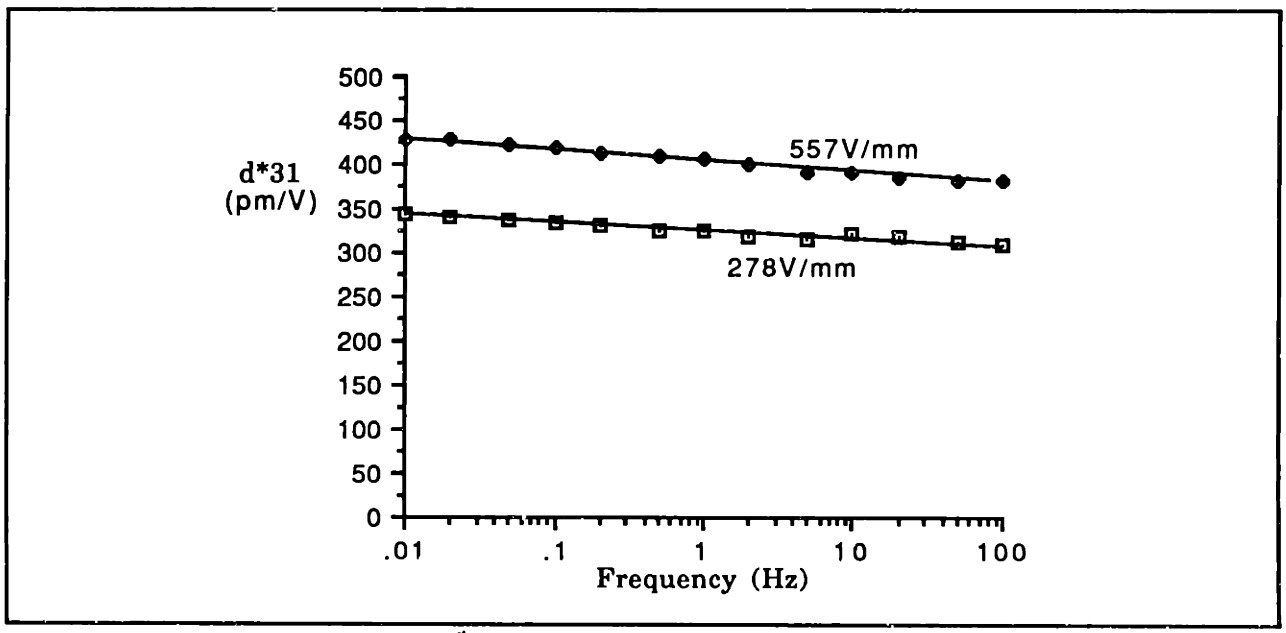

Figure 2.11: Variation of d^*_{31} vs. Frequency Illustrating the Influence of Creep in Unconstrained G-1195

Figure 2.11 shows the results of the two separate tests. The piezoelectric coefficient d^*_{31} is plotted against frequency for the two levels of applied field. The variation in d^*_{31} is relatively small over the four-decade frequency range.

However, the coefficient clearly shows some rate dependence. The d^*_{31} value at .01Hz is within 5% of the static (DC) value for the same field level.

The phenomenon of piezoelectrically-induced creep is the cause of the variation in d^*_{31} with frequency. Creep in piezoceramics has been recognized by the manufacturers, and several previous investigations (Jaffe, *et al.*, 1971 and Chen and Montgomery, 1980), but is generally not dealt with in theoretical studies. In experimental studies, especially those which utilize piezoceramics under static fields, creep is readily apparent.

Instead of the prolonged stress which induces conventional mechanical creep, it is the prolonged application of an electric field which causes the piezoelectric strain to grow with time. It is surmised that the large strains at large fields cause a physical realignment of the domain microstructure and a change in the polarization of the parallel dipoles which make up each domain.

In order to determine the relative levels of creep at various field strengths and strain levels, a series of simple tests was conducted. The test specimen was once again a 63.5mm x 25.4mm x .254mm G-1195 sheet. Accurate measurement of creep required that residual strains on the test ceramic be brought to zero before the test was begun. To find the true zero residual strain, a hysteresis loop was executed prior to testing. The center of the loop was then considered the actual zero strain point. Creep was observed at room temperature in stress-free piezoceramics, both when the field was applied in the same direction and against the direction of polarization.

Beginning from a condition of "true" zero strain and zero field, a step increase in field against the direction of polarization was applied and the inplane strain response of the ceramic sheet was measured with a strain gage and recorded on a Nicolet digital oscilloscope. Several different step values of field were applied. The step in field was both rapid (less than 0.1 second rise time) and free from bounce. From Fig. 2.12 it is clear that the initial step response in strain is rapid. In less than 1 second the majority of the change in strain is achieved. When the response is considered over a longer time scale however, the creep becomes apparent.

The basic nonlinear field-strain relationship discussed previously can be seen in the step responses. Although 787V/mm is four times the field strength of 197V/mm, it produces within 1 second a strain of 340μS, more than six times

the strain of 55μS produced by the 197V/mm field. This corresponds closely with the .1Hz data shown in Fig. 2.5. The subsequent increase in strain over *time* represents the effect of the creep. There is significant additional strain due to creep, especially at the higher applied field levels. For example, for fields of 197V/mm and 787V/mm, the strains at 400 seconds are 60μS and 430μS. This represents increases due to creep of 9% and 26%. The effect of creep is clearly more important at higher field and strain levels.

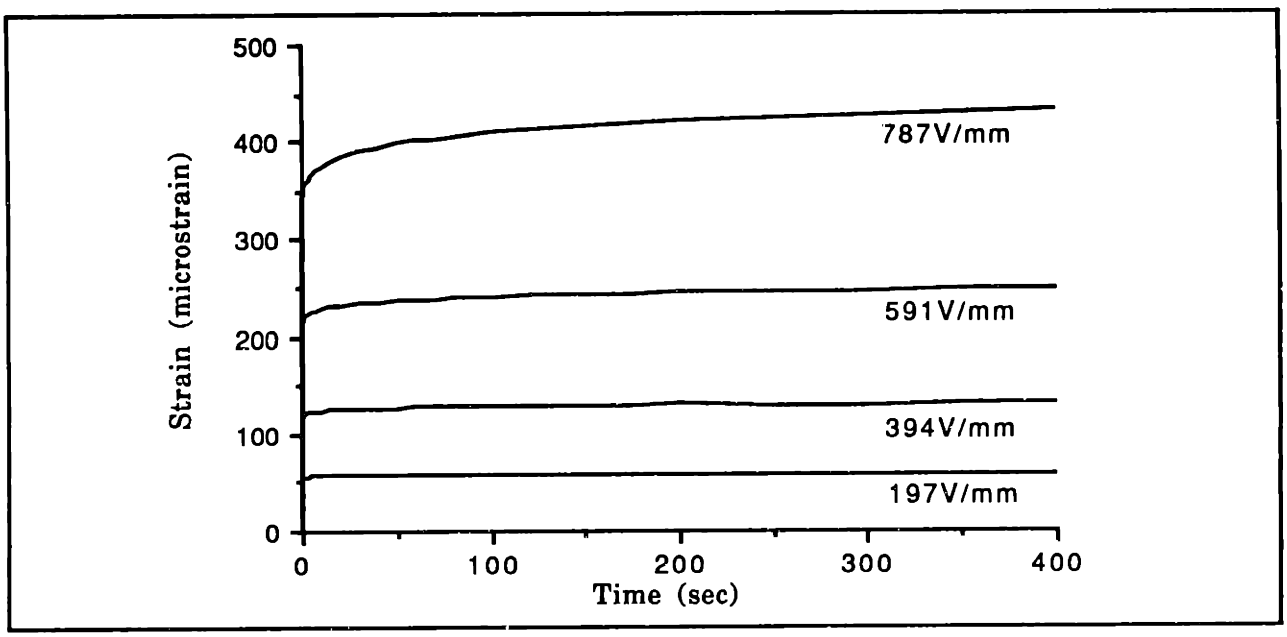

Figure 2.12: Strain Response to Steps in Applied Field Illustrating Piezoelectric Creep for Unconstrained G-1195

Thus, for static operation, there is some ambiguity in the final value of strain achieved. For the static tests conducted in this study, the strain was allowed to attain a near constant level before measurements were taken. A settling time of 300 seconds was used. Where one-way actuation is used, as represented by the step responses in Fig. 2.12, the creep can cause drift in the induced strain of a structure. For this reason, strategies discussed in Section 2.3 to account for creep strain may have to be adopted.

The strain rate dependence of d^*_{31} (Fig. 2.11) is related to creep. At lower frequencies, enough time is spent per half cycle for some creep to occur. In higher frequency applications, the field and strain change rapidly so that no significant creep strain occurs. For dynamic operation, the dependence of d^*_{31} on frequency can be used.

2.2.4 Depoling

Many applications which use piezoceramic actuators require large deflections or strains. It is therefore desirable to utilize the full potential of the piezoelectric effect. However, in an effort to obtain the greatest achievable strain, the net polarization of the ceramic and thus, its piezoelectric properties, can be severely degraded. In the section on basic field-strain behavior, a limiting field level was mentioned. In this section, that concept will be expanded on and the depolarization (or depoling) process as well as the operating limits imposed by high fields will be discussed.

During the manufacture of piezoceramics, a large (>1 kV/mm) field is applied across the ceramic material to initially orient the the previously randomly-oriented crystallites toward the direction of the polarizing field. The polarization of the ceramic is not permanent. If a large static field is applied in the same direction as the polarization, no depoling will occur. Static tests conducted elsewhere (Lazarus, 1989) have shown that d^*_{31} does not continue to grow at substantially higher field levels in the poling direction, in contrast to the trend reported earlier in this section. The real limit on the field which may be applied in the poling direction will be imposed by one of two things. Either the field will breakdown by arcing between the electrodes or the ceramic will crack due to the high strain. The former situation can be avoided by careful electrical isolation. The latter implies that, since actual induced strain will be limited in a structure, a larger field may be applied to a piezoceramic which does not achieve its free strain. If a large enough field is applied opposite to the polarization direction, the ceramic will be depolarized or *depoled*. The field which causes depoling is called the coercive field, and is often designated E_c. A piezoceramic may also be depoled if an extremely large stress is applied or if its temperature exceeds the Curie point for that material.

If the coercive field is applied for a period of time, the piezoceramic will be repoled in the direction opposite to the original poling. If the opposing field is only slightly less than E_c, the ceramic may still depole and repole in the opposite direction, but much more slowly.

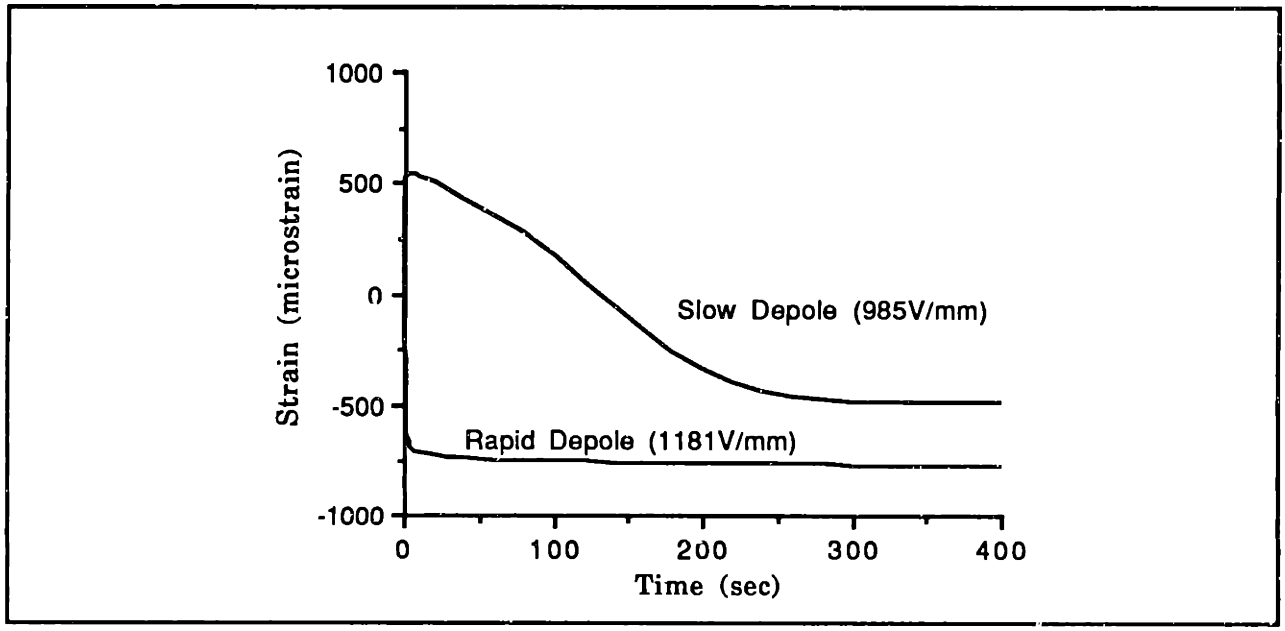

Figure 2.13: Strain Response to High Applied Fields Illustrating Depoling in Unconstrained G-1195

Figure 2.13 shows the strain resulting from step inputs in field opposite to the poling direction. The test conditions were the same as those used to investigate creep, but higher fields were applied. For both applied fields, a strain of 450-500μS occurs within 1 second. The slow depoling and repoling from a 984V/mm field occurs over several minutes. The result is a strain of comparable magnitude and opposite direction to the original strain. Figure 2.13 can be contrasted with the strain responses of Fig. 2.12. In both cases the initial strain response is in the direction expected. The first few seconds of the slow depoling show behavior similar to that seen in Fig. 2.12. The strain during rapid depoling follows a path similar to the ones in Fig. 2.12 for only the first fraction of a second. The rapid depoling and subsequent repoling resulting from the application of a field of 1181 V/mm takes place over a time of roughly 2 seconds. The repoling is followed by some creep.

Degradation effects from the depoling-repoling cycle were also investigated in a separate test. In that test, a field of 1400V/mm was applied to a piezoceramic sheet opposite to the original polarization direction for 30 seconds, depoling the ceramic. The 1400V/mm field was then reversed to repole the ceramic in the original direction. This repoling field was applied for 180 seconds. Subsequent to the depole/repole cycle, the strain response of the ceramic was

measured for fields up to 400V/mm. The cycle and measurement was repeated 25 times. There was no measurable loss in piezoelectric properties.

In higher frequency applications, the coercive field also limits the amount of strain which can be achieved. However, an oscillatory field greater than the static coercive field is necessary to depole the ceramics. If the field is of sufficient strength, depoling will occur when the direction of the time-varying field is opposite to polarization. The coercive field thus depends on frequency. It is often reported as two separate values - one static and one at 60Hz.

In general practice, operation against the poling field direction should be limited to some fraction, perhaps 80% or 90% of the coercive field. But no similar limit is imposed in the poling direction. In order to achieve larger strains, the depoling limit can be circumvented. This is usually accomplished by applying a large bias field to insure that the net applied field remains either always in the poling direction or at least well below the coercive field in the antipoling direction. For example, if the coercive field is 1000V/mm, a 1500V/mm static field could be applied in the poling direction. The range of oscillatory operation would then be extended from near 1000V/mm peak to near 2500V/mm peak. Alternatively, a field of 1500V/mm peak could be applied and operation kept below 1500V/mm in order to maintain the net applied field aligned with the poling direction.

2.2.5 Orthotropic Inplane Response

The objective of this subsection is to determine whether the orientation of the x_1 and x_2 axes is indeed arbitrary as the linear transversely isotropic piezoceramic model (Eq. 2.3) suggests. According to the assumptions of the model, the ceramic is made up of randomly oriented crystallites. Prior to the application of the poling voltage, the net polarization is zero and there is no distinction between the physical structure in any direction. The material is mechanically and electrically "isotropic." Upon poling, the x_3 direction is distinguished from the directions perpendicular because of the reorientation of the crystallites. But the ceramic is still transversely isotropic. The inplane orientation of the x_1 and x_2 axes should be arbitrary.

In the piezoceramic constitutive matrix representing the ideal linear model (Eq 2.3) only three independent piezoelectric coefficients (d_{31}, d_{33}, and d_{15})

are included. In the x_1-x_2 transversely isotropic piezoceramic it is assumed that $d_{24} = d_{15}$ and $d_{32} = d_{31}$.

A test was conducted to discern whether the piezoelectric behavior in the x_1-x_2 plane is indeed isotropic, particularly if d^*_{32} is equal to d^*_{31}. Two different material types were investigated: G-1195 and PZT-5H, manufactured by Vernitron. The test specimens were stress-free 63.5mm x 25.4mm x .254mm G-1195 and 45.7mm x 22.9mm x .254mm PZT-5H. A BLH 45 degree strain rosette was mounted on the center of the upper surface of each of the ceramic sheets and a field (E_3) was applied across the ceramic. From the rosette measurements the strain in every direction in the x_1-x_2 plane could be calculated. In the ideal case, the inplane strain does not change with orientation.

An electric field of from 0 to 550V/mm peak was applied to the ceramics. The test was conducted at several different frequencies, with no significant frequency variation in results other than the strain rate effects discussed in the previous section. Figure 2.14 shows the peak field-strain results for G-1195 and PZT-5H piezoceramics for tests conducted at 50Hz. The three curves represent strain measurements in 3 directions separated by 45 degrees. The basic nonlinear field-strain behavior is consistent with what was described previously. Over this field range d^*_{31} is slightly greater for the PZT-5H material. In both materials, there is a clear difference in the strain in the three directions, but the relative values of the strains remain roughly the same as the field level is increased. In the ideal inplane isotropic model all three curves would coincide.

The same data can be thought of in a different way by making use of the concept of principal strains. From the rosette data the principal directions and strains can be calculated by standard methods. The two principal strain values put a bound on the possible strain levels. This approach assumes that there is no strain variation with location in the plane.

For example, for G-1195, compared to the strain in the x_1 direction corresponding to a 550V/mm field, the -45 degree strain was 7.0% less and the 45 degree strain 10.2% greater. The calculated principal strains were 11.0% greater and 7.2% less than the x_1 strain. The principal directions for the two materials are shown in Fig. 2.15. It is clear that d^*_{32} does not equal d^*_{31} for free strain of the piezoceramics tested. Although it was not measured, it is possible that the elastic compliances (s^E_{11} and s^E_{22}) are different as well.

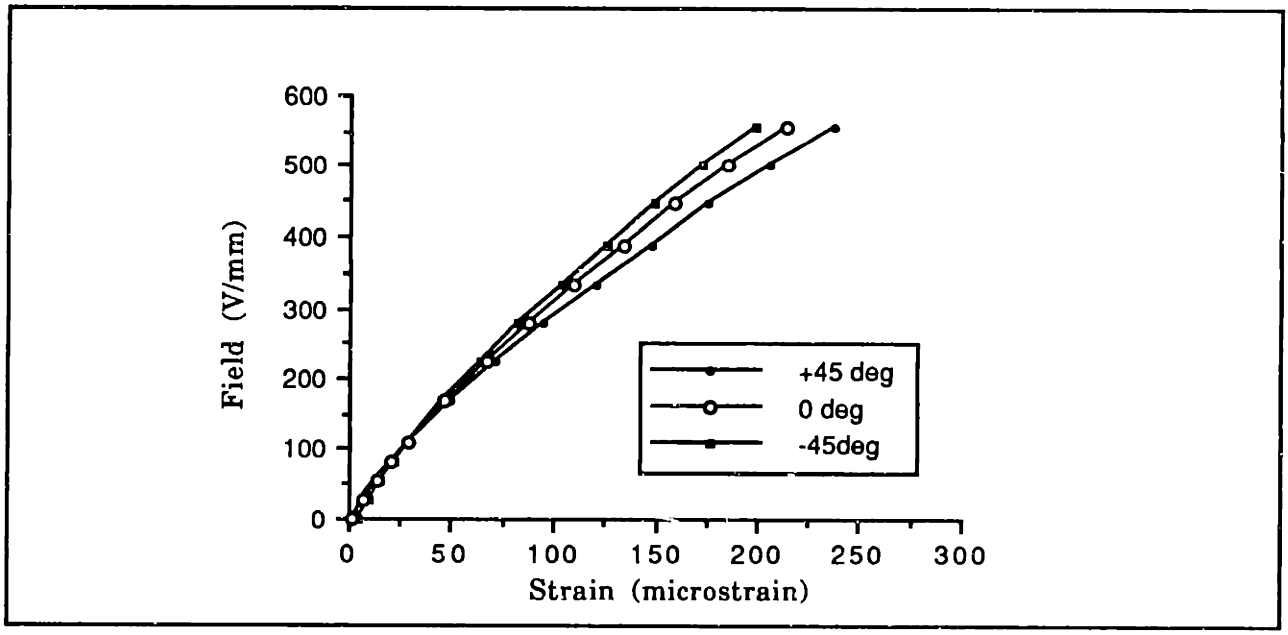

a) Piezoelectric Products G-1195

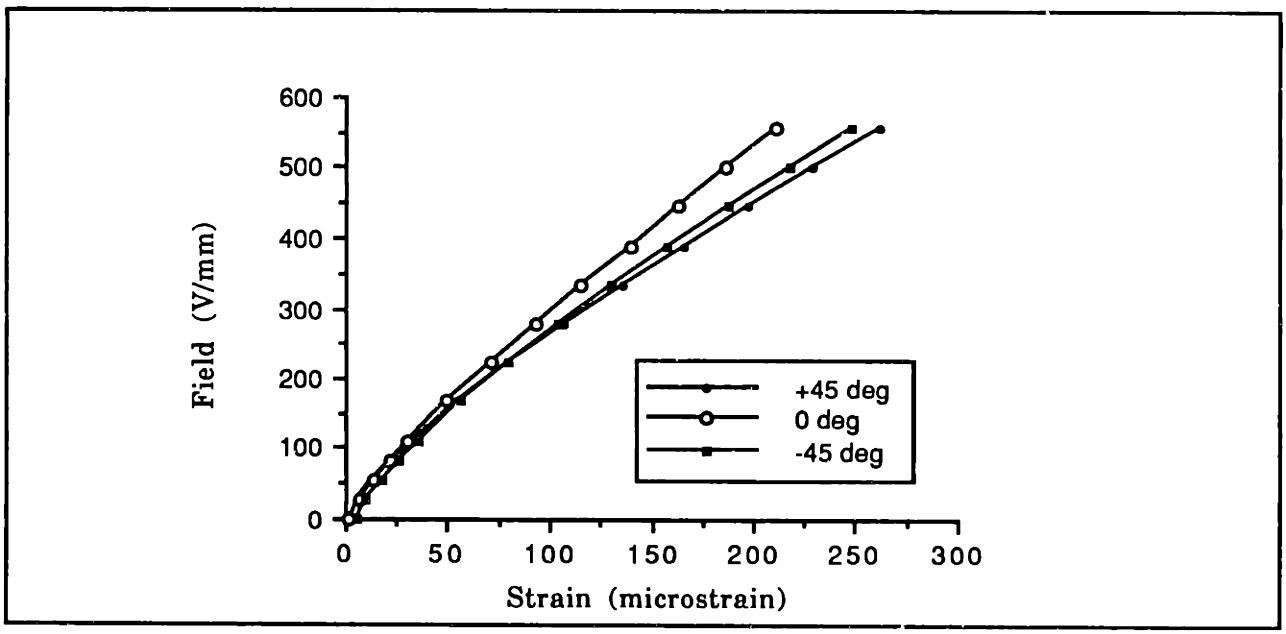

b) Vernitron PZT-5H

Figure 2.14: Inplane Strain Response to Applied Field from 45-degree Strain Rosette Illustrating Orthotropic Strain Coefficient (50Hz)

Three possible explanations for the observed orthotropic phenomenon were considered: manufacturing/processing effects, the shape of the ceramic sheet, and the spatial separation of the three strain measurements. The manufacturing effect explanation proposes that the introduction of the orthotropy could have taken place during the process where the ceramic is

spread out and rolled under a knife edge to obtain an even thickness. It is common to introduce orthotropy in similar processes where, for example, a metal is rolled. The manufacturer suggested this possibility.

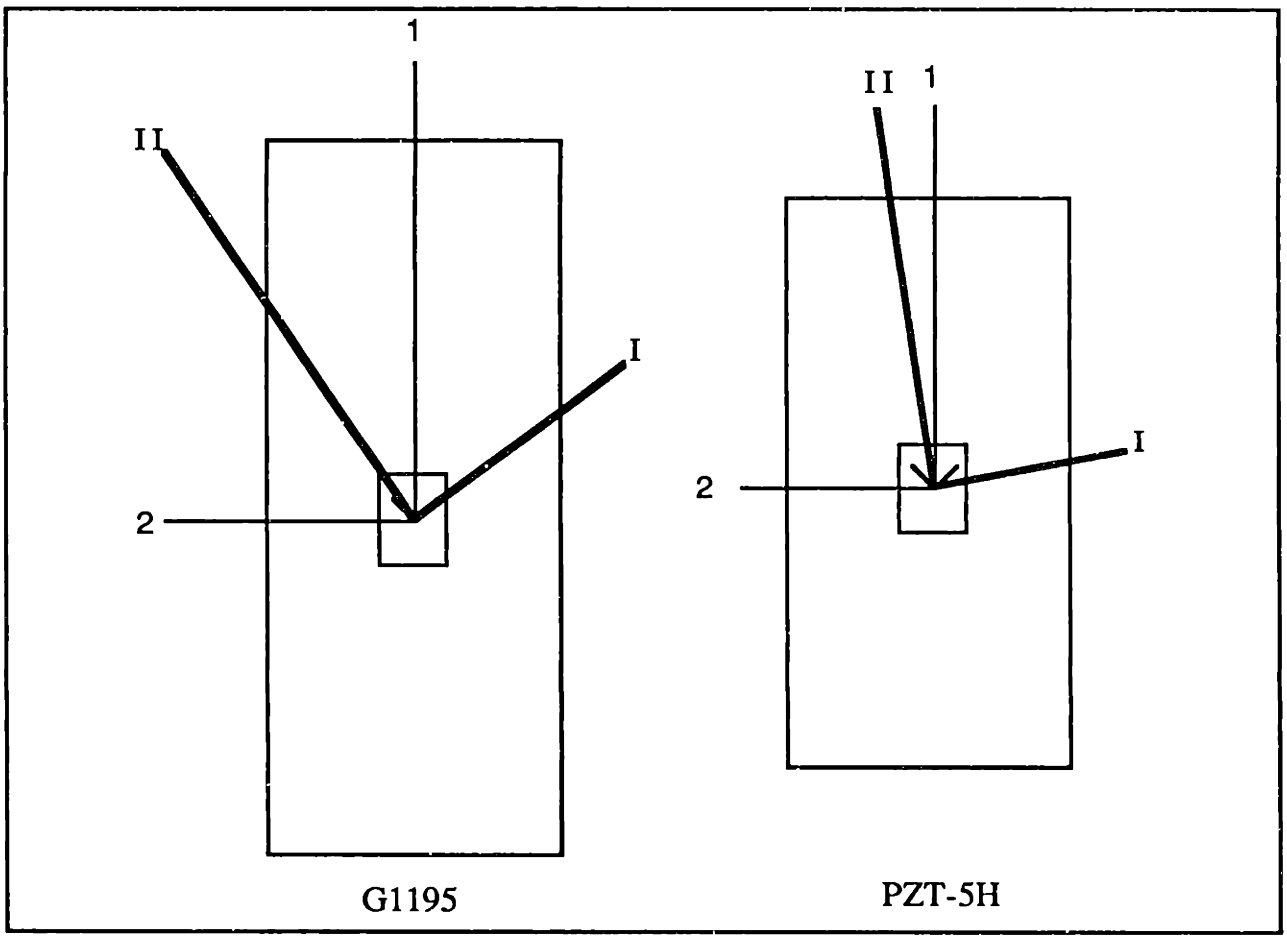

Figure 2.15: Principal Piezoelectric Strain Directions Determined from Strain Rosette Data

The second explanation is that the manner in which each sheet is cut influences the inplane strains through three-dimensional effects from the sheet boundaries. When the shape of one PZT-5H specimen tested was changed from rectangular to square by cutting off a large portion of the ceramic, no difference in results was found. Based on this and other tests, no clear relationship between the directions of principal strain and the shape of the piezoceramic sheets has been found.

The third explanation is that the spacing of the three gages on the rosette, though small, meant that the strain was actually measured in three places, separated by approximately 2mm, compared to specimen widths of about 25mm. This idea was discarded on the basis of extensive field-strain data from different

specimens of the same material which match to within a few percent even though the locations of measurement were not precisely controlled.

None of the explanations provides a definitive reason for the observed behavior. Although the orthotropy was significant for free piezoelectric strain, under elastic constraints, it was found that the orthotropic effects tend to blur. When a piezoceramic sheet was sandwiched between two similarly-sized pieces of aluminum there was no longer any measurable orthotropy associated with the strain (Lazarus, 1989).

In one-dimensional applications, such as the beams discussed in Chapter 3, the field-strain behavior in the single direction of interest can be measured and used to predict structural deformation. Strain in only one direction was used for correlating the beam experiments in Chapter 3. The same is the case for the plates in Chapter 4. It is unrealistic to expect that the piezoceramic strain has to be completely characterized as a function of inplane orientation. In view of other, more significant nonidealities, a single measurement, along the direction of primary interest, should be adequate.

2.2.6 Effect of Imposed Mechanical Strain

It was shown previously in this section that the piezoelectric coefficient d^*_{31} exhibited a significant dependence on the level of piezoelectrically-induced strain. Piezoceramics which are part of structures will experience a variety of mechanically-induced strains as well. It would be undesirable for actuator performance to depend strongly on the mechanical stress and strain of the structure because prediction of strain behavior would then be greatly complicated. The level of dependence of the piezoelectric coefficients on the imposed mechanical strain is therefore a concern.

It is known that a large stress can depolarize a piezoceramic. Short of depolarization, an applied stress can degrade piezoelectric properties (Jaffe, *et al.*, 1971 and Doroshenko and Ugryumova, 1978). The purpose here is not to establish the depoling stress level, but to determine the effect of lower magnitude stresses typically encountered in structural control.

In Doroshenko and Ugryumova (1978), a compressive stress of σ_1=200MPa produced a loss in d_{31} of from 5-30% for the six different PZT compositions tested. In Jaffe, *et al.* (1971), application of a large uniaxial compressive stress was

found to cause an anisotropy. A loss of 50% in d_{31} and a corresponding 80% increase in d_{32} is reported under 150MPa of compressive stress with less than 2% loss in d_{31} and 7% increase in d_{32} for stresses under 35 MPa. The manufacturer of the ceramics used in this study (Piezoelectric Products) reports in the material data that there is 0% change in d_{33} at 3000psi (21MPa) and 13% decrease at 5000psi (35MPa). Data were not available for changes in d_{31}, which is the concern here.

An experiment was carried out to confirm that a low level imposed mechanical tensile stress (σ_1) had little influence on piezoelectric performance. A 25.4mm by 76.2mm sandwich of PZT G-1195 between 2 sheets of aluminum was used as the test structure. The three .254mm thick layers were bonded together with Devcon cyanoacrylate adhesive. A sandwich structure was used for the tests because the load was more easily applied to it than to a single free

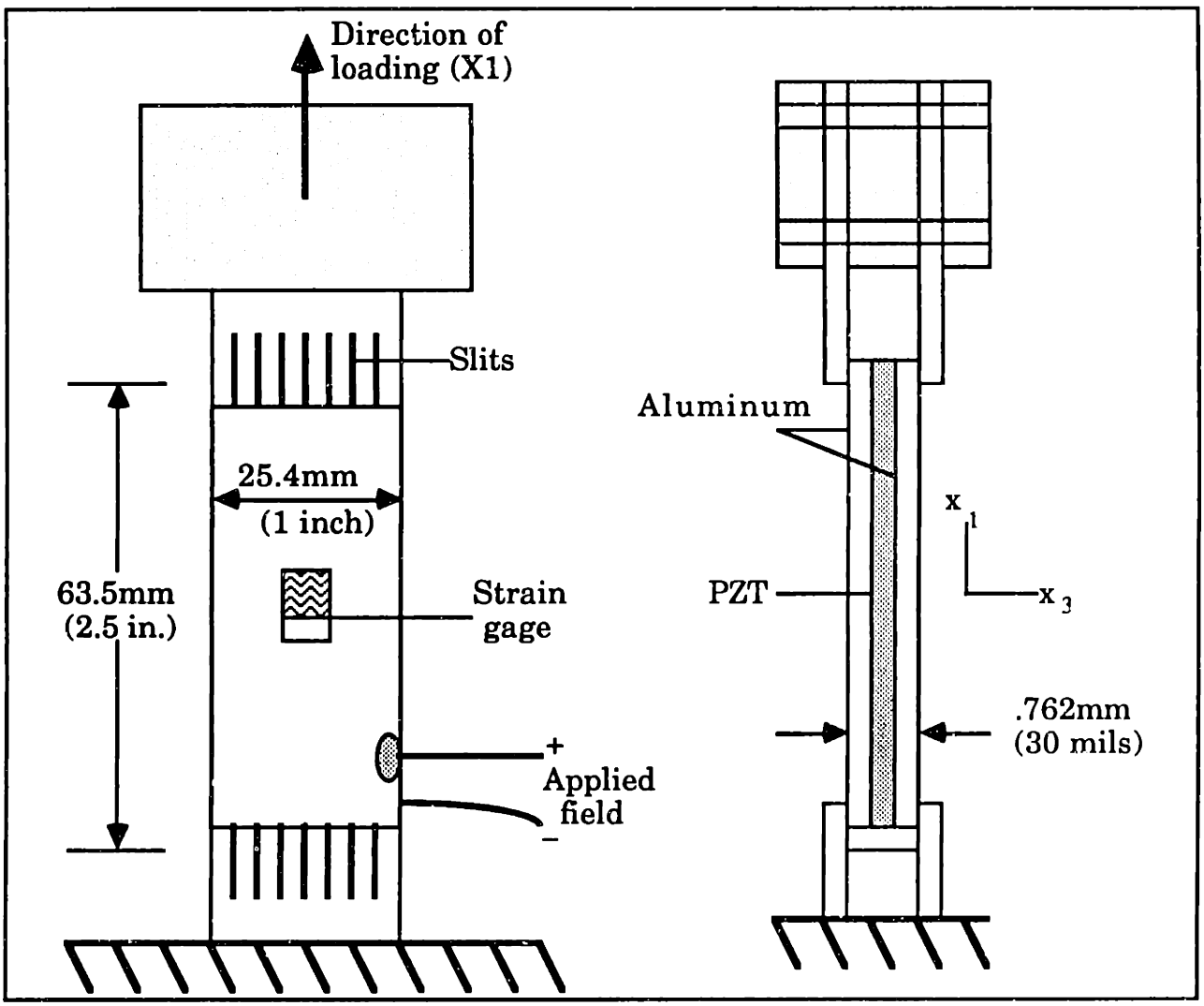

Figure 2.16: Experimental Configuration for Mechanical Loading of Sandwich Specimens

ceramic.

The strain response of the piezoceramic was tested at 0.1Hz prior to bonding between the aluminum. The sandwich was then tested, again at 0.1Hz, under no external mechanical load.

An attempt was made to load the sandwich in the x_1 direction, without changing the stiffness of the constraining layers in x_2. Figure 2.16 shows the experimental setup for loading the sandwich. Aluminum loading tabs were bonded to the sandwich. The vertical (longitudinal) slits were an attempt to limit the transverse restriction imposed by the tabs. The lower tab was clamped to a rigid base. The load was applied to the upper tab with a winch and steel cable mechanism and measured with a load cell. The tabs caused a slight reduction in the strain induced in the sandwich. For the tests, the "zero stress" value was measured while the sandwich was in the clamp, but with no external load applied.

Mechanical stresses up to 13MPa were applied to the sandwich. A 550V/mm field was applied at each stress level, and peak-to-peak strain was measured. Figure 2.17 shows the results with peak piezoelectric strain normalized by peak piezoelectric strain at zero load. This normalized strain is also a measure of normalized d^*_{31}. The variation in d^*_{31} for these levels of bias strain is small and repeatable. It is consistent with the change (increase) in d^*_{32}

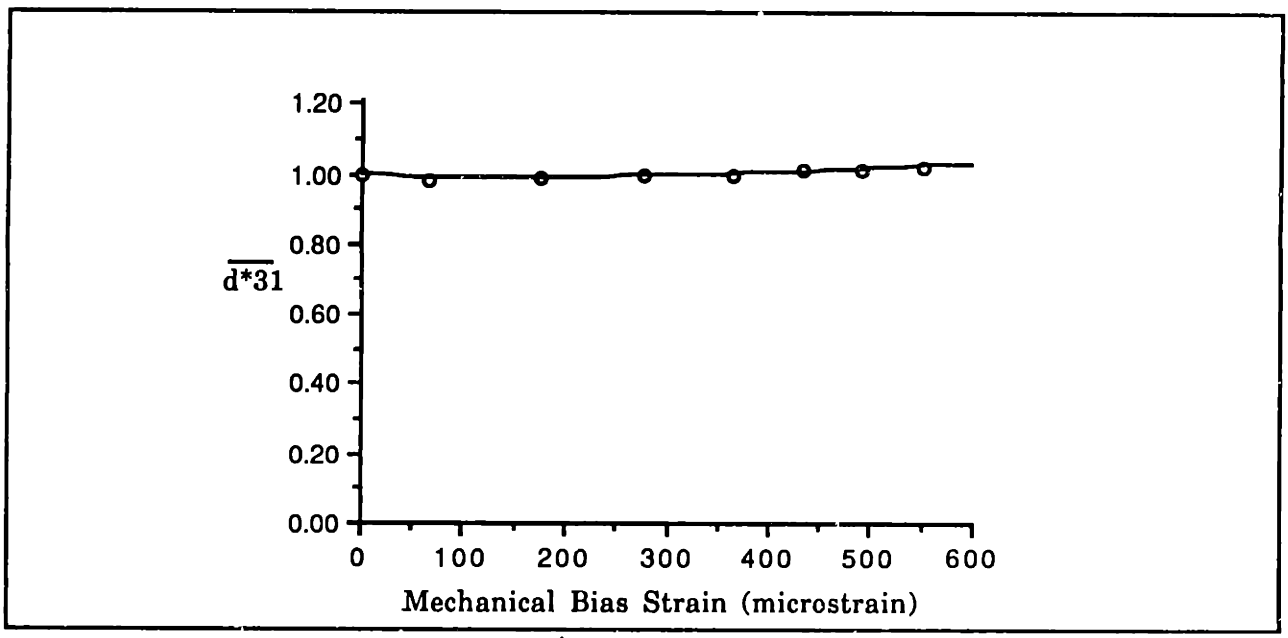

Figure 2.17: Change in d^*_{31} with Mechanically-imposed Strain

seen by Jaffe, *et al.*

It can be concluded that the level of *piezoelectrically-induced* strain determines the piezoelectric properties. The externally imposed mechanical strain does not affect d^*_{31} to a degree comparable to the piezoelectrically-induced strain. For 100μS of mechanically-induced strain, the apparent change in d^*_{31} is roughly 1%. Yet the basic stress-free field-strain data in Fig. 2.7 shows that 100μS of piezoelectrically-induced strain increases d^*_{31} by more than 50%. From this it can be concluded that d^*_{31} variation is much more dependent on piezoelectrically-induced than mechanical strain. For stiffness-driven problems, where high stresses are not encountered, it is therefore not necessary to account for mechanically-induced changes in piezoelectric properties. For high stress problems the piezoelectric performance is known to decline and should be a concern.

2.3 IMPLICATIONS OF NONIDEALITIES FOR USE

In the previous section, experimental evidence of several nonideal phenomena present in piezoceramics was detailed. It is obvious that the model of Section 2.1 is both a linearization and simplification of actual behavior. In this section, the implications of the nonidealities for the use of piezoceramic induced strain actuators will be discussed. Techniques for either avoiding, modeling, or otherwise dealing with the real phenomena will be presented.

Of the six phenomena illustrated (the dependence of d^*_{31} on strain, field-strain hysteresis, frequency dependence and creep, depoling, orthotropy, and response to mechanical strain) the last two are of least concern. As was stated previously, an isotropic model is believed to be adequate when piezoceramics are part of larger structures. Also, although it is known that extremely high imposed stresses will degrade performance, even to the point of depolarization or tensile failure of the ceramic, the lower imposed mechanical strains more typical of stiffness-limited structures do not significantly influence piezoelectric properties.

Depoling and Coercive Field

Before addressing the other three nonlinearities, depolarization limits will be discussed. As a general rule, the user of piezoceramics should attempt to

design so as to apply electric field in the polarization direction. Several other steps are necessary in considering the possibility and effects of depoling. First, the coercive field, E_c, should be established for the frequency of interest. The variation in E_c for different specimens of the same material was found to be small, but there may be several weakly poled pieces in a large lot. The static E_c will always be lower than the dynamic values.

Second, the operating range of field must be established. The field against the poling direction should be limited to some fraction of the coercive field (perhaps 80%). It may be desirable to set a voltage limit on amplifier output. If higher strains are required, a bias field may be applied in the poling direction to shift the operating range of the net applied field. The net field opposite to the poling direction must still be kept below E_c.

Third, a piezoceramic may partially or fully depole when in operation. There is often difficulty in recognition of the depoling. This typically will be the case when the actuator is either one of a large network or is only partially depoled. The actuator strain should be compared periodically with a baseline performance to determine if full or partial depoling has occurred. Clearly, the depoling of single or multiple ceramics due to a field exceeding E_c, an overstress, or a temperature above the Curie point cannot be allowed to cause a system instability. The likelihood of depoling and subsequent detection should be considered prior to the start of operation as part of an overall fault tolerance strategy.

Finally, if a piezoceramic is depoled, it is desirable to have the capability to repole it. In some applications, especially during operation, it may not be feasible to repole. It was found that the piezoceramics tested were able to withstand depoling and repoling 25 times without subsequent measurable loss in performance. Thus, repoling capability is an easy way to help insure long term utility of an actuator.

Nonlinear Field-Strain, Hysteresis, and Creep

We are left with three (related) phenomena of concern: the nonlinearity in the field-strain relation, hysteresis, and creep. It is true of all three that lower strains cause less nonlinearity. When the piezoceramics are used as induced strain actuators, the elastic constraint of a substructure will cause induced strains

lower than the piezoceramic actuation strain. Therefore, the nonlinear effects will be lessened. In relatively low strain precision applications, this reduction of nonlinearities can be exploited.

However, in many applications it is desirable to induce the highest strain possible. By extending the field operating range with a large bias field, the achievable induced strain and therefore the nonidealities, will be of the order of the free actuation strain effects shown here. The behavior can therefore not be avoided.

Unlike depoling, where limits on applied field can guarantee safe operation, the fundamental field-strain nonlinearity must be confronted. The degree of this nonlinearity differs with material, but it is present in all piezoceramics. The field-strain behavior, independent of the associated hysteresis, may be represented in two basic ways: a model which attempts to accurately represent the full extent of the nonlinearity; or a linearized model.

In the case where the full nonlinear behavior is modeled there are options. Either the field-strain or the d^*_{31}-strain relation can be modeled. A d^*_{31}-strain fit provides the advantage that the correct value for d^*_{31} for any level of induced strain can be found. In the presentation of the data in the previous section, the accuracy of the analytical curve fits was not emphasized. However, for low strain levels, simple polynomials provide accurate fits. For the range of fields and strain tested (up to 90% of E_c) with a quadratic fit, correlation coefficients of R^2=.998 for field as a function of strain and R^2=.994 for d^*_{31} as a function of strain were achieved. For higher fields (in the poling direction) and strains, the fit is likely to be less accurate. A higher order polynomial may be used, or the data may be stored in tabular form and accessed when necessary.

Alternatively, if it is felt that the basic field-strain nonlinearity adds too much complication to a model, the relationship might be linearized around a specific amplitude with deviations treated as disturbances. This simplified approach uses a single value, which may or may not be chosen to be equal to the small signal d_{31} to represent d^*_{31}. This technique simplifies control design but sacrifices some accuracy. de Luis (1989) uses a single value for d^*_{31} in an application where induced strains never exceed 25 microstrain. A single d_{31} is also used in Chapter 4, where induced strains are below 5 microstrain.

In most cases, the manner in which the field-strain nonlinearity is addressed should recognize hysteresis. This is especially true in high strain and static situations. As a first step, a piezoceramic material with a small amount of hysteresis can be chosen. G-1195 is believed to exhibit more hysteresis than several other piezoceramic compositions. Beyond material improvements, there are three ways to deal with hysteresis. It may be ignored, modeled to varying degrees, or controlled and linearized.

For vibration problems the simplest approach is to use only the relative amplitudes of the field and strain with hysteresis not explicitly represented in the model. The hysteresis can then be considered as an unmodeled phase lag whose presence will not cause instability if a positive phase margin is maintained. This approach is not applicable to static problems.

If hysteresis is explicitly modeled, vibration and static problems must be treated differently. For oscillatory strains, because the phase lag between strain and field varies both within each cycle and with changes in strain amplitude, there may be difficulty in representing the phase lag by a complex d^*_{31} coefficient. A transfer function representation of the hysteresis is also not broadly valid because of the nonlinearity of d^*_{31} with strain amplitude, and to a lesser extent the variable lag .

For static applications, a pure phase lag representation is definitely not satisfactory. Because static operation does not follow a repeating path on a field-strain plot, a static model of hysteresis must be more explicit. It is necessary to recognize and account for residual strains as well as the history and direction of operation. However, a model which includes explicit representation of a hysteresis loop with one or two equations is valid only for operation along that loop. For example, if the hysteresis loop corresponding to a 200μS peak strain is modeled, and actual operation uses strains from 0 to 150μS, the model will not be adequate. This difficulty results from the dependence of d^*_{31} and the aspect ratio of the hysteresis loop on induced strain.

A final approach to hysteresis is to effectively close the hysteresis loop through a control system. This requires some basic knowledge of the hysteretic behavior, and is more easily accomplished for oscillatory systems. Methods such as charge control which reduce the apparent hysteresis between input and output are easily implemented and can render the response more predictable. For static

problems, a simple control system designed with at least an awareness of hysteresis, to monitor strain and apply field can adequately deal with hysteresis. If hysteresis is not recognized in the design, performance may suffer. Methods for dealing with the hysteresis loop in control design will be the object of further study.

In most cases, creep will cause less difficulty than hysteresis. At high frequencies creep is not important. For vibration control applications creep can thus either be ignored, or, if frequencies are low (<10Hz), its presence may be allowed for in a stabilizing control system which is likely to be present. Creep is most prevalent under high static fields. If a large bias field is used to extend the achievable strain, significant creep may result. For precision static problems, a control system should be designed to specifically address creep. When a high field is applied, such a system will reduce the field magnitude with time to offset creep strain, keeping net strain constant.

Summary

If piezoceramics are to be used as induced strain actuators to achieve high strains, their inherent nonidealities will be significant. It is recognized that precisely modeling each eccentricity in behavior requires a great deal of effort and an unwarranted complexity in design. However, a recognition of the real piezoceramic properties will lead to a design which produces a more robust system.

We can conclude with the following statements concerning the use of piezoceramics as induced strain actuators. Steps to avoid depoling, as well as inclusion of repoling capability are straightforward and can be easily addressed in design of a system. Recognition of the real field-strain relation is necessary for most applications. A knowledge of hysteresis allows for better prediction of static performance. In vibratory applications, awareness of the variable lag in strain in response to field will allow for inclusion in the stability margins. Control and linearization of the hysteresis loop can be accomplished. In static applications, the ability to compensate for creep can be easily included with considerable benefits.

A characterization of the real piezoelectric strain behavior of piezoceramics can be achieved through simple laboratory tests. Such recognition

of real properties will aid in design of components using piezoceramic actuation strain as well as in diagnosing unmodeled or otherwise inexplicable actuator performance.

CHAPTER THREE: ONE-DIMENSIONAL INDUCED STRAIN ACTUATION

3.0 INTRODUCTION

The objectives of this chapter are to develop increasingly detailed models of the interaction between piezoceramics and beam-like substructures to which they are bonded or in which they are embedded, and to judge the accuracy of the models by comparison with experimental results. Three different models of increasing fidelity are presented. The models are compared to determine under what circumstances the higher fidelity ones are needed.

Piezoceramics are only one of a number of types of induced strain actuators. But while the method of inducing strain differs, all strain actuators share common mechanical features. When they are bonded to or embedded in a beam-like structure, both the actuators and structure extend, bend, and shear, depending on the magnitude of the actuation strain and the geometry and relative stiffnesses of the actuators, substructure, and bonding layers. The models developed in this chapter are therefore generally applicable to all induced strain actuators. In addition, they will be specifically applied to piezoelectric actuation. The realistic properties of the piezoceramics from the previous chapter are included in the analytical comparison with experimental results.

Previous models of surface bonded piezoceramic actuators (Crawley and de Luis, 1987, and de Luis and Crawley, 1985) considered the actuators as separate mechanical elements exerting forces on a rectangular beam-like substructure. The current models more accurately describe the full mechanical behavior of the actuators, allow for more general cross-section beam substructures, and are suitable for dynamic (vibration control) as well as quasisteady (shape control) applications.

Three different mechanical models of induced strain actuation are presented. In Fig. 3.1, the actuators are shaded, and the bold lines represent the strain distribution implicit in each model. The first includes only uniform extension in the actuators and is designated the uniform strain model (Fig. 3.1

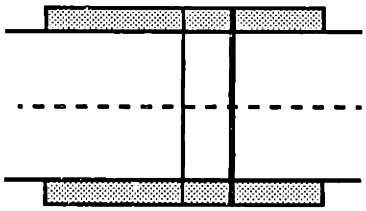

a) Uniform Strain Extension

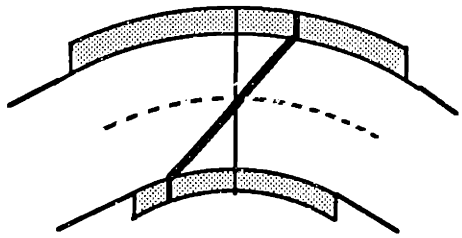

b) Uniform Strain Bending

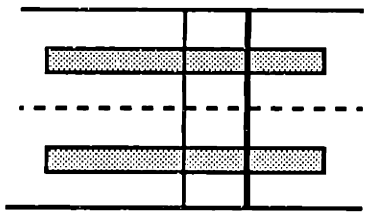

c) Bernoulli-Euler Extension

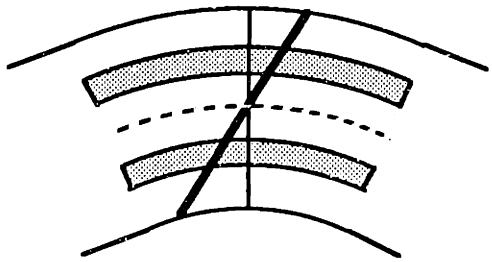

d) Bernoulli-Euler Bending

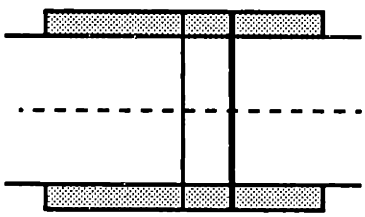

e) Bernoulli-Euler Extension

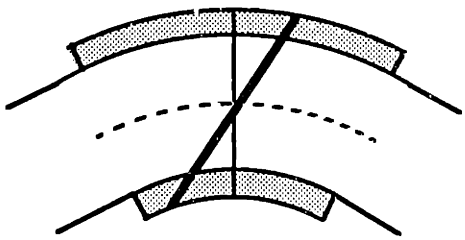

f) Bernoulli-Euler Bending

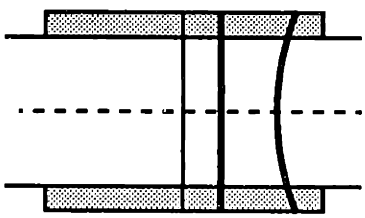

g) Finite Element Extension

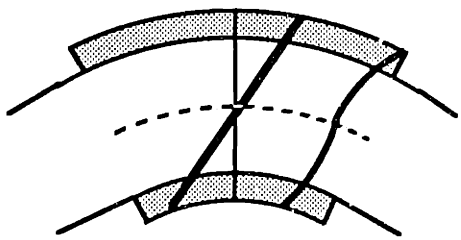

h) Finite Element Bending

Figure 3.1: Induced Strain Distributions in Models

a,b). The second model includes extension and bending in the actuators, and is called the Bernoulli-Euler or consistent strain model, in the sense that the strain assumption in the actuator is consistent with the Bernoulli-Euler assumption (c,d,e,f). The third, a finite element model, implicitly includes extension, bending, and shear in the actuator (g,h). In addition, the analytical models are developed for the general case which includes shear in the actuator/beam bonding layer, and for the limiting case of an ideal bond at the actuator/beam interface. The analytical results are compared for quantities such as induced strain and total displacement for typical substructures. The models are then correlated with oscillatory and quasisteady experiments.

In Chapter 2, the symbols 'S' and 'T' were used to designate strain and stress, in order to comply with the *IEEE Standard on Piezoelectricity* (1978) definitions. The symbol 'ε' was used to represent the dielectric coefficient. In this and subsequent chapters, the dielectric coefficient does not appear. In the mechanical derivations and models which follow, the symbol 'ε' will be used for strain and the symbol 'σ' for stress.

3.1 UNIFORM STRAIN MODEL

In this section, analytical models based on an assumed uniform strain in the actuator will be presented. The derivation of the perfectly bonded surface mounted actuator model for induced bending and extension in beams of arbitrary cross-section will be shown. The specialization of the bending model to rectangular cross-section beams will also be presented. Finally, the results of a model which incorporates shear lag in a bonding layer will be summarized.

Uniform strain is the designation given to the series of models developed by Crawley and de Luis (1987). This term is used because of the assumption that the strain in surface mounted actuators is uniform or constant through their thickness. The uniform strain model is accurate for the case of actuators inducing extension (Fig. 3.2a) in a one dimensional rod or beam. Neglecting shear in the beam, actuator, or bond layer, the strain in such elements is uniform across the cross-section. For strain-induced bending (Fig. 3.2b), the assumption that strain is uniform in the actuators (*i.e.* the actuators themselves extend or compress only) is a good approximation when the structure is much thicker than the actuators. However, for relatively thin structures, the approximation breaks

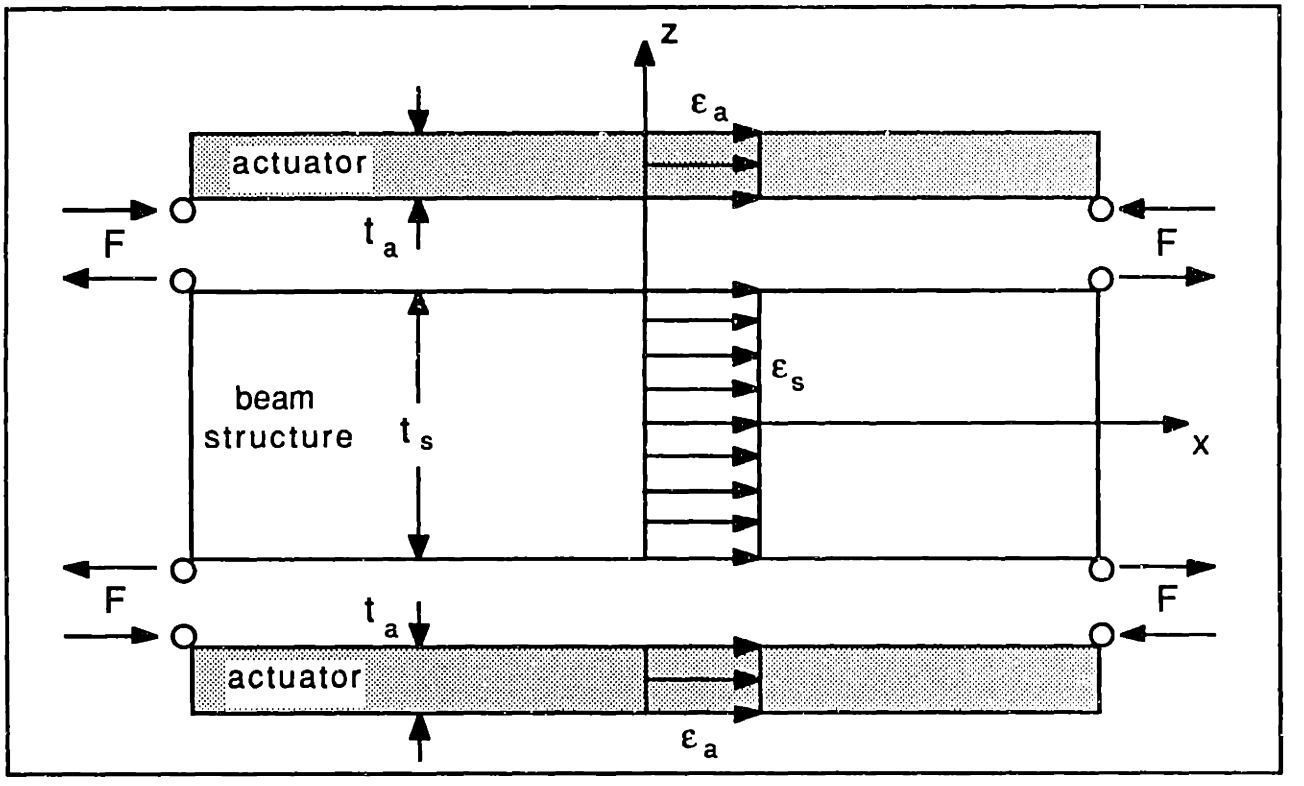

a) Induced Extension

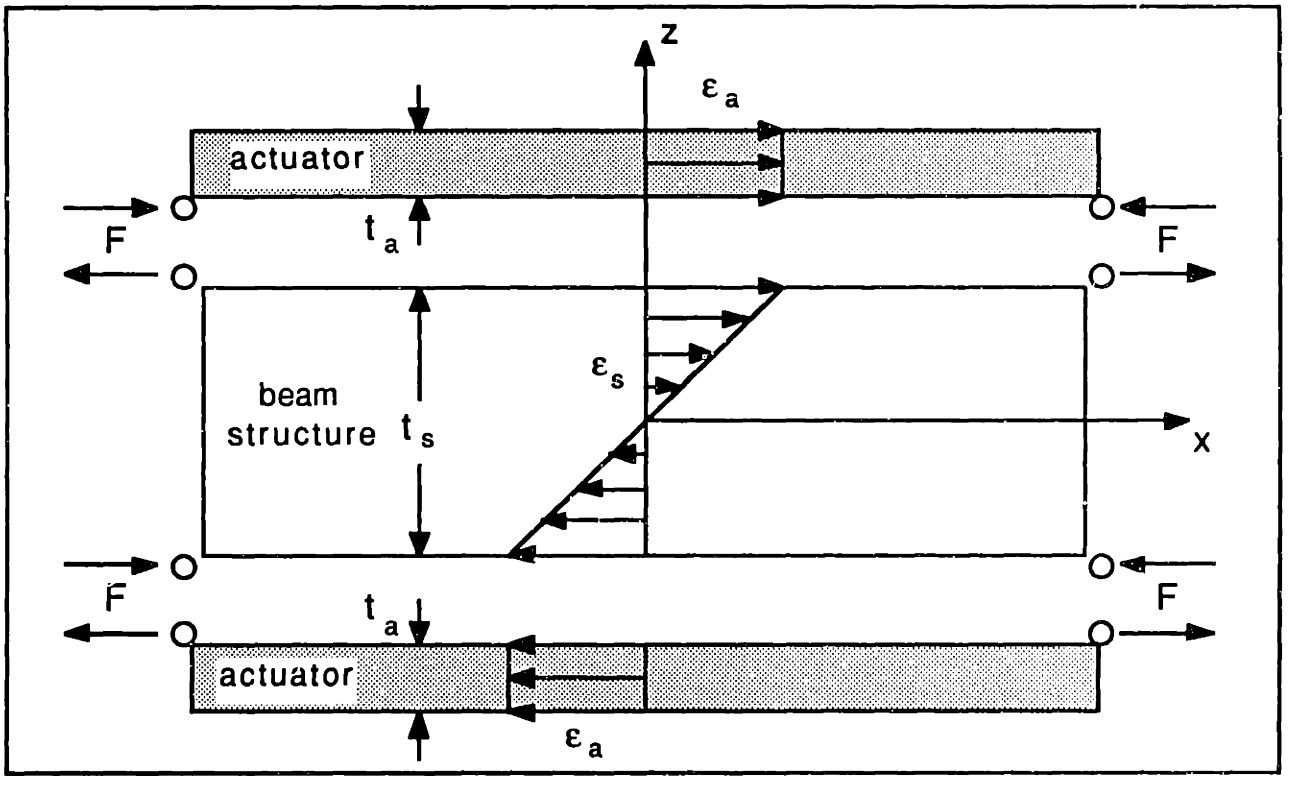

b) Induced Bending

Figure 3.2: Uniform Strain Model Geometry

down. The uniform strain models will be compared with other more general models in Section 3.4.

Perfectly Bonded Surface Models

As an example of the uniform strain approach, the derivation for the uniform strain model for induced bending with perfectly-bonded surface actuators acting on a beam with no external loads will now be summarized, after Crawley and de Luis (1987). The subscripts '*s*' and '*a*' will be used to refer to structure and actuator quantities. When a bonding layer of finite stiffness is present between the actuators and structure, the forces created by the strain actuator are transmitted by a shear stress which varies along the length of the actuator, but tends to be concentrated at the ends. In the limit, when there is a "perfect" bond at the actuator/structure interfaces, the forces created by the actuators are transmitted to the structure at concentrated points at the end of the actuator, which can be modeled as "pins." Examining the equilibrium of the structure of Fig. 3.2b, the forces F at the "pins" cause a moment to be applied to the structure of magnitude

$$M = -Ft_s \tag{3.1}$$

The beam, which is assumed to be in pure bending, has stress

$$\sigma_s^k(z) = -\frac{MzE^k}{(EI)_s} \tag{3.2}$$

where the superscript 'k' refers to the kth layer of a symmetric beam and $(EI)_s$ includes only the bending stiffness of the beam. If the beam is symmetric, then the stress at the top surface of the beam ($z=t_s/2$) is

$$\sigma_s^{surf} = \frac{Ft_s^2 E_s^{surf}}{2(EI)_s} \tag{3.3}$$

The actuator is assumed to uniformly extend without bending. Thus, the stress in the actuator is

$$\sigma_a = -\frac{F}{A_a} \tag{3.4}$$

The stress-strain relationships for the structure and actuator may be written

$$\varepsilon_s = \frac{\sigma_s^k}{E_s^k} \tag{3.5}$$

$$\varepsilon_a = \frac{\sigma_a}{E_a} + \Lambda \tag{3.6}$$

where Λ is the actuation strain caused by thermoelasticity, piezoelectricity, electrostriction, or another physical phenomenon. By requiring displacement compatibility at the upper actuator/structure interface, the strains there may be equated. Thus, if Eqs. 3.3 and 3.4 are inserted into Eqs. 3.5 and 3.6, and the latter two expressions are equated, the result for the pin force F is

$$F = -\frac{\Lambda}{\frac{t_s^2}{2(EI)_s} + \frac{1}{(EA)_a}} \tag{3.7}$$

and the induced strain in the upper actuator and the upper surface of the structure is

$$\varepsilon_s^{surf} = \varepsilon_a = \frac{1}{1 + \frac{2(EI)_s}{(EA)_a t_s^2}} \Lambda \tag{3.8}$$

which can be written

$$\varepsilon_s^{surf} = \varepsilon_a = \frac{6\Lambda}{6 + \psi_b} \tag{3.9}$$

where

$$\psi_b = \frac{12(EI)_s}{t_s^2 (EA)_a} \tag{3.10}$$

is a measure of the relative stiffnesses of the structure and one actuator. When the cross-section of the beam is rectangular

$$I_s = \frac{A_s t_s^2}{12} \tag{3.11}$$

and the relative stiffness parameter ψ_b for a rectangular beam is

$$\psi_b = \frac{(EA)_s}{(EA)_a} \tag{3.12}$$

The lower actuator and beam lower surface have induced strains

$$\varepsilon_s^{surf} = \varepsilon_a = -\frac{6\Lambda}{6 + \psi_b} \tag{3.13}$$

The curvature induced in the structure is

$$\kappa = -\frac{2}{t_s}\frac{6\Lambda}{6 + \psi_b} \tag{3.14}$$

In Fig. 3.3, the predicted normalized induced curvatures, $\kappa t_s/2\Lambda$, are plotted as a function of the structure-actuator thickness ratio, $T=t_s/t_a$, for three different modulus ratios (E_s/E_a = 1.0, 1.5, and 2.0). It is assumed that the rectangular beam and actuator widths are identical ($b_s=b_a$).

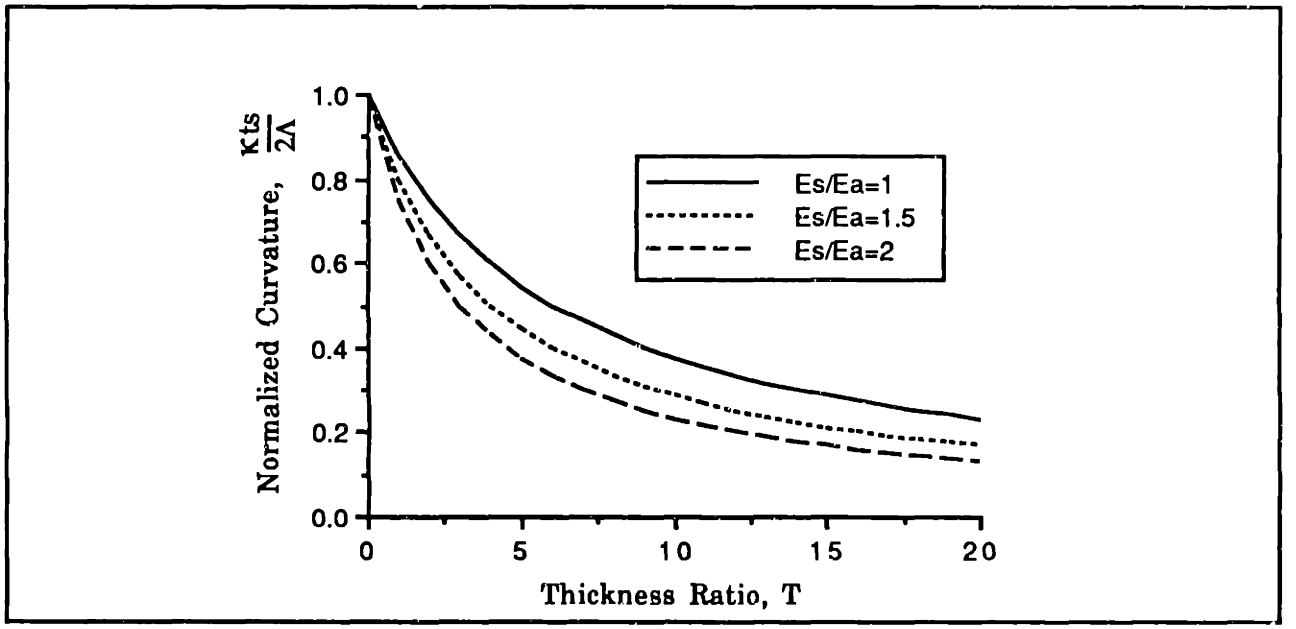

Figure 3.3: Normalized Induced Curvature for Uniform Strain Bending Model

The curvature is nondimensionalized so that it measures the induced beam surface strain as a fraction of the actuation strain. Examining Fig. 3.3, it is clear that for a fixed T, less strain can be induced in a structure with higher modulus. Based on the uniform strain model, it can be inferred that for maximum induced curvature, the ratio of structure-to-actuator thicknesses should be made small. For effective induced bending, the thickness ratio should be kept below the "knees" in the curves at about ψ_b=6. The results of Fig. 3.3 are at variance with the more accurate results of the Bernoulli-Euler model shown in Fig. 3.5 in Section 3.2.

The case of induced extension in a uniform strain model may be derived in a similar fashion (Crawley and de Luis, 1987). The resulting induced strain is

$$\varepsilon_a = \varepsilon_s = \frac{2\Lambda}{2 + \psi_e} \tag{3.15}$$

where

$$\psi_e = \frac{(EA)_s}{(EA)_a} \tag{3.16}$$

This result is valid for an arbitrary structure cross-section.

Surface Mounted Models with Bonding Layer

The results of the extension and bending models which include a finite stiffness bonding layer between the structure and actuators will now be summarized. An interpretation of those induced strain predictions will be used to determine losses in net displacements due to shear lags in the bonding layer.

In all cases, it is desirable to have a bond which is as stiff as possible when using surface-bonded actuators to induce strain in a structure. The potential losses due to shear lag in the bonding layer will be most significant if a particularly soft or thick adhesive layer is used. Because of the uniform strain assumption, Crawley and de Luis (1987) were able to treat the bonded extension and bending cases in the same manner. The predicted induced strains with the bonding layer included are

$$\frac{\varepsilon_a}{\Lambda} = \frac{\alpha}{\alpha + \psi}\left(1 + \frac{\psi}{\alpha}\frac{\cosh(\Gamma \bar{x})}{\cosh(\Gamma)}\right) \tag{3.17}$$

$$\frac{\varepsilon_s}{\Lambda} = \frac{\alpha}{\alpha + \psi}\left(1 - \frac{\cosh(\Gamma \bar{x})}{\cosh(\Gamma)}\right) \tag{3.18}$$

where $\bar{x}$ is the nondimensional coordinate along the length of the actuators, ranging from -1 at one end to +1 at the other, α=6 for bending and α=2 for stretching, and $\psi=\psi_e$ or ψ_b as appropriate. The meaning of ε_s is the strain in the bar for the case of induced extension, and on the surface of the beam for induced bending. The shear lag parameter Γ is

$$\Gamma^2 = \frac{\left(\frac{G_{bl}}{E_a}\right)\left(\frac{t_{bl}}{t_a}\right)}{\left(\frac{t_{bl}}{l_a}\right)^2}\left(\frac{\alpha + \psi}{\psi}\right) \tag{3.19}$$

where '*bl*' indicates a bonding layer quantity and α and ψ are chosen to be appropriate for extension and bending. The shear parameter gets larger when the bond has a greater shear modulus (G_{bl}), a smaller thickness (t_{bl}), or if the actuator length (l_a) is large. At the center of the actuators ($\bar{x}$ = 0) the strains in the structure and actuator are nearly equal and identical to the perfect bond value. At the actuator edges ($\bar{x}$ = ±1), the actuator strain is equal to the actuation strain, Λ, and the strain in the structure is zero. For the limiting case of large Γ (nearly a perfect bond), the predicted strains in Eqs. 3.17 and 3.18 approach the perfect bond strains of Eqs. 3.9 and 3.15.

When the strain in the structure (Eq. 3.18) is integrated from $\bar{x}$ = -1 to $\bar{x}$ = 1, for the case of induced extension, the total displacement u induced in the structure may be obtained

$$\frac{u}{l_a \Lambda} = \frac{2}{2 + \psi_e}\left(1 - \frac{1}{\Gamma_e}\frac{\sinh(\Gamma_e)}{\cosh(\Gamma_e)}\right) \tag{3.20}$$

where Γ_e is the value of Eq. 3.19 evaluated for extension (α=2). This expression provides a means of judging the net effect of shear layer losses. A similar result may be derived for the change in slope over the length of the actuator, when actuation is in bending

$$\frac{t_s}{2 l_a \Lambda}\frac{dw}{dx} = \frac{6}{6+\psi_b}\left(1 - \frac{1}{\Gamma_b}\frac{\sinh(\Gamma_b)}{\cosh(\Gamma_b)}\right) \tag{3.21}$$

which has the same form as Eq. 3.20. Equations 3.20 and 3.21 also give the net extension and slope change for a perfectly bonded actuator in the limit as Γ goes to zero.

The assumptions and derivations of surface-bonded actuators with uniform strain, under the conditions of both perfect and deformable bonds have been presented. These results will be used in comparisons with the other models in Section 3.4.

3.2 BERNOULLI-EULER MODEL

In this section, the strain induced in a beam by actuators undergoing Bernoulli-Euler like deformations will be derived. In this model, it is assumed that the entire cross-section, both structure and actuators, undergoes consistent Bernoulli-Euler strains, uniform for extension, and linear with z for bending. Models for induced stretching and bending with embedded actuators will be derived first. Then, the embedded models will be specialized to the case of surface bonded actuators. Finally, the finite bonding layer solution developed by Crawley and de Luis (1987) for the uniform strain model will be adapted for the Bernoulli-Euler model.

Embedded Actuator Models

The induced strain due to actuators embedded in a beam will now be derived. It is assumed that the actuators are perfectly embedded, *i.e.* there are no shear losses in transferring strain from actuator to substructure. It is further assumed that cutouts are made in the structure to physically accommodate the actuators, implying a change in the local stiffness.

Under these assumptions, the embedding of an actuator in a beam can be treated analogously to a beam with internal forces and moments generated by thermal strains (Rivello, 1969). Thermal strains are in fact just a special case of actuation strain. The geometry for a typical embedded actuator arrangement is defined in Fig. 3.4.

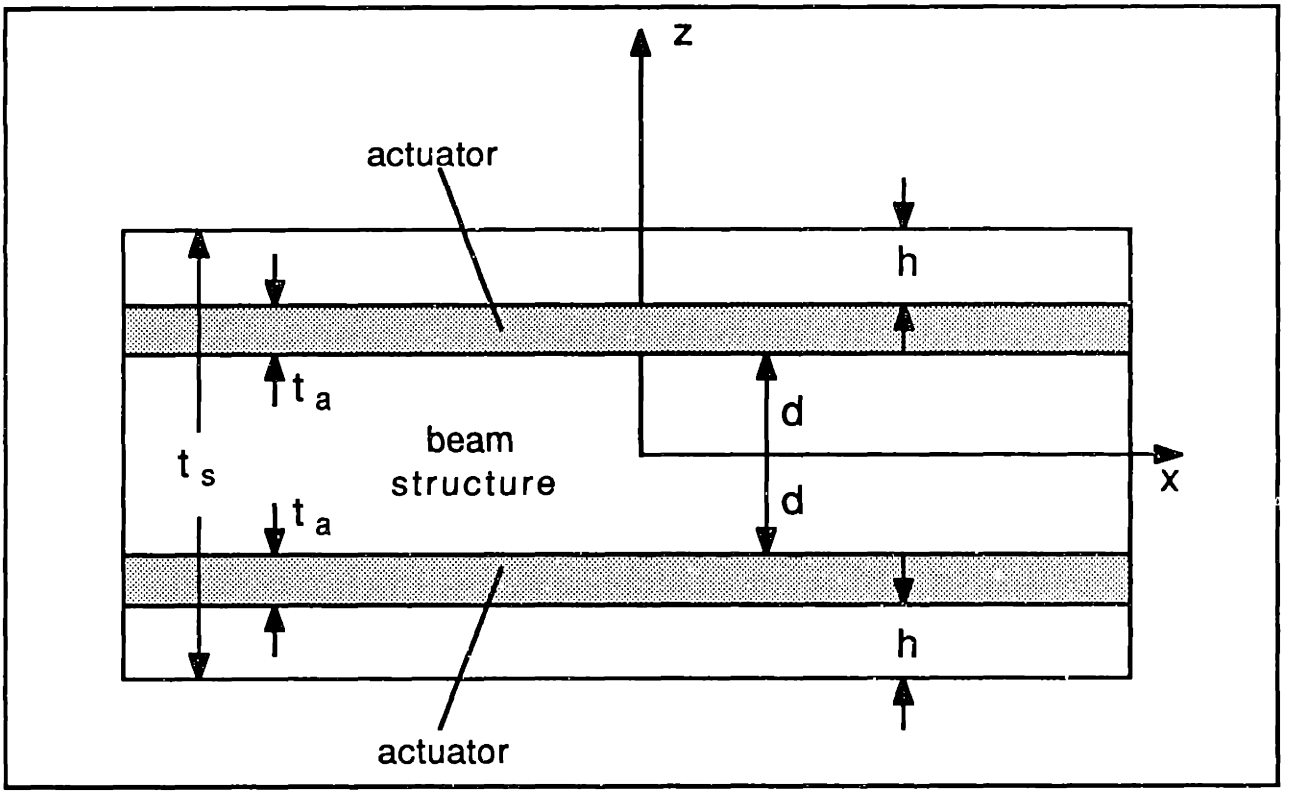

Figure 3.4: Geometry for Bernoulli-Euler Model with Symmetric Embedded Actuation

In beam notation, the assumed Bernoulli-Euler strains are

$$\varepsilon = \varepsilon_0 - z\kappa \tag{3.22}$$

and the constitutive property of the material in the cross-section is

$$E(z)\varepsilon(z) = \sigma(z) + E(z)\Lambda(z) \tag{3.23}$$

where, with reference to Fig. 3.4, the properties are those of the actuator when $d<|z|<d+t_a$, and those of the structural material elsewhere. Substitution of Eq. 3.22 into Eq. 3.23, and integration with respect to z yields

$$(EA)_{Total}\varepsilon_0 - (ES)_{Total}\kappa = P_m + P_\Lambda \tag{3.24}$$

or substitution, premultiplication by z, and integration yields

$$(ES)_{Total}\varepsilon_0 - (EI)_{Total}\kappa = M_m + M_\Lambda \tag{3.25}$$

where

$$(EA)_{Total} = \int_z E(z)b(z)dz \tag{3.26}$$

$$(ES)_{Total} = \int_z E(z)\,b(z)\,z\,dz \tag{3.27}$$

$$(EI)_{Total} = \int_z E(z)b(z)\,z^2 dz \tag{3.28}$$

are the total area stiffness, first and second moment of inertia respectively. The terms P_m and M_m are the resultants in equilibrium with the externally applied forces and moments

$$P_m = \int_z \sigma(z)\,dz \quad \text{and} \quad M_m = \int_z \sigma(z)\,z\,dz \tag{3.29}$$

The terms P_Λ and M_Λ are the internal forces and moments created by the actuation strain.

$$P_\Lambda = \int_z E(z)\Lambda(z)b(z)dz \tag{3.30}$$

$$M_\Lambda = \int_z E(z)\Lambda(z)b(z)\,z\,dz \tag{3.31}$$

Thus far, the derivation is applicable for arbitrary beam and actuator cross-sections. In the general case, the total strain energy, U, may be written

$$U = \tfrac{1}{2}\int_0^l \left([\varepsilon_0 \;\; \kappa] \begin{bmatrix} EA & ES \\ ES & EI \end{bmatrix} \begin{bmatrix} \varepsilon_0 \\ \kappa \end{bmatrix} - 2[P_\Lambda \;\; M_\Lambda] \begin{bmatrix} \varepsilon_0 \\ \kappa \end{bmatrix} \right) dx \tag{3.32}$$

For the idealized rectangular cross-section geometry of Fig. 3.4, in which both the beam and actuation are symmetric about the neutral axis, the extension and bending are uncoupled. Solution of the extension problem with no applied loads ($P_m = M_m = 0$) gives

$$(EA)_{Total} = E_s(b_s t_s - 2b_a t_a) + 2E_a b_a t_a \tag{3.33}$$

$$P_\Lambda = 2E_a b_a t_a \Lambda \tag{3.34}$$

and the induced extensional strain is

$$\varepsilon_0 = \frac{2E_a b_a t_a \Lambda}{E_s(b_s t_s - 2b_a t_a) + 2E_a b_a t_a} = \frac{2\Lambda}{2 + \psi_e} \tag{3.35}$$

where as before (Eq. 3.16)

$$\psi_e = \frac{(EA)_s}{(EA)_a} = \frac{E_s(b_s t_s - 2b_a t_a)}{E_a b_a t_a} \tag{3.36}$$

and account has now been taken for the removal of the material of the actuator in calculating $(EA)_S$.

Under the same conditions, the solution to the bending problem is

$$(EI)_{Total} = E_s\left(\frac{b_s t_s^3}{12} - 2I_a\right) + 2E_a I_a \tag{3.37}$$

$$I_a = A_a\left(d^2 + dt_a + \frac{t_a^3}{3}\right) \tag{3.38}$$

$$M_\Lambda = -2(EA)_a\left(d + \frac{t_a}{2}\right)\Lambda \tag{3.39}$$

and the induced bending strain is

$$\varepsilon = -\kappa z = \frac{2(EA)_a\left(d + \frac{t_a}{2}\right)\Lambda}{E_s\left(\frac{b_s t_s^3}{12} - 2I_a\right) + 2E_a I_a} z \tag{3.40}$$

The induced bending strain in any part of the structure (or actuators) can be found by simply using the appropriate value for z. This equation is not consistent with the derivation by Crawley and de Luis (1987) which assumed Bernoulli-Euler bending but simplified the problem by counting both the actuator stiffness and the structural stiffness at the location of the material cut out for the actuator.

Surface Mounted Models

Perfectly-bonded surface actuators inducing extension and bending strain are special cases of the Bernoulli-Euler model. In specializing the embedded model to the surface-bonded case, care must be taken to properly address the lack of a "cutout" when the actuators are mounted on the surface.

For the case of extension, the specialization is straightforward. The induced extensional strain is still

$$\varepsilon = \frac{2\Lambda}{2 + \psi_e} \tag{3.41}$$

where ψ_e is now

$$\psi_e = \frac{(EA)_s}{(EA)_a} = \frac{E_s b_s t_s}{E_a b_a t_a} \tag{3.42}$$

These expressions are identical to Eqs. 3.15 and 3.16, which were derived using the uniform strain model.

For the case of bending, the specialization is less obvious. The distance of the inner face of the actuator from the neutral axis becomes

$$d = \frac{t_s}{2} \tag{3.43}$$

and the term in the denominator of Eq. 3.40 is altered because there is no loss in bending stiffness due to a cutout in the structure. The induced bending strain is then

$$\varepsilon = -\kappa z = \frac{2(EA)_a\left(\frac{t_s}{2} + \frac{t_a}{2}\right)\Lambda}{E_s\left(\frac{b_s t_s^3}{12}\right)_s + 2E_a I_a} z \tag{3.44}$$

The correct moment of inertia for each of the surface-mounted actuators is

$$I_a = A_a\left(\frac{t_s^2}{4} + \frac{t_s t_a}{2} + \frac{t_a^2}{3}\right) \tag{3.45}$$

Putting Eq. 3.45 into Eq. 3.44, the induced strain becomes

$$\varepsilon = -\kappa z = \frac{12(t_s + t_a)\Lambda}{\left(\frac{(EA)_s}{(EA)_a} + 6\right)t_s^2 + 12t_s t_a + 8t_a^2} z \tag{3.46}$$

This expression can be further simplified if the stiffness ratio ψ (Eq. 3.12) and the thickness ratio, $T=t_s/t_a$, are used. For a rectangular cross-section beam, $\psi_b=\psi_e$, and the induced strain is

$$\varepsilon = -\kappa z = \frac{6\left(1+\frac{1}{T}\right)\Lambda\left(\frac{2}{t_s}\right)z}{(6+\psi)+\frac{12}{T}+\frac{8}{T^2}} \tag{3.47}$$

The similarity to the solution for the induced curvature or bending strain in the beam in the uniform strain model (Eq. 3.14) is obvious. Equation 3.47 however includes additional terms due to bending in the actuators. The additional terms in this equation are proportional to $(1/T)$. They become significant as T approaches zero, and are less significant when the beam is much thicker than the actuators. Figure 3.5 shows the surface strain for three different relative moduli (E_s/E_a=1.0, 1.5, 2.0). For convenience it is assumed that the structure and actuators have identical widths ($b_s=b_a$).

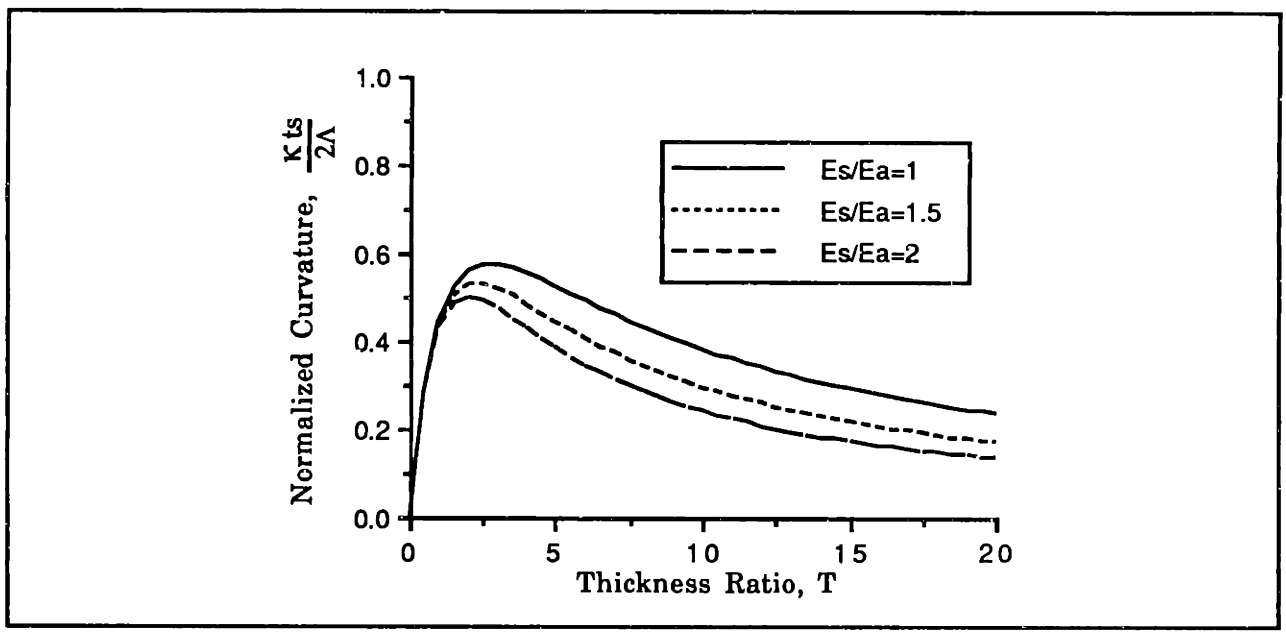

Figure 3.5: Normalized Induced Curvature for Bernoulli-Euler Bending Model

Surface Mounted Models with Bonding Layer

Crawley and de Luis (1987) developed a model which incorporated bonding layer shear lag into a bending model which assumed uniform strain in the actuators. The results were presented in Section 3.1.

In extension, the Bernoulli-Euler model is identical to the uniform strain model. Thus, the strains in the actuator and structure have the same form as Eqs. 3.17 and 3.18

$$\frac{\varepsilon_a}{\Lambda} = \frac{2}{2+\psi_e}\left(1+\frac{\psi_e}{2}\frac{\cosh(\Gamma_e \bar{x})}{\cosh(\Gamma_e)}\right) \tag{3.48}$$

$$\frac{\varepsilon_s}{\Lambda} = \frac{2}{2+\psi_e}\left(1-\frac{\cosh(\Gamma_e \bar{x})}{\cosh(\Gamma_e)}\right) \tag{3.49}$$

where $\bar{x}$ is defined along the length of the actuators and goes from -1 to +1. The "shear lag parameter" Γ_e for stretching is

$$\Gamma_e^2 = \frac{\left(\frac{G_{bl}}{E_a}\right)\left(\frac{t_H}{t_a}\right)}{\left(\frac{t_H}{l_a}\right)^2}\left(\frac{2+\psi_e}{\psi_e}\right) \tag{3.50}$$

where l_a is the length of the actuator and '*bl*' refers to the bonding layer.

For the case of bending, if the bonding layer is assumed to contribute no bending stiffness and is thin enough that it doesn't significantly change the distance of the actuators from the neutral axis, its effect is to reduce the overall curvature and add a component of pure extensional strain to the actuator. The strains are inferred to be

$$\frac{\varepsilon_a}{\Lambda} = \left(\frac{12}{t_s}z + \psi_b\frac{\cosh(\Gamma_b \bar{x})}{\cosh(\Gamma_b)}\right)\frac{\left(1+\frac{1}{T}\right)}{6+\psi_b+\frac{12}{T}+\frac{8}{T^2}}\left(1-\frac{\cosh(\Gamma_b \bar{x})}{\cosh(\Gamma_b)}\right) \tag{3.51}$$

$$\frac{\varepsilon_a}{\Lambda} = \frac{-z\kappa}{\Lambda} = \frac{12}{t_a}\frac{\left(1+\frac{1}{T}\right)z}{6+\psi_b+\frac{12}{T}+\frac{8}{T^2}}\left(1-\frac{\cosh(\Gamma_b\bar{x})}{\cosh(\Gamma_b)}\right) \tag{3.52}$$

reflecting the different strain distribution in the Bernoulli-Euler model, where Γ_b is now

$$\Gamma_b^2 = \frac{\left(\frac{G_{bl}}{E_a}\right)\left(\frac{t_H}{t_a}\right)}{\left(\frac{t_H}{L}\right)^2}\left(\frac{6+\psi_b+\frac{12}{T}+\frac{8}{T^2}}{\psi_b\left(1+\frac{1}{T}\right)}\right) \tag{3.53}$$

Expressions for net extensional displacement and net slope change analogous to Eqs. 3.20 and 3.21 may also be written for this model. The effect of a finite bond layer, as measured by the strain distribution along the actuator length as well as the net displacements, will be illustrated in Section 3.4.

Results for the Bernoulli-Euler models of embedded and surface-mounted actuators have been presented. The models were developed for both induced extension and induced bending. The results for the finite bonding layer shear lag model presented by de Luis were adapted to the Bernoulli-Euler model. Following the presentation of the finite element model in the next section, the results from the three models (uniform strain, Bernoulli-Euler, and finite element) will be compared in Section 3.4.

3.3 FINITE ELEMENT MODEL

The finite element model developed was the most detailed of the three models of induced strain actuator/structure interaction. It was used to model surface-mounted actuators both with and without explicit modeling of an elastic bonding layer. No additional insight is gained from the finite bonding layer model beyond that from the analytical models. Therefore, only the perfect bond model will be discussed. This model highlights the transfer of strain from actuator to structure and illustrates losses due to shear in both the actuators and structure. In Section 3.4, the finite element results will be compared with the results of the uniform strain and Bernoulli-Euler models. A description of the finite element model follows.

Details of the Model

A detailed two-dimensional finite element model of one half of a symmetric surface-mounted actuator/beam system was developed. The model was developed in ADINA (Automatic Dynamic Incremental Nonlinear Analysis) and executed on a Microvax. The actuators were each modeled with 40 (2x20) elements and the beam structure by 120 (4x30) or more depending on the beam thickness. A typical model is shown in Fig. 3.6. A finer mesh was used near the edges of the actuator in order to highlight the shear lag in the transfer of strain.

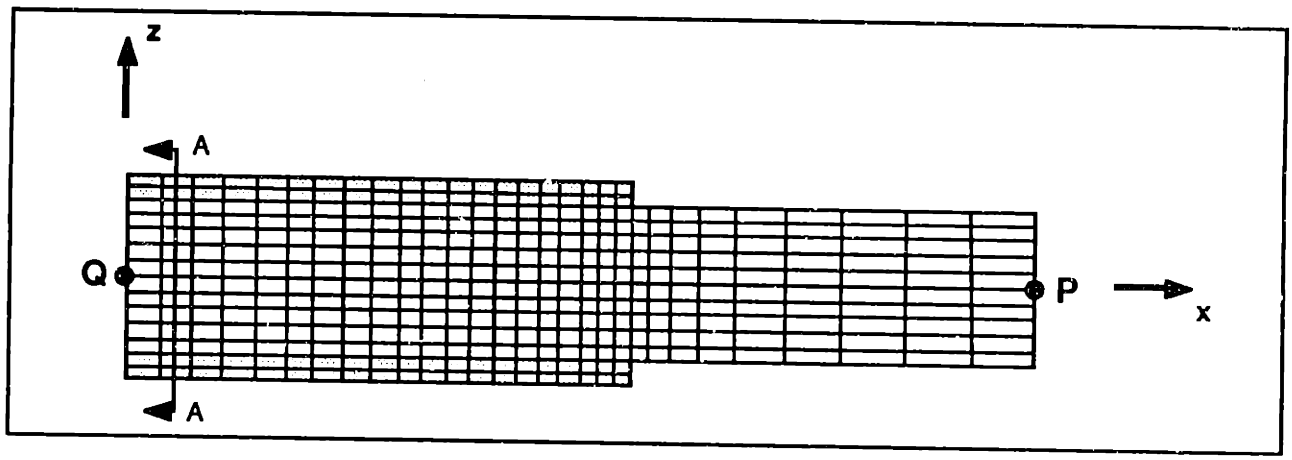

Figure 3.6: Typical Grid for ADINA Model (T=6.25)

Two-dimensional solid plane stress eight-node isoparametric elements were used. All the quadrilateral elements were rectangular. In the model, the elements used allowed only two degrees of freedom (x and z translation) per node. The left edge of the model was constrained in the x direction. Point Q at the center of the left edge was constrained in both the x and z directions.

The same basic model was used for induced bending and extension. The structure modeled was an aluminum beam (E_S = 70 GPa) with Piezoelectric Products G-1195 piezoceramic actuators. Beams of variable thickness were modeled. The actuator thickness was most often 10 mils (.254 mm), corresponding to the actuators used in the experiments (Section 3.6). The length of the actuator was 0.2 to 1.5 inches and the length of the structure 0.4 to 2.0 inches. Since an element with idealized piezoelectric properties was not available, the induced strain actuators were modeled with an isotropic thermoelastic material type. When a temperature (ΔT) was applied to the

structure and actuators, the actuators experienced a thermal actuation strain equal to

$$\Lambda = \alpha \Delta T \tag{3.54}$$

where α is the prescribed coefficient of thermal expansion and the actuation strain was uniform in the x and z directions. Since the model was linear, a single value for actuation strain (Λ=100μS) was used.

Because of the unavailability of a piezoelectric element, several modeling simplifications had to be made. The difference between the Young's modulus in the poling (z) direction and in the x direction of a piezoceramic could not be included in a thermoelastic material type. The material properties for a G-1195 piezoceramic are c^E_{11} = 63 GPa and c^E_{33} = 49 GPa. In the isotropic finite element, a value of 63 GPa, corresponding to the inplane modulus, was used. In addition, the thermoelastic element allowed for only a single value for the coefficient of thermal expansion. Thus $\alpha_x = \alpha_z = \alpha$. In real piezoceramics, the analogous d_{31} and d_{33} strain coefficients are not identical. They have both different magnitudes and different signs. However, the purpose of the model was to observe phenomena related to strain in the x direction. Because the actuators were thin and free to expand or contract in the z direction, it was believed that the inaccurate modeling of the piezoelectric effect in z would not significantly alter the results.

Extension was induced in the structure by specifying identical coefficients of thermal expansion for the upper and lower actuators. Bending was induced by specifying coefficients of thermal expansion equal in magnitude, but of opposite sign. In the next section, results from the finite element model will be compared with analytical results from the previous two sections.

3.4 COMPARISON OF MODELS

Three different models of induced strain actuation have been presented. The results for the uniform strain, Bernoulli-Euler, and finite element surface-mounted actuator models will now be compared for both induced extension and induced bending. The aim of the comparison is to determine over what range of parameters the simpler analytical models are valid.

The comparison of the surface-mounted models is organized to highlight the basic differences in the deformation of the structure predicted by each model. First, the actual strain induced in the structure, far from the edge of the actuators (Fig. 3.6, section A-A), will be compared. This is the most basic means of evaluating induced strain actuators. For this comparison, a perfect bond is assumed, and the influence of material shear is not significant because comparisons are made for strain far from the actuator edges.

Second, the influence of a finite stiffness bonding layer between actuators and structure will be highlighted. The strain distributions along the length of the actuators and structure will illustrate the shear lag introduced by the bonding layer. In addition, the reduction in net extension or change in slope due to the inclusion of finite bonds will be shown.

Third, the influence of a finite material shear will be highlighted. The analytical models, which include only extension and bending, will be compared to the finite element model, which also allows actuator and structure shear. The deformations and strains through the actuator and structure, as well as the total extensional or bending displacement, will be used to show the net loss due to material shear.

3.4.1 Induced Strain

The amount of strain induced in a structure is clearly a primary concern in induced strain actuation. The basic differences in strain distribution in the three perfect bond extension and bending models for the case of perfectly-bonded actuators were illustrated in Fig. 3.1. In the uniform strain model, it is assumed that the actuators strain uniformly. In the Bernoulli-Euler model, the actuators bend as well as extend. The finite element model allows extension, bending, and shearing in the actuator and structure.

For the case of extension induced by perfectly-bonded actuators, the formulas for induced strain for the uniform strain (Eq. 3.15) and Bernoulli-Euler (Eq. 3.41) models are identical

$$\varepsilon_a^{US} = \varepsilon_a^{BE} = \frac{2\Lambda}{2 + \psi_e} \tag{3.55}$$

There is no analogous formula for the finite element model. The predicted induced strain is shown in Fig. 3.7 for the analytical (Eq. 3.55) and finite element models for an aluminum structure and G-1195 actuators (E_s/E_a=1.111) with identical widths and a range of structure to actuator thickness ratios, $T=t_s/t_a$. For the finite element model, the strain away from the actuator edge at section A-A in Fig. 3.6 is used. In Fig. 3.7, the six points representing the finite element results coincide with the curve representing the analytical prediction. The difference between the analytical and finite element models is less than 0.1%.

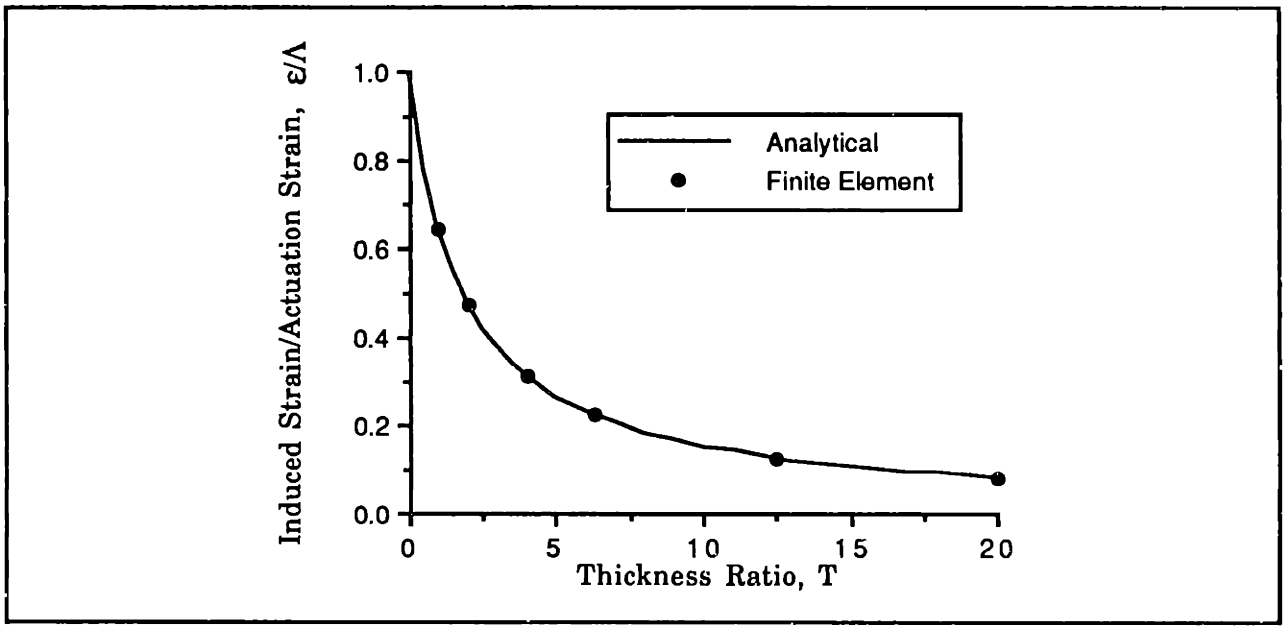

Figure 3.7: Comparison of Induced Extension Strains From Analytical and Finite Element Models

For the case of induced bending, the two analytical models are different. The predicted induced strains in the structure for the uniform strain (Eq. 3.9) and Bernoulli-Euler models (Eq. 3.47) with surface-bonded actuators are

$$\varepsilon_s^{US} = -\kappa_s^{US} z = \frac{6\Lambda}{6+\psi_b}\frac{2}{t_s} z \tag{3.56}$$

$$\varepsilon_s^{BE} = -\kappa_s^{BE} z = -\frac{6\left(1+\frac{1}{T}\right)\Lambda}{6+\psi_b+\frac{12}{T}+\frac{8}{T^2}}\frac{2}{t_s} z \tag{3.57}$$

For the Bernoulli-Euler model the predicted induced strain depends on both the relative stiffness, ψ_b, and the thickness ratio, T. The $1/T$ term in the numerator represents the additional moment arm from the structure surface (where the "pin forces" of the uniform strain model are located) to the midpoint of the actuators. The extra terms in the denominator are due to the inclusion of the full bending stiffness of the actuators. For the purpose of comparison, the assumption is made that the widths of the structure and actuators are equal. That is,

$$\frac{A_s}{A_a} = \frac{t_s}{t_a} = T \tag{3.58}$$

The induced strains are then

$$\varepsilon_s^{US} = -\kappa_s^{US} z = \frac{6\Lambda}{6 + \bar{E}T} \frac{2}{t_s} z \tag{3.59}$$

$$\varepsilon_s^{BE} = -\kappa_s^{BE} z = \frac{6\left(1 + \frac{1}{T}\right)\Lambda}{6 + \bar{E}T + \frac{12}{T} + \frac{8}{T^2}} \frac{2}{t_s} z \tag{3.60}$$

where $\bar{E} = E_s/E_a$. Thus, for given actuator and structure moduli, the predicted strain for each model depends only on T. For the case of an aluminum structure and G-1195 actuator, ($\bar{E}$ =1.111), the predicted curvatures are compared to the curvatures predicted by the finite element model far from the actuator edges. In Fig. 3.8, the curvatures are normalized so they represent surface strain in the beam.

The difference between the Bernoulli-Euler and finite element model is less than 0.1% over the entire range. For large T, all the models give nearly the same result, but agreement of the uniform strain model is not precise. For example, for a thick beam (T=20), the uniform strain model predicts a curvature 2.7% *below* the others. For small T, as the structure becomes vanishingly thin, the Bernoulli-Euler and finite element models predict structure surface strain which approaches 0, while the uniform strain model incorrectly predicts structure surface strain approaching the actuation strain. The uniform strain model significantly overestimates the strain because it does not correctly

represent the full actuator stiffness. For stiffer structures (*i.e.* $\bar{E}$ larger than 1.111) the uniform strain model matches the Bernoulli-Euler model better, but remains inaccurate for very small T. Based on the comparison of predicted induced strains the Bernoulli-Euler model appears to be accurate over the practical range of thickness ratios. The uniform strain model is nearly as accurate for large T, but is not adequate for thin structures.

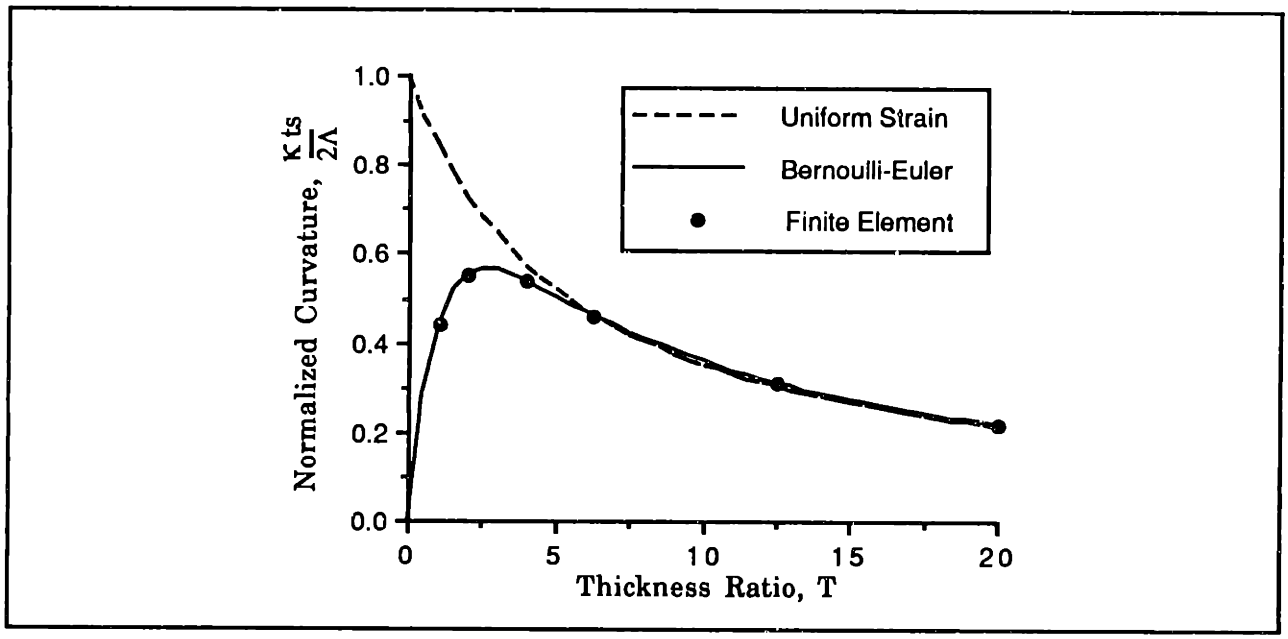

Figure 3.8: Comparison of Induced Bending Strains From Analytical and Finite Element Models

In most cases, the strain or curvature *in the structure* is of primary concern. If the strain at the surface of the actuator is important, the Bernoulli-Euler model should be used, with the appropriate value for z placed in Eq. 3.47. The uniform strain model is not adequate in predicting actuator surface strain (Fig. 3.1), especially for thin structures.

3.4.2 Influence of Finite Stiffness Bonding Layer

Inclusion of a finite stiffness bond between actuators and structure will reduce the effectiveness of induced strain actuators mounted on the surface of a structure. In Sections 3.1 and 3.2, the results for the uniform strain and Bernoulli-Euler models with a finite bonding layer were presented. Here, the extension model (identical for uniform strain and Bernoulli-Euler) and the Bernoulli-Euler bending model with finite stiffness bond layers will be compared to the corresponding perfect bond models. The extension case provides a more

straightforward illustration of the bonding layer shear lag phenomenon, and will therefore be the primary focus. Explicit expressions for the importance of the finite bond effect will be developed.

The induced extension and bending strains for the Bernoulli-Euler model with finite bonds from Eqs. 3.18 and 3.52 are

$$\frac{\varepsilon_s}{\Lambda} = \frac{2}{2+\psi_e}\left(1 - \frac{\cosh(\Gamma_e \bar{x})}{\cosh(\Gamma_e)}\right) \tag{3.61}$$

$$\frac{\varepsilon_s}{\Lambda} = \frac{-z\kappa_s}{\Lambda} = \frac{6\left(1+\frac{1}{T}\right)\frac{2}{t_s}z}{6+\psi_b+\frac{12}{T}+\frac{8}{T^2}}\left(1 - \frac{\cosh(\Gamma_b \bar{x})}{\cosh(\Gamma_b)}\right) \tag{3.62}$$

where

$$\Gamma_e^2 = \frac{\left(\frac{G_{bl}}{E_a}\right)\left(\frac{t_{bl}}{t_a}\right)}{\left(\frac{t_{bl}}{l_a}\right)^2}\left(\frac{2+\psi_e}{\psi_e}\right) \tag{3.63}$$

$$\Gamma_b^2 = \frac{\left(\frac{G_{ad}}{E_a}\right)\left(\frac{t_{ad}}{t_a}\right)}{\left(\frac{t_{ad}}{L}\right)^2}\left(\frac{6+\psi_b+\frac{12}{T}+\frac{8}{T^2}}{\psi_b\left(1+\frac{1}{T}\right)}\right) \tag{3.64}$$

and $\bar{x}$ is the nondimensional coordinate along the length of the actuator, ranging from -1 at one end to +1 at the other. When the shear lag parameter, Γ, becomes large, the second terms of Eqs. 3.61 and 3.62 become small and strains nearly equal to those which are obtained with a perfect bond are achieved. The parameter increases for a longer actuator and a thinner and higher shear modulus bond layer. In addition, a stiffer actuator (larger E_a,t_a) or a stiffer structure (larger E_s,t_s) will decrease Γ. For given adhesive properties, the effect of the finite bond is greatest when the most strain energy is being transferred (see Section 3.5). This occurs at ψ_e=2 for the extension case and depends on $\bar{E}$ for the bending case.

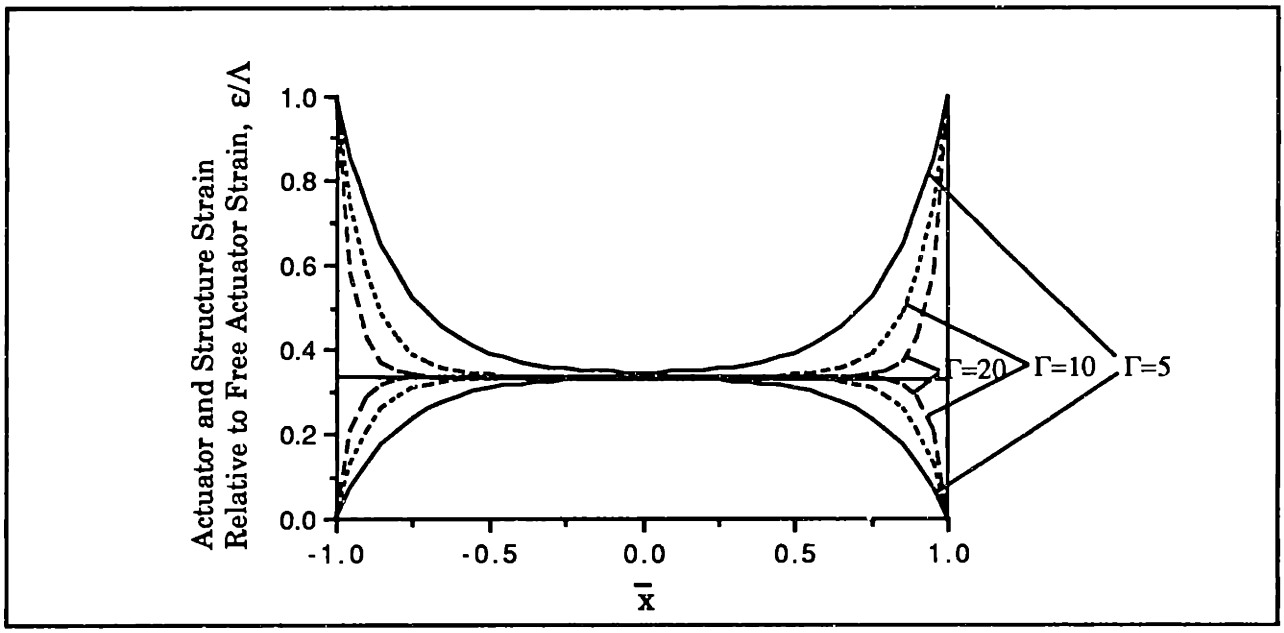

Figure 3.9: Extensional Strain Induced in Structure and Actuator with Finite Bonding Layer Stiffness Characterized by Shear Parameter, Γ

Figure 3.9 shows the extensional strain given by Eq. 3.61 for induced extension. A value of ψ_e=4.444, corresponding to $\bar{E}$ =1.111 (aluminum structure and G-1195 actuator) and T=4 is used. Three different values of Γ_e (5, 10, and 20) are shown. The upper curves represent the strain in the actuator. The lower curves, representing induced strain in the structure, illustrate the reduction in strain near the actuator edges. The perfect bond model predicts a constant normalized strain of .310 along the actuator length. An analogous plot of the bending case would appear nearly identical. For $\bar{x}$ =0, the strains in the structure and actuator are nearly identical to those for the perfect bond value. At the actuator edges ($\bar{x}$ = ±1), the strain in the actuator is equal to the actuation strain, Λ, and the strain in the structure is zero.

While the induced strain distribution is informative, the net induced *displacement* may be a more indicative measure of shear losses, because the net displacement sums strains over the full length of the actuators. When the strain in the structure (Eq. 3.16) is integrated from $\bar{x}$ = -1 to $\bar{x}$ = +1, the total displacement u induced in the structure may be obtained (Eq. 3.20), where Γ_e is given by Eq. 3.63. In contrast, the normalized induced displacement obtained by integrating the perfect bond strain (Eq. 3.15) is

$$\frac{u}{l_a \Lambda} = \frac{2}{\psi_e + 2} \tag{3.65}$$

By dividing Eq. 3.20 by Eq. 3.65, the fraction of the perfectly-bonded displacement achieved in the case of a finite bonding layer stiffness is obtained, and is plotted in Fig. 3.10. For large Γ, the effect of the bond is minimized. The difference from 1 on the curve is due to less than ideal strains induced in the beam, as indicated in Fig. 3.9, integrated over the actuator length.

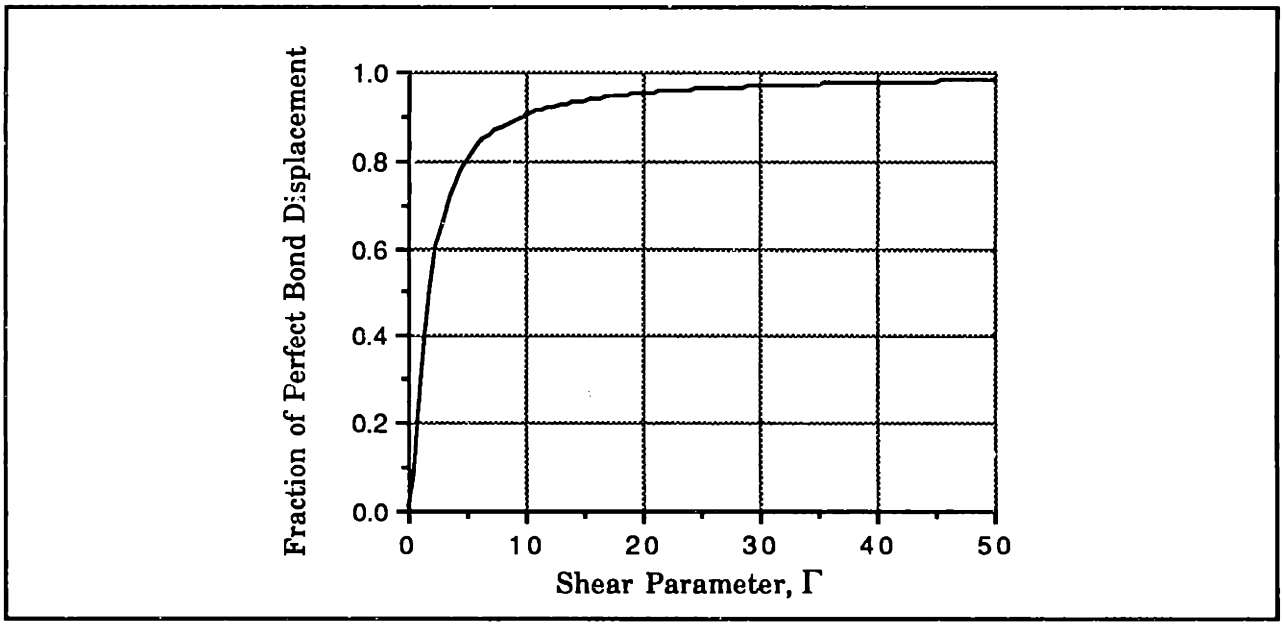

Figure 3.10: Effect of Shear Lag in Finite Stiffness Bonding Layer on Net Induced Displacement

A similar result may be derived for the change in net slope over the length of the actuator, when actuation is inducing bending. For simplicity and easy analogy with the extension case, the uniform strain model is used, and Eq. 3.21 may be obtained. Dividing Eq. 3.21 by the normalized induced change in slope for a perfectly bonded actuator,

$$\frac{t_s}{2l_a\Lambda}\frac{dw}{dx} = \frac{6}{\psi_b + 6} \tag{3.66}$$

The same functional form shown in Fig. 3.10 is obtained.

For even moderate values of Γ, it can be assumed that $\cosh(\Gamma) \approx \sinh(\Gamma)$ (they agree within 0.5% for Γ=3 and 0.01% for Γ=5). The fraction of the perfect bond displacement or slope change achieved is simply

$$\eta_{disp} = 1 - \frac{1}{\Gamma} \tag{3.67}$$

where either Γ_e or Γ_b is used. By integrating the square of the induced strain over the actuator length, the efficiency of strain energy transfer may be obtained. Assuming Γ>5, the energy transfer efficiency is

$$\eta_{energy} = 1 - \frac{2}{\Gamma} \tag{3.68}$$

where the efficiency is again 1 for a perfect bond. Thus, for example, 95% of the perfect bond displacement and 90% of the perfect bond strain energy transfer can be achieved for Γ=20.

3.4.3 Influence of Finite Material Shear

Finite shear in the actuators and structure will also reduce the effectiveness of the actuation, but due to assumed deformations, is not included in the analytical models. In the finite element model, however, shear in the actuators and structure is implicitly included. In this subsection, a perfect bond is assumed.

The shear is evident in Fig. 3.11, which shows the deformation of the finite element model in the region near the actuator edge for extension induced by a perfectly bonded actuator. The results shown are for a thickness ratio, T=6.25. Initially, the elements are all rectangular. The deformed elements shown illustrate the exaggerated displacement in the x direction only. Near the actuator edge, the actuator strains more than the structure. There is a shear lag in transferring the strain both from the actuator to the structure and then through the thickness of the structure. Away from the edge, the strain across the section is nearly uniform, as would be predicted by the analytical models.

Figure 3.12 shows the strain at the midline and upper surface of the beam, and at the upper surface of the actuator. For induced extension (a), the strains are normalized by the actuation strain, Λ, and are plotted versus the x distance from the edge of the actuator normalized by the actuator thickness, t_a. For induced bending (b), the abscissa is the same, but the ordinate shows the curvature normalized by the actuation strain, Λ, and the z location of the beam surface, $t_s/2$.

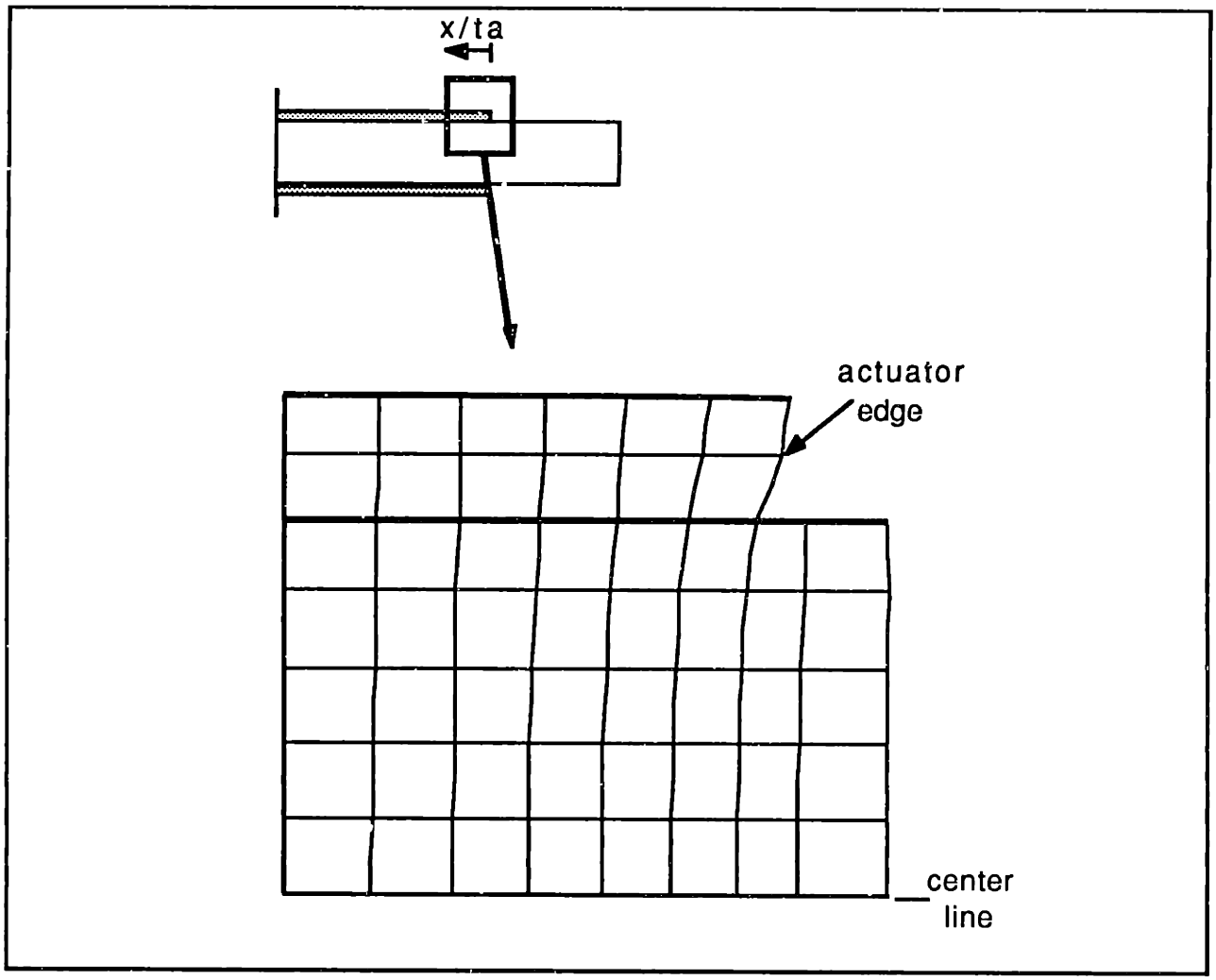

Figure 3.11: Deformation of Finite Element Model in Induced Extension Showing Evidence of Shear Through Actuator and Structure

In Fig. 3.12a, at the free edge of the actuator (x/t_a=0), the upper surface of the actuator deforms with a strain equal to the actuation strain. Away from the edge (x/t_a>0), the actuator surface strain rapidly approaches the value of the perfectly-bonded induced strain of Eq. 3.15. The midline of the structure begins to strain before the edge of the actuator, and also approaches the analytical induced strain within several actuator thicknesses. The beam surface strain actually has a small compression spike near the edge of the actuator before reaching the induced strain. Figure 3.12b shows normalized curvatures for induced bending. It has the same form as the induced extension curves (a), with shear lags in both the actuator and beam structure possessing comparable characteristic lengths.

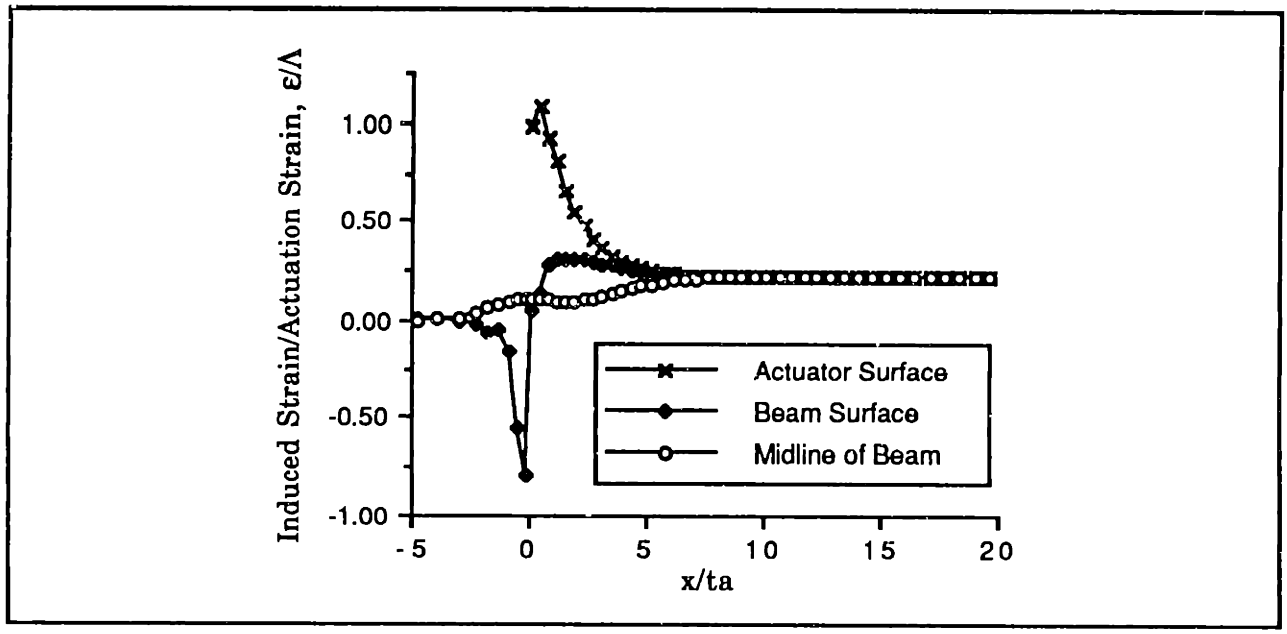

a) Induced Extension

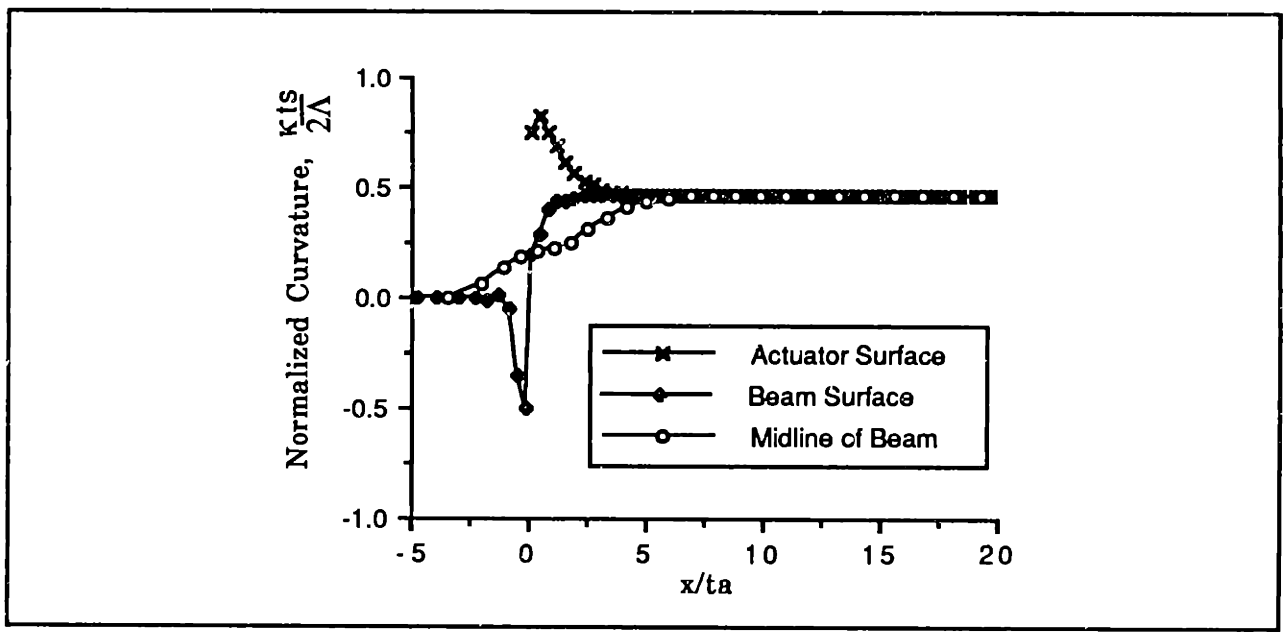

b) Induced Bending

Figure 3.12: Strains in Actuator and Structure Along Actuator Length Predicted By Finite Element Model (T=6.25)

The strain information illustrates local shear effects, however, the axial displacement u for a point far from the actuator can once again be used as an indicator of the net effect of the actuation. Figure 3.13 shows the axial deflection u for the finite element model (point P in Fig. 3.6), divided by the displacement for the perfectly-bonded model (Eq. 3.65). Results were obtained for actuator

aspect ratios ($AR=l_a/t_a$) of 40, 100, 150, and 250, and for a range of thickness ratios ($T=t_s/t_a$).

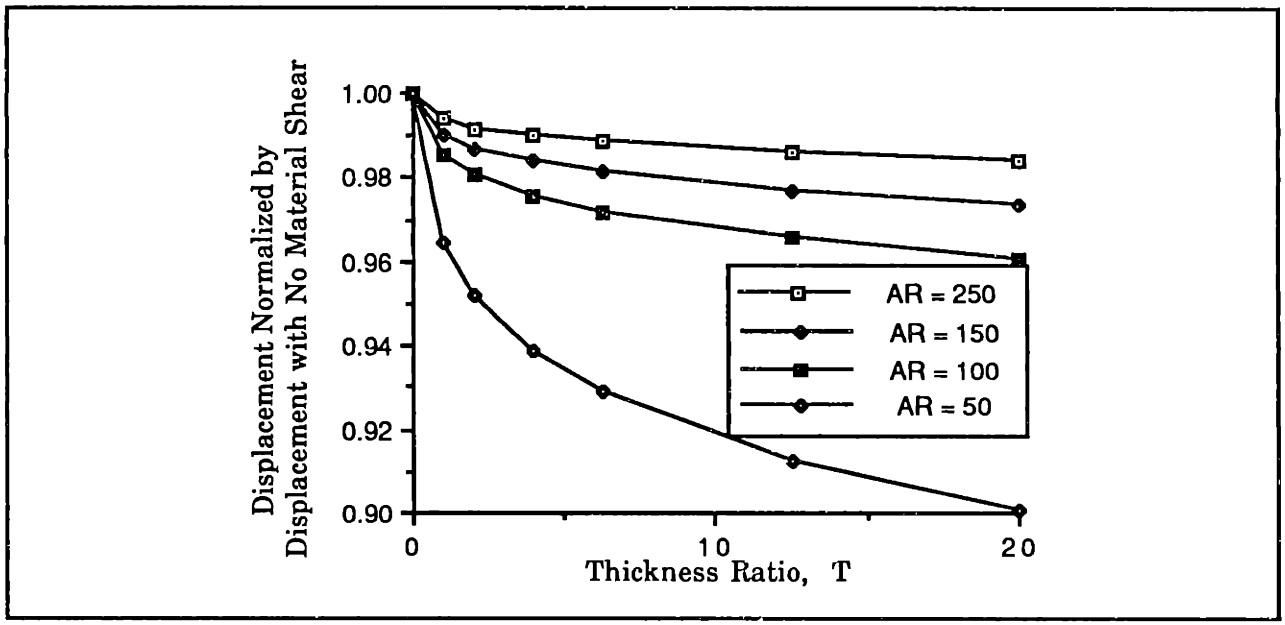

Figure 3.13: Normalized Net Induced Displacement for Variable Actuator Length and Beam Thickness

The fraction of the perfectly-bonded uniform strain model displacement achieved decreases for thicker beams (larger T) and shorter actuators (smaller AR). But for typical actuator geometries, the fraction of the ideal displacement achieved is near unity.

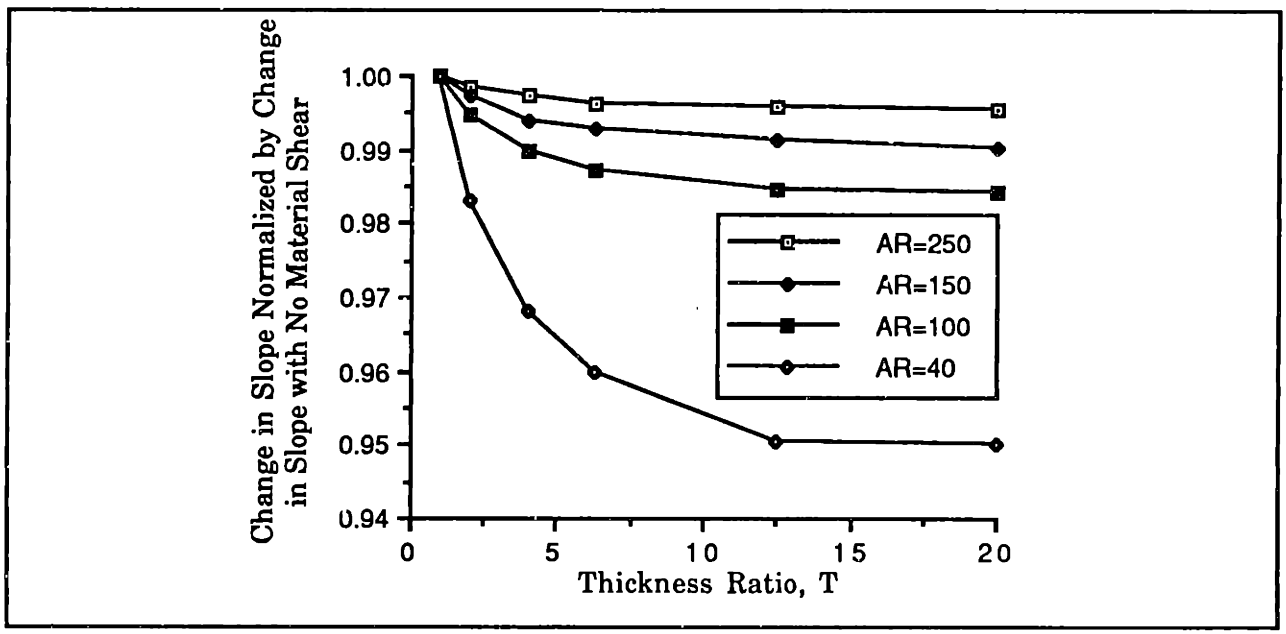

Figure 3.14: Normalized Net Induced Slope Change for Variable Actuator Length and Beam Thickness

For the bending case, a representative measure is the net change in the slope of the beam. That change in the slope (dw/dx) is determined by integrating the induced curvature over the length of the actuator. For the case of a perfect bond where the curvature is assumed constant over the length of the actuator, the change in slope is given by Eq. 3.66, which depends directly on the single value for curvature (or induced bending strain).

There was no discernable difference between the finite element and Bernoulli-Euler predictions for induced strains in Fig. 3.8 because a comparison of strains far from the edge was used. In the net slope change measure, there is a clear difference. Fig. 3.14 shows the results for typical aspect and thickness ratios. The same trends as in Fig. 3.13 are apparent, but the overall effect of the shear losses is less significant in bending (roughly half the reduction of the extension case). This is due in part to the more efficient strain energy transfer in bending for this particular geometry (see Section 3.5). Also, in bending, larger normal strains are induced, and thus, the shear is a smaller factor.

In summary, four comparisons among the models were made. For extension induced by perfectly bonded surface actuators, all three models predict nearly identical extensional strains away from the edges of the actuator. For induced bending, the Bernoulli-Euler and finite element models predict nearly identical curvature, while the uniform strain model overpredicts the curvature for thin beams. Actuators bonded with layers of finite stiffness yield more than 95% of the net displacement of the perfectly-bonded model, provided the shear lag parameter Γ exceeds 20. For realistic thickness ratios, and actuator aspect ratios in excess of 100, the consideration of actuator and beam material shear still yields net displacements within 5% of the idealized model. This implies that for practical engineering analysis, the perfectly bonded Bernoulli-Euler model is sufficient. Results of experiments will be correlated using the Bernoulli-Euler bending model. In addition, evidence of the finite bond layer will be presented. In the next section, guidelines for achieving the greatest efficiency with induced strain actuators will be developed.

3.5 EFFICIENT INDUCED STRAIN ACTUATION

An objective of this section is to provide a means of judging the relative "efficiency" of various actuator/structure combinations. At least two measures of efficiency are available. The induced strain energy may be used as a general measure of efficiency. The maximum strain energy which can be transferred from actuators to structure depends on relative stiffnesses and geometry. The total deformation was used in the previous section to determine effectiveness. In the present section, it will be the basis for another comparison - the relative merit of embedded versus surface-mounted actuators.

In this section, results for maximizing effectiveness of induced strain actuators will be presented. The surface-mounted Bernoulli-Euler models will be used to illustrate the efficiency of strain energy transfer. Then, the relative effectiveness of embedding actuators for shape control applications will be discussed.

Strain Energy Transfer

The induced strain is a means of evaluation which is often of concern, but the efficiency of strain energy transfer is in some ways more indicative of the effectiveness of the actuator. In a vibration control problem for example, the total energy of the system must be minimized. The strain energy transfer will be compared for the analytical models only.

The efficiency of strain energy transfer is defined as follows:

$$\eta = \frac{\text{induced strain energy in structure}}{\text{maximum available energy}}$$

For actuators inducing extension the strain energy in the structure is

$$U_s = \tfrac{1}{2}\int_s \sigma_s(x)\varepsilon_s(x)dV_s = \tfrac{1}{2}\int_s E_s\varepsilon_s^2(x)dV_s \tag{3.69}$$

where the strain in the structure is given for a pair of perfectly bonded actuators by Eq. 3.15. Inserting the correct strain, the strain energy becomes

$$U_s = 2(EA)_s l \frac{\Lambda^2}{(2 + \psi_e^2)} \tag{3.70}$$

where l is the length of the actuators.

The maximum available energy occurs if the full actuation strain is achieved in the presence of stress. That is

$$U_{av} = 2\left(\tfrac{1}{2}\int_s (E_a \Lambda)\Lambda \, dV_s\right) = (EA)_a l \Lambda^2 \tag{3.71}$$

where the factor of 2 is present to account for both actuators. The efficiency in extension is then just Eq. 3.70 divided by Eq. 3.71, or

$$\eta_e = \frac{2\psi_e}{(2 + \psi_e)^2} \tag{3.72}$$

Figure 3.15 shows this efficiency as a function of ψ_e (Eq. 3.16). For the perfectly-bonded extension models, a relative stiffness of 2 transfers the maximum energy. Strain energy transfer drops off rapidly for lower ψ_e, but slowly for stiffer structures (larger ψ_e). If an induced strain actuator with low modulus such as PVDF piezoelectric film is used, ψ_e will be very high and little strain energy can be transferred.

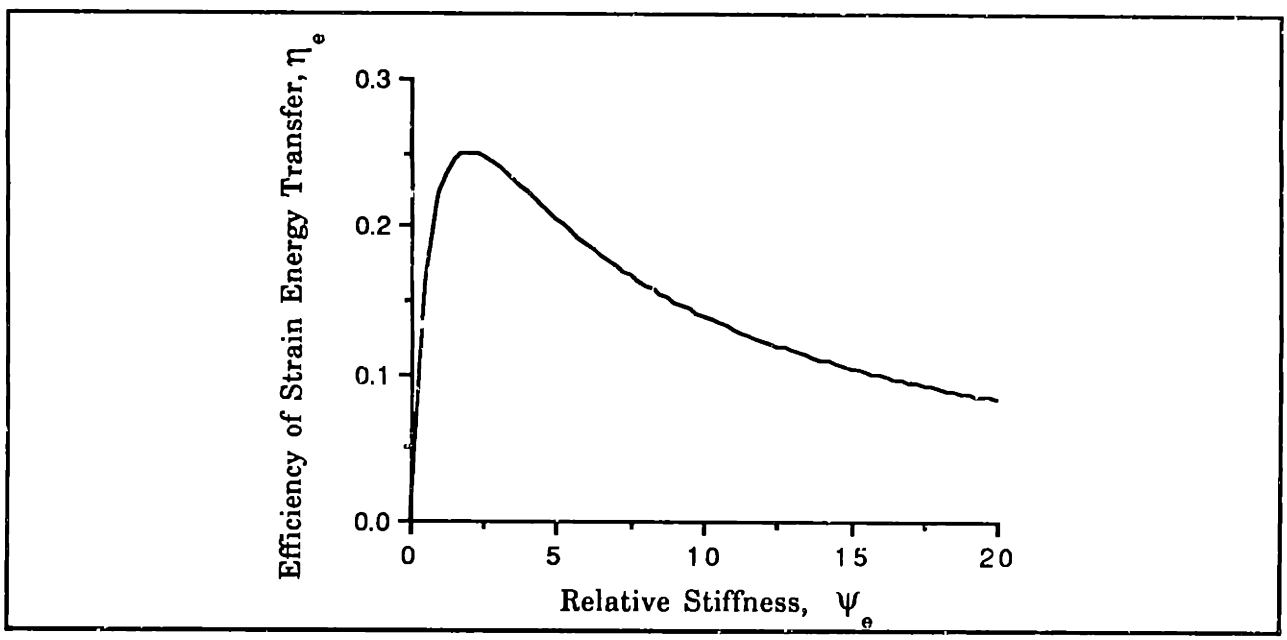

Figure 3.15: Efficiency of Strain Energy Transfer for Extension Induced by Surface-mounted Actuators

For the case of bending, the amount of available energy (Eq. 3.71) remains the same. The strain energy in the structure is still represented by Eq. 3.69, but Eq. 3.47 is now substituted for the strain, with the result

$$U_s = 72(EI)_s\, l\, \frac{\Lambda^2}{(6+\psi_b)^2} \tag{3.73}$$

Dividing Eq. 3.73 by Eq. 3.71, the resulting efficiency for bending is

$$\eta_b = \frac{6\psi_b\left(1+\frac{1}{T}\right)^2}{\left(6+\frac{12}{T}+\frac{8}{T^2}+\psi_b\right)^2} \tag{3.74}$$

where ψ_b is defined in Eq. 3.10. This expression depends not only on the relative stiffness, ψ_b, but also on the relative moduli of the materials, $\bar{E}$. Figure 3.16 shows the large variation in efficiency depending on the modulus ratio, assuming identical actuator and structure widths and a rectangular cross-section. For high modulus structures, the peak efficiency occurs at a larger value of ψ_b. The efficiency for bending does not drop off for large T as rapidly as the extension

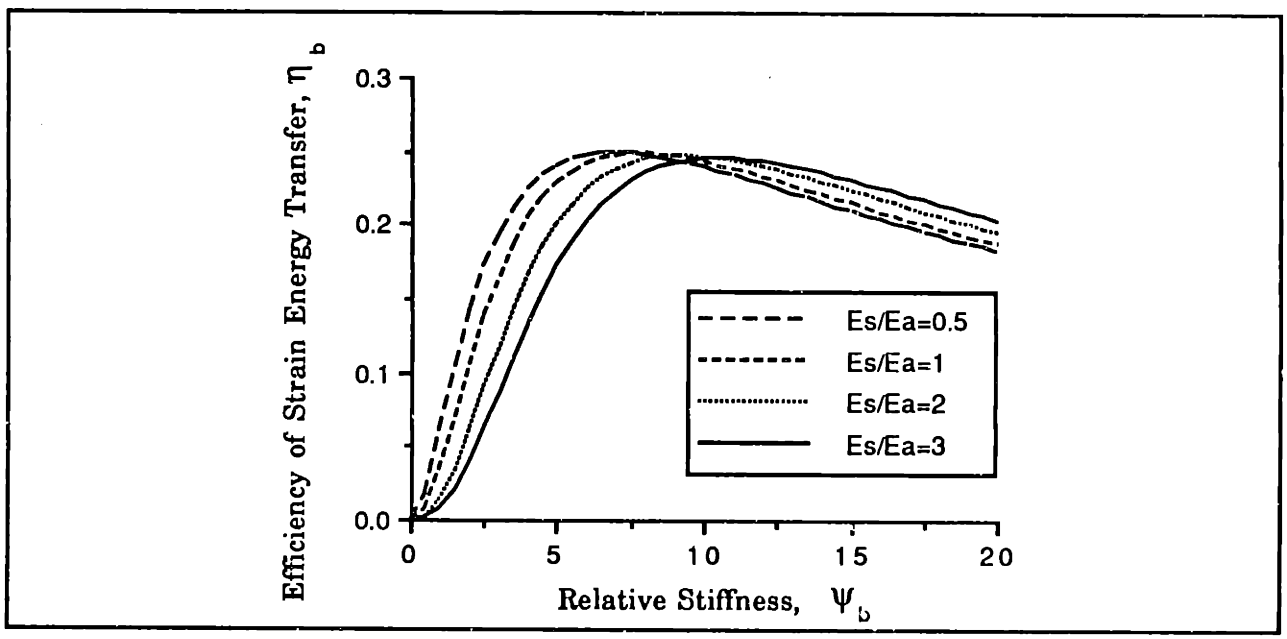

Figure 3.16: Efficiency of Strain Energy Transfer for Bending Induced by Surface-mounted Actuators

efficiency. However, for small ψ_b, where the maximum curvature is induced, the efficiency of strain energy transfer is drastically reduced.

The efficiency of strain energy transfer has been shown to be a means of determining the overall effectiveness of an actuator-structure combination. The analytical formulations provide clear information on both the configuration of maximum energy transfer and the change in effectiveness for different geometries and stiffnesses. In vibration control problems, where total energy is minimized, the effectiveness of strain energy transfer may be a useful guideline for setting the configuration.

Comparison of Embedded and Surface-Bonded Curvatures

In some applications, such as shape control, it may be desirable to induce the largest possible displacements, regardless of energy efficiency. Thus, instead of maximizing strain energy, the strain or displacement is maximized. As an example of the use of a displacement-based comparison, the relative efficiency of embedding and surface bonding actuators will be determined. This comparison will provide guidelines for when the actuators should be embedded and when it is desirable to mount them on the surface of the structure if, in a shape control problem for example, the maximum curvature is desired.

The comparison is specialized to rectangular cross-section beams with a uniform modulus and a pair of actuators an equal distance from the neutral axis. For surface-mounted actuators the induced curvature from Eqs. 3.47 is

$$\kappa = -\frac{6\left(1+\frac{1}{T}\right)\Lambda\left(\frac{2}{t_s}\right)}{(6+\psi_b)+\frac{12}{T}+\frac{8}{T^2}} \tag{3.75}$$

and for embedded actuators the curvature from Eq. 3.39 is

$$\kappa = -\frac{2(EA)_a\left(d+\frac{t_a}{2}\right)\Lambda}{E_s\left(\frac{b_s t_s^3}{12}-2I_a\right)+2E_a I_a} \tag{3.76}$$

where I_a is given by Eq. 3.38. The depth of the embedded actuators is measured with the distance h as shown in Fig. 3.4. Thus,

$$h = \frac{t_s}{2} - d - t_a \tag{3.77}$$

and as a fraction of the total structure thickness

$$H = \frac{h}{t_s} = \frac{1}{2} - \frac{d}{t_s} - \frac{1}{T} \tag{3.78}$$

When the expression for curvature in Eq. 3.76 is written with H, T, and t_s as variables, for $H \geq 0$ it becomes

$$\kappa = -\frac{t_s (EA)_a \left(1 - \frac{1}{T} - 2H\right) \Lambda}{E_s \left(\frac{b_s t_s^3}{12} - 2I_a\right) + 2E_a I_a} \tag{3.79}$$

where I_a is now

$$I_a = A_a \left(\frac{t_s^2}{4} - t_s h + h^2 + h t_a + \frac{t_a^2}{3}\right) \tag{3.80}$$

If the further assumption that the structure and actuators have identical moduli and widths is made, the curvature is

$$\kappa = -\frac{6}{T}\left(1 - \frac{1}{T} - 2H\right)\Lambda\left(\frac{2}{t_s}\right) \tag{3.81}$$

Under similar assumptions, the curvature for the surface-mounted case is Eq. 3.75 with

$$\psi_b = \frac{E_s}{E_a} T \tag{3.82}$$

For a given depth of embedding, H, the curvatures induced by embedded actuators (Eq. 3.81) can be normalized by the curvature induced by surface-bonded actuators (Eq. 3.75) to show the merits of embedding. Such a result is shown in Fig. 3.17.

The curves do not begin at T=0. Physically, H can change from 0, an actuator flush with the surface, to $\frac{1}{2} - \frac{1}{T}$, in which case the actuators are touching each other on the neutral axis. The minimum thickness ratio for embedded actuators is T=2 for H=0, T=2.5 for H=.1, etc.

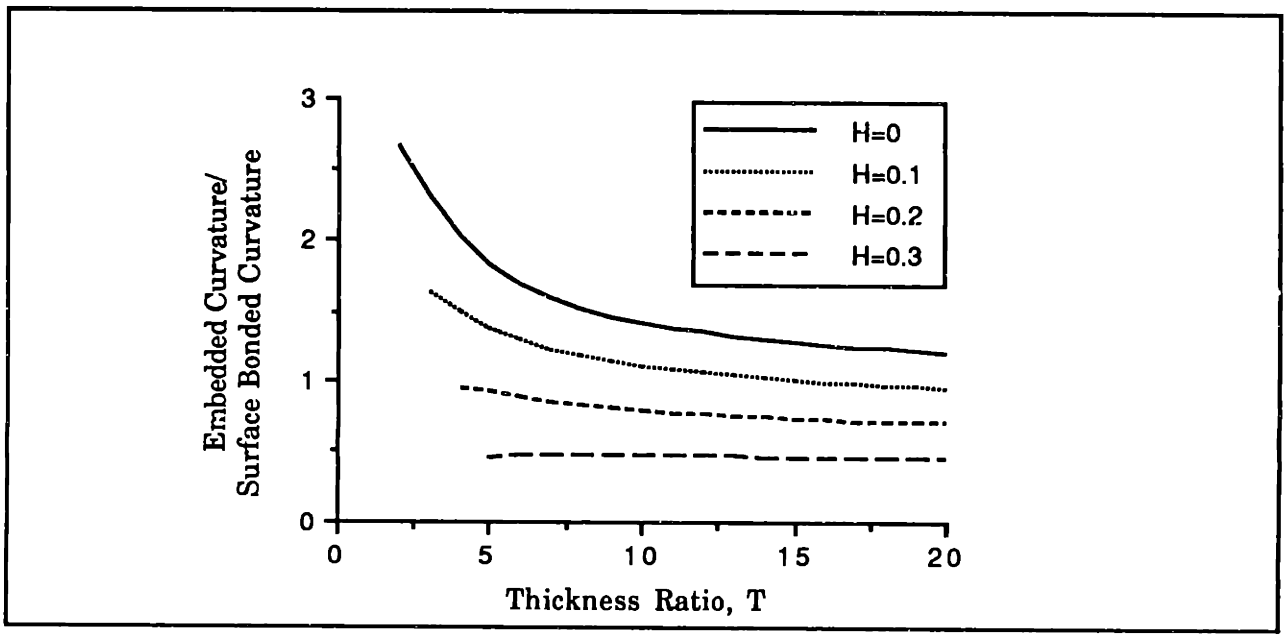

Figure 3.17: Comparison of Induced Curvature for Embedded and Surface-mounted Actuation

Several points are apparent from the figure. As the actuators are embedded deeper in the structure they produce significantly less curvature. As the thickness ratio increases, the curvature from all embedded actuator configurations declines with respect to the surface-bonded curvature. Also, a shallow embedding of less than H=.1 will yield more curvature than surface-mounted actuators for moderate values of T. This implies that more bending strain is induced by an actuator embedded just below the surface than one on the surface. The physical explanation for this effect is that when actuators are moved away from the neutral axis, the bending stiffness increases with the square of the distance and the actuation moment directly with the distance. In addition, when the material cutout is filled, additional stiffness is added.

It has been shown, by comparison of induced curvatures, that embedded actuators may be preferable to surface-mounted ones. In addition, it was shown that, based on a criterion of maximum strain energy transfer, the relative stiffnesses and moduli may be chosen to yield efficient operation. The choice of evaluation depends on the problem of concern. It is clear that for the case of

induced extension, the maximum strain or displacement is induced for a vanishingly thin structure, regardless of the relative moduli of structure and actuator, yet very little energy is transferred. These criteria do however, provide two means of evaluation. In addition, from the previous sections, it is apparent that the effects of the finite bond layer and actuator and structure shear act to reduce both induced displacements and strain energy.

The analytical results found in the chapter to this point will be applied to experimental results in the following section.

3.6 EXPERIMENTS AND RESULTS

A series of tests was conducted with piezoceramic actuators in order to verify the accuracy of the surface-mounted bending models of induced strain actuation. In addition it was expected that observation of the shear lag between the actuator surface and structure surface would be possible. It was not the purpose of these experiments to use the piezoceramics in an active vibration or shape control system.

Bending was induced in two beam test specimens. Because induced strain was the means of actuation, the actuators were placed near the root of the test beams, where strain levels were highest. Both beams were statically deformed and driven dynamically in steady state with the piezoceramic actuators, and the strain in the beam and the ceramics was measured. This section includes descriptions of the manufacture of the two test specimens, the testing procedure, and the test results.

Manufacture of Test Specimens

Two aluminum test specimens were constructed. They had thicknesses of 3.21mm and 1.59mm, or thickness ratios of T=12.65 and T=6.25. In all respects except the thickness, the two specimens were identical. Each was constructed from 2024 aluminum 356mm in length (457mm including the portion of the beam which was clamped) and 51 mm wide.

The piezoceramics used were G-1195 lead zirconate titanate (PZT) with dimensions 63.5mm x 25.4mm x .254mm (2.5in. x 1.0in. x 0.01in.). All ceramics were tested prior to bonding to the beam to insure uniformity in actuation strain output for a commanded field. Tests to determine actuation strain were

conducted in the manner outlined in the previous chapter. The free piezoelectric strain was measured for application of a static field and for a field with frequency 10Hz.

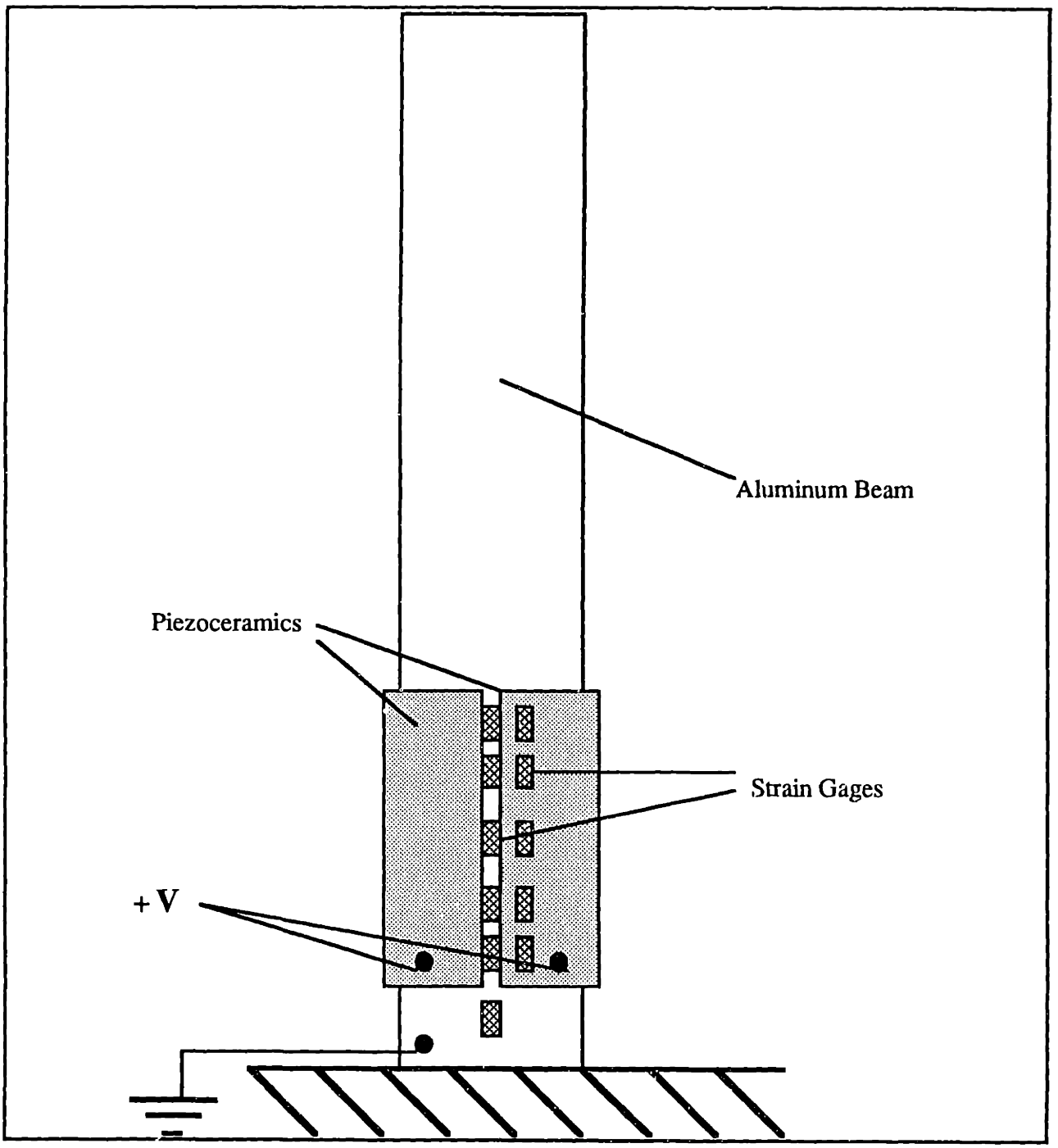

Figure 3.18: Beam Test Specimen

The complete instrumented specimen pictured in Fig. 3.18 illustrates the location of the ceramics. They were bonded 25.4mm (1 inch) from the base of the beam to form two actuator pairs. Amicon, a 24-hour room temperature curing

epoxy manufactured by Emerson Cuming, was used to bond the actuators to the beam surface. First, two ceramics were bonded to one face, then two others were bonded to the opposite face in a separate cure. In order to allow for measure-

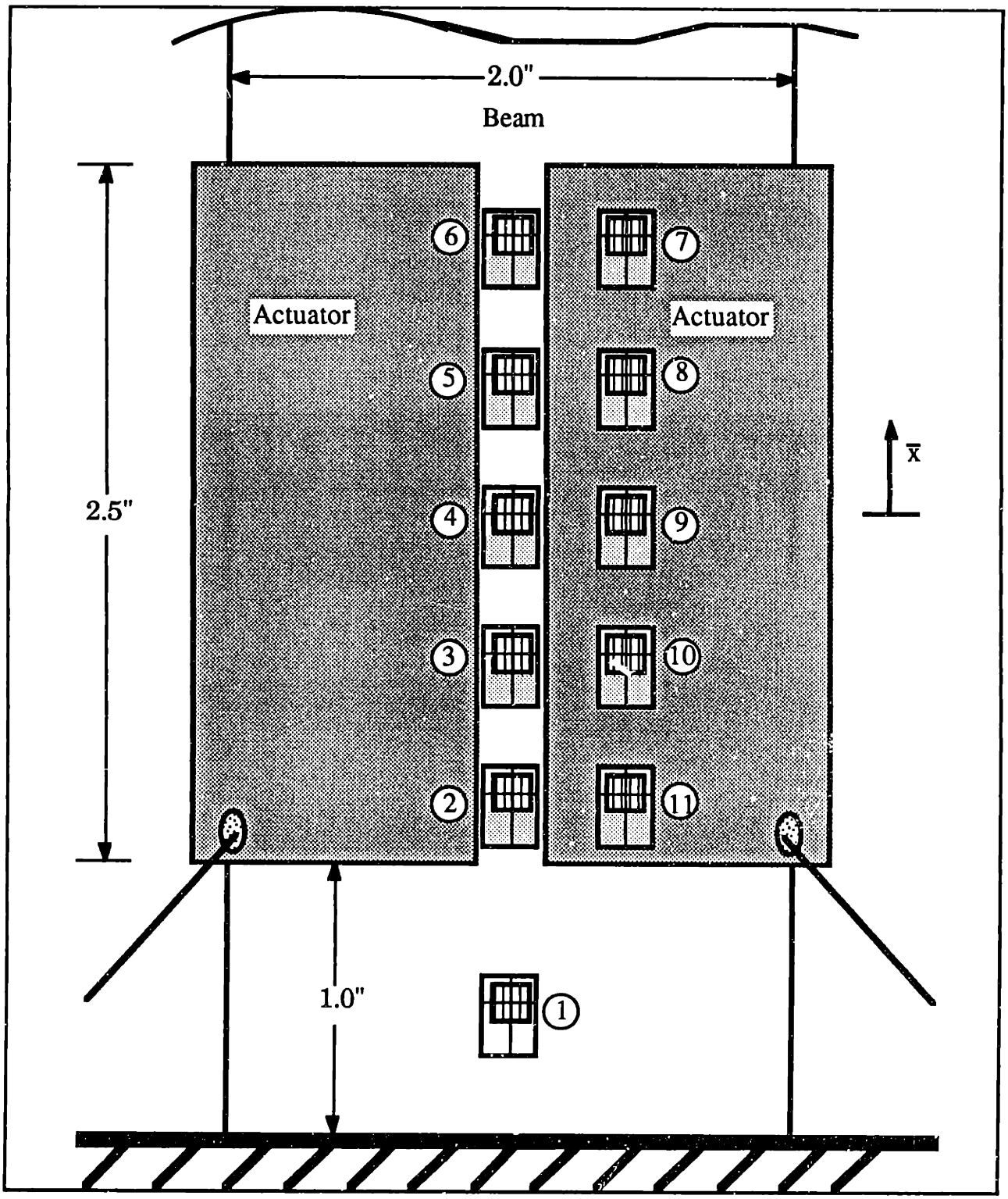

Figure 3.19: Strain Gage Locations on Beam Test Specimens

ment of the strain on the beam surface, the actuators were placed so that a gap of 6mm remained on the surface of the structure between them. The ceramics overhang the edge of the beam by 3mm, allowing for easy electrical connection to both the upper and lower faces of all four ceramics. Eleven strain gages were mounted on the structure and actuator in order to measure the strain on both the beam and ceramic surface (Fig. 3.19). Each gage had dimensions of 4.8mm by 7.2mm with an active gage length of 1.57mm. The lowermost gage was used to measure overall beam motion. The other 10 gages measured the relative surface strains in the beam and ceramics.

Test Procedure

Both static and dynamic tests were performed on each of the two beams. In all cases, the actuators were oriented, and the appropriate field applied, to induce bending of the beam. For all tests, the specimens were clamped vertically to a .5m x.5m x.15m steel test stand. The entire test stand sat on a 15mm thick rubber sheet for further dynamic isolation of the test article. An aluminum clamp, consisting of two 100mm x 200mm x 50mm blocks bolted to the test stand, held the specimens. The procedure for each type of test will be described below.

In the static tests, a DC voltage supply provided an identical electric field to each of the four actuators. Voltages of 50V and 100V were applied, corresponding to field levels of 196.9V/mm and 393.7V/mm. After a wait of several minutes for the effects of creep to abate (Section 2.2), strain measurements were made. A switching box and a digital voltmeter were used to read the 11 strains.

In the dynamic tests, a Wavetek signal generator supplied a sinusoidal input to a high-impedance amplifier which was used to drive the piezoceramics. The amplifier was configured to represent a voltage source. Tests were conducted at frequencies from 0.1Hz to just above the first cantilevered-free frequency of the beams. The amplitudes of the input fields were 113V/mm and 226V/mm for the T=12.65 beam and 113V/mm for the T=6.25 beam. At each frequency, the strains were recorded on a Nicolet 2090 digital oscilloscope. The data were later processed to determine the amplitudes of the strains.

The major objective of the tests was to provide comparative strain data for evaluation of the models. In addition, the total response of the beam was calculated to verify the basic static and dynamic models.

In order to predict the dynamic response of the beam due to the induced strain, damping measurements were made. Immediately following the steady state tests, the beam was excited at resonance at an amplitude slightly greater than the highest achieved in the test. The input voltage was then cut off and the subsequent ringdown, as measured by the strain of gage 1 (Fig. 3.19) was recorded. The ringdown data were used to estimate damping corresponding to the amplitude of motion of the beam achieved in the tests. Aerodynamic damping and friction from the clamp caused increased damping at higher amplitudes. In predicting the response, the damping level for the actual amplitude was used.

Results

The test results generally support the Bernoulli-Euler bending model. That is, the strain through the beam and the surface-mounted actuators appeared to have a linear variation with z. The basic strain results confirming the model will be presented below. The effect of shear lag as well as the effect of piezoceramic creep at low frequencies will be illustrated. Finally, the analytical predictions of induced strain and overall beam motion will be compared to the data.

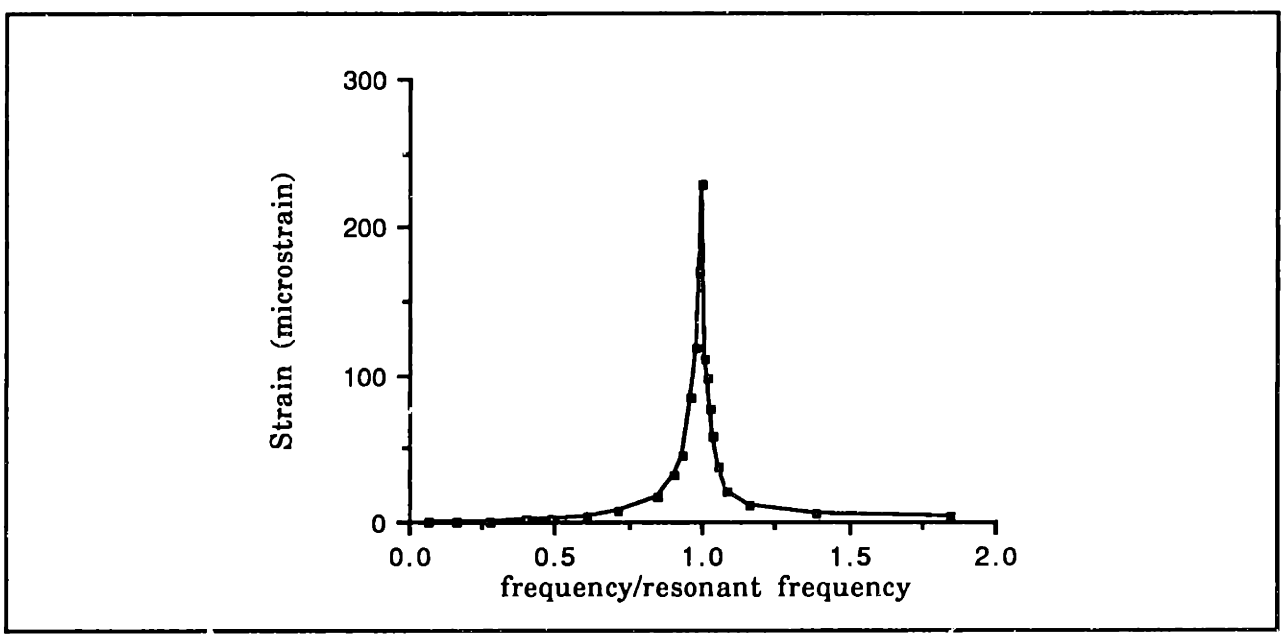

Figure 3.20: Typical Strain vs. Frequency Data (Gage 1)

The typical strain data taken for the sine sweep tests is shown in Fig. 3.20. The strain amplitude at the first bending frequency is obviously much larger than at low frequencies or in static tests. The first bending frequencies of the two specimens were 21.7Hz and 11.2Hz.

For perfectly-bonded actuators the Bernoulli-Euler bending model predicts the ratio of the strain (Fig. 3.19) on the surface of the actuator (gages 11,10,9,8,7) to that on the surface of the structure (gages 2,3,4,5,6) to be

$$\frac{\varepsilon_a^{surf}}{\varepsilon_s^{surf}} = \frac{\frac{T}{2}+1}{\frac{T}{2}} = 1 + \frac{2}{T} \tag{3.83}$$

which for the two test beams with T=12.65 and T=6.25 is

$$\frac{\varepsilon_a^{surf}}{\varepsilon_s^{surf}} = 1.158 \quad and \quad \frac{\varepsilon_a^{surf}}{\varepsilon_s^{surf}} = 1.32 \tag{3.84}$$

independent of frequency. The uniform strain model predicts the ratio of the two strains to be 1.

In Fig. 3.21 the strain ratios for the five strain gage pairs are shown as a function of frequency. The predicted strain ratios for the perfect bond uniform strain and Bernoulli-Euler models are shown. For both beams, the Bernoulli-Euler prediction corresponds more closely to the data. The error of the uniform strain model is more significant for the thinner beam (b) as would be expected (Section 3.4). The Bernoulli-Euler model better represents the real state of strain because it allows bending in the actuators.

The agreement of the Bernoulli-Euler model with the data is not exact. The data are grouped in a band around the prediction, and show a slight dependence on frequency. As expected, the strain ratios for all five strain gage pairs converge (to values within 5% of each other) at the first resonant frequencies for each of the beams. For the thicker beam (a) the ratios are centered about the Bernoulli-Euler prediction. For the thinner beam, they are as much as 5.5% below the prediction.

For frequencies above resonance, the ratios deviate from the narrow band of values. This is due to the influence of the second beam bending mode, and the presence of strain nodes. The low strains are difficult to measure accurately.

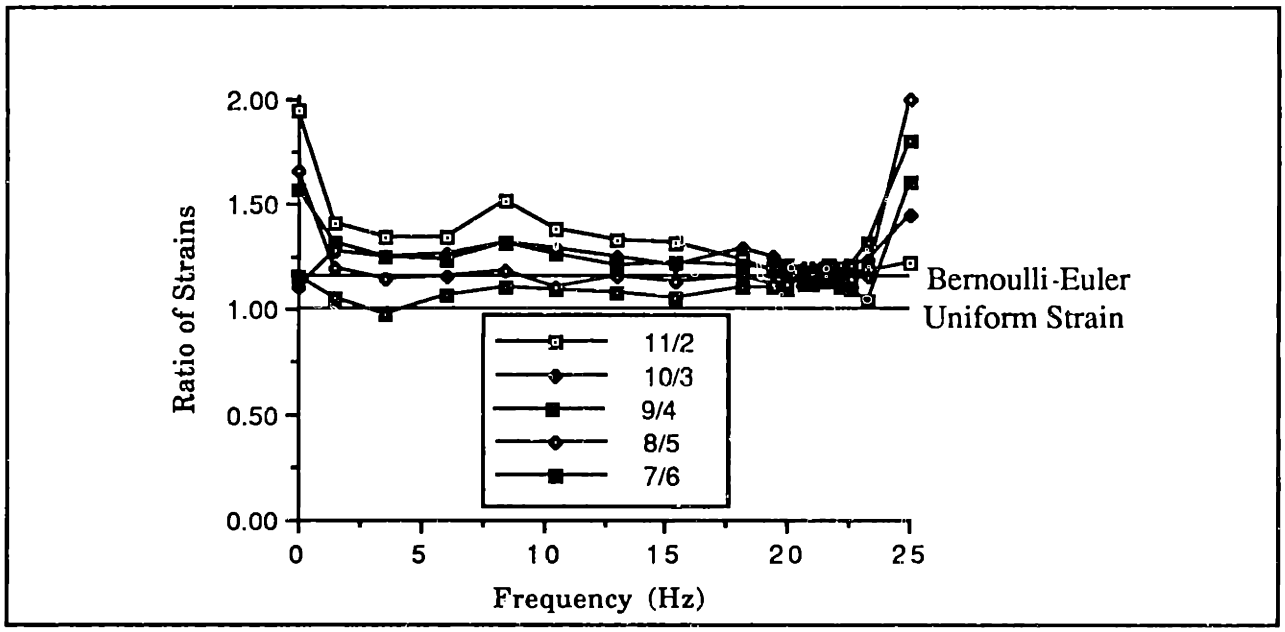

a) T=12.65

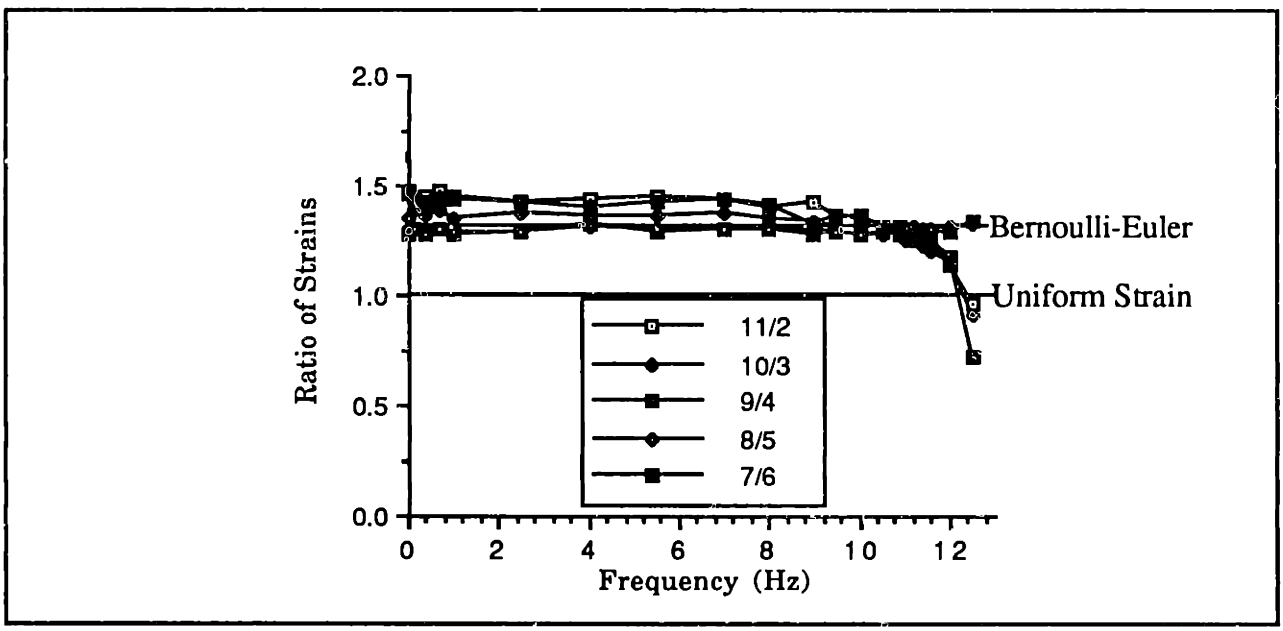

a) T=6.25

Figure 3.21: Ratios of Strain on Surface of Actuator and Surface of Structure vs. Frequency

At low frequencies above DC where dynamic amplification is still small (*i.e.* 3-15 Hz and 2-8 Hz for the respective specimens), the five ratios show a large variation. For T=12.65 (a) at 10.5 Hz, the ratios vary from 1.07 to 1.33 and for

T=6.25 (b) at 5.5 Hz they vary from 1.29 to 1.45. In both cases, the lowest ratio is found for the gages (9/4) in the center (Fig. 3.19). For all frequencies, this ratio remains below that predicted, indicating that the strain distribution through-the-thickness is not precisely linear. However, the linear consistent strain assumption is still better than the uniform strain one.

The strain ratios measured near the ends of the actuators (11/2, 7/6) are

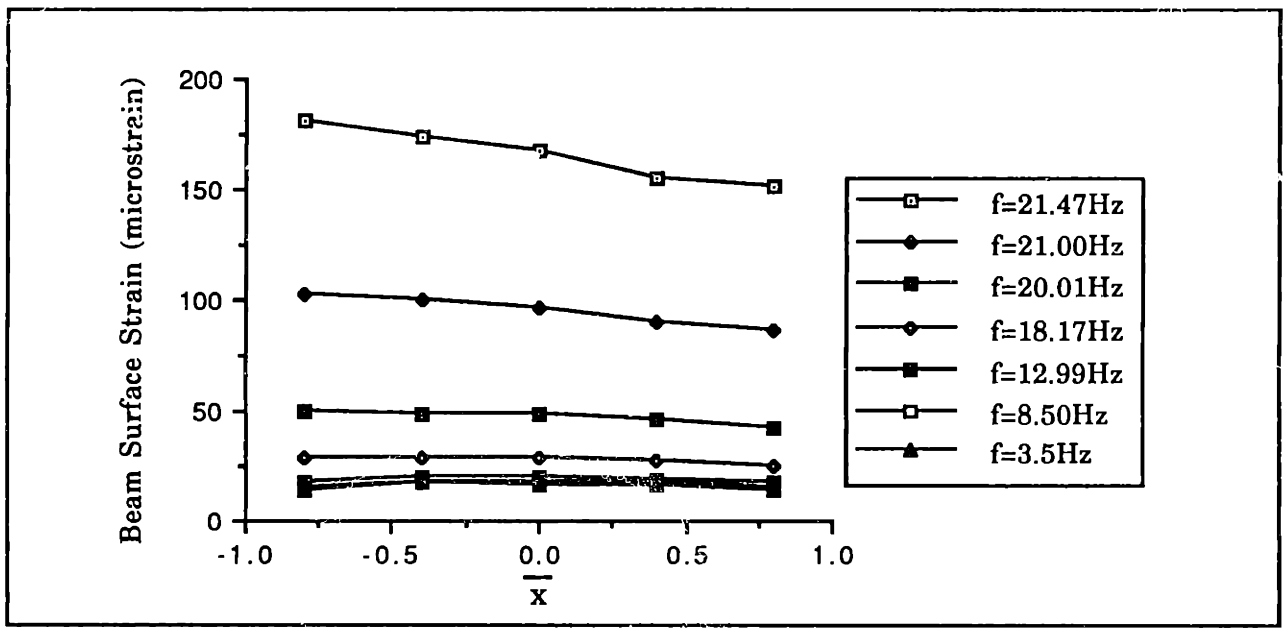

a) T=12.65

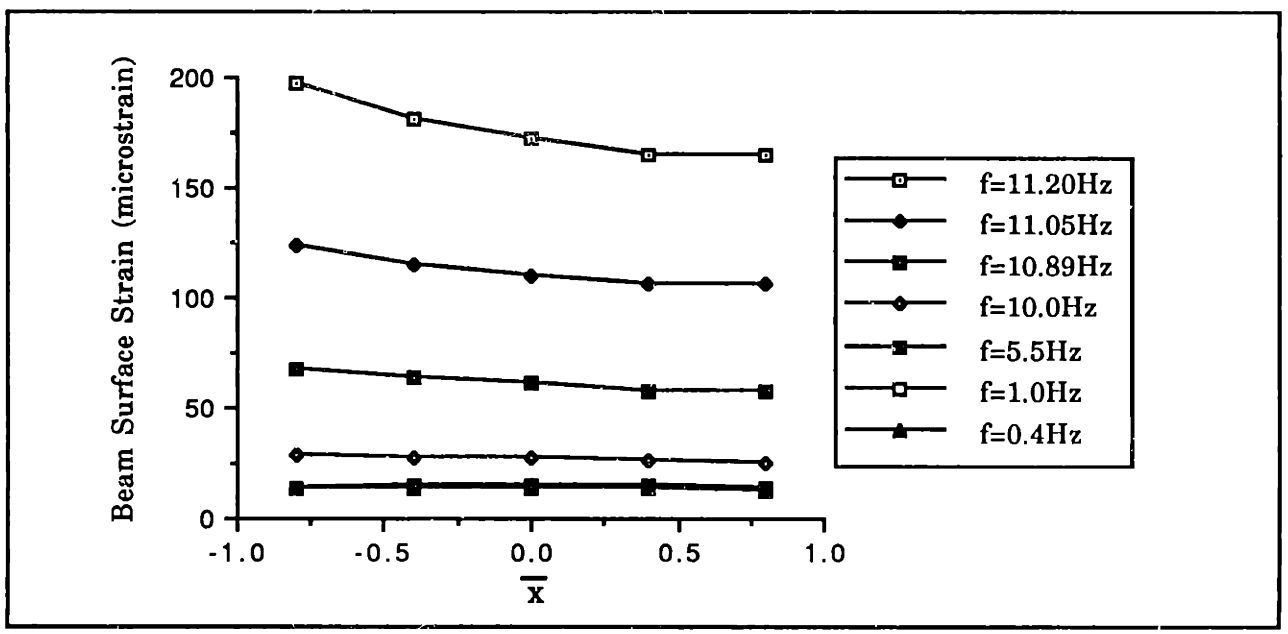

b) T=6.25

Fig. 3.22: Strains Measured at Beam Surface for Frequencies Below First Bending Resonance

generally between 10 and 20% higher than the predicted ratio. This is due in part to the lack of a constraint on the free edge of the actuators. In addition, a shear lag in the adhesive bonding layer or actuator increases the ratios. At the resonant frequencies, the ratios at the outer gages drop to match the others as the global first mode strain dominates.

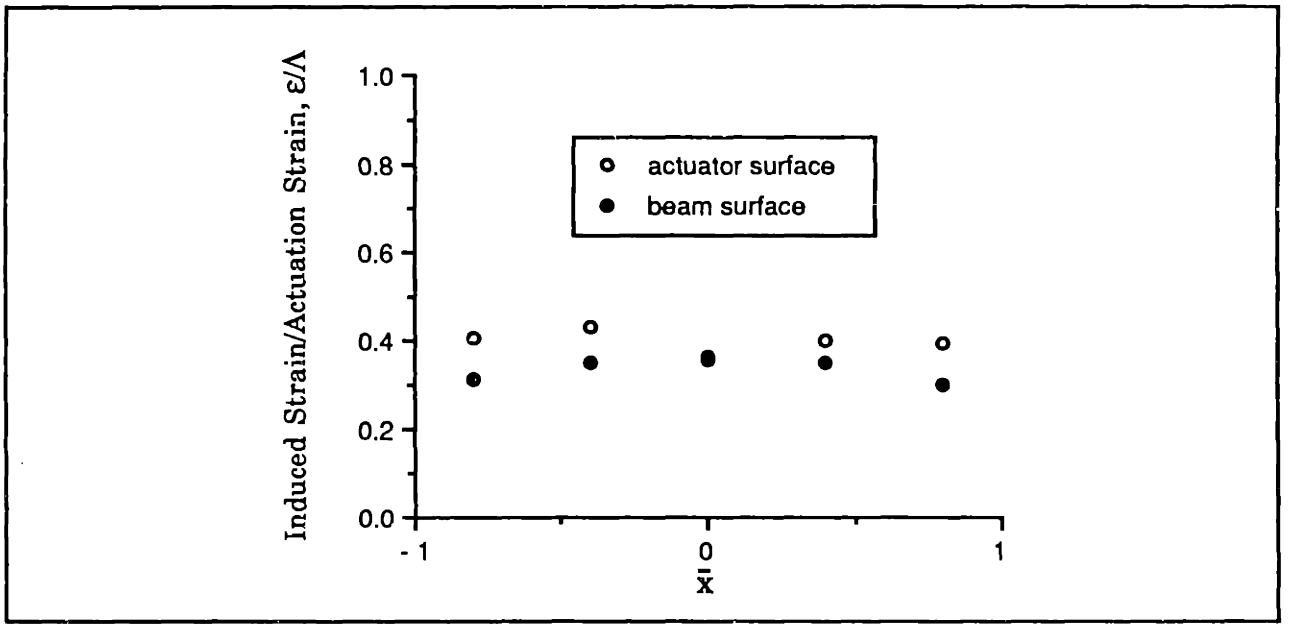

a) T=12.65 (3.5 Hz)

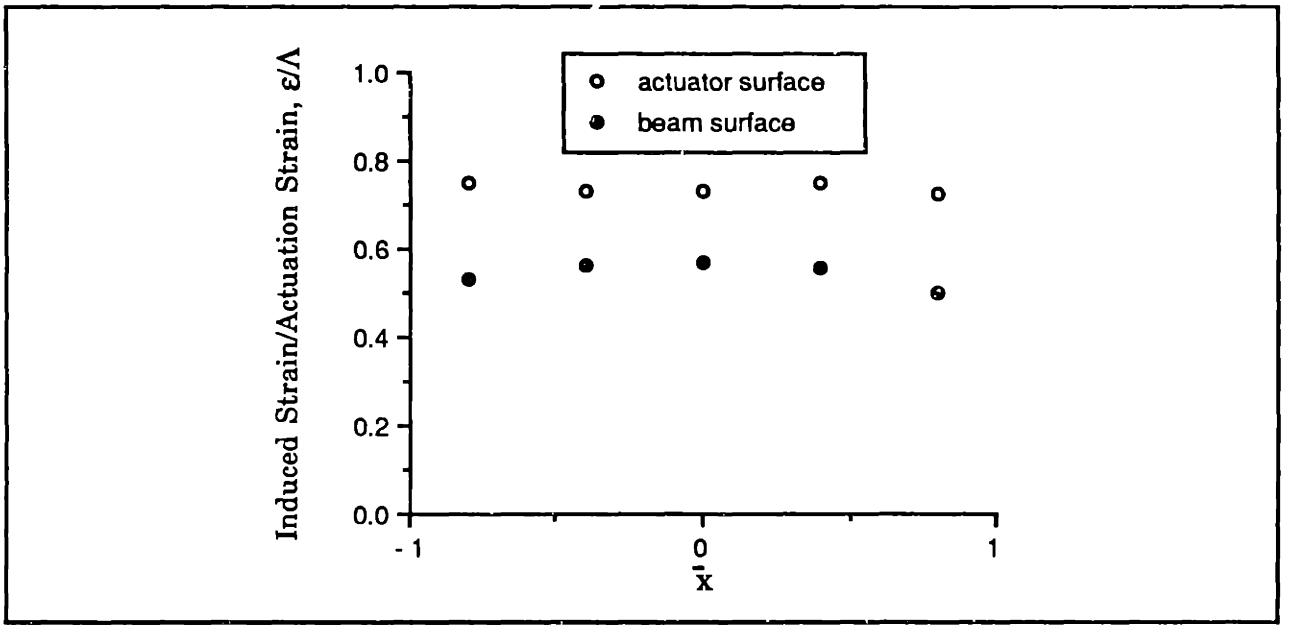

b) T=6.25 (1 Hz)

Figure 3.23: Low Frequency Induced Strains at Actuator and Structure Surface

Another way to view at the strains is to look directly at the measured strains in the beam. Figure 3.22 shows the strain over the length of the actuators for several frequencies up to resonance. Note that at low frequency the total strains are small. They are highest in the middle ($\bar{x}$ =0) and drop off symmetrically at both ends, where lags exert local influence. At higher frequencies, overall strain levels are greater. In addition, the strains decrease from $\bar{x}$ =-0.8 to $\bar{x}$ =0.8. These measuring points correspond to 9% and 23% of the distance from the root along the beam, and thus illustrate the imposition of the beam first bending mode. The most useful data for examining induced strain is found at the low frequencies (Fig. 3.23) where nearly all the strain is due to induced strain and not dynamic/inertia effects.

The dropoff in strain may be due to the physical arrangement. Because the beams were not entirely covered by the two actuators, it is possible that the entire cross section does not bend as one unit - there is a lag in strain across the center section, which is not directly covered by the actuators (Fig. 3.19). Although the configuration may be a possible explanation, it is believed to be of secondary significance.

Even at low frequencies, there is some dynamic amplification present. For example, the T=6.25 actuator surface and beam surface strains based on the Bernoulli-Euler model are predicted to be .61Λ and .46Λ, but they are actually about 20% higher (Fig. 3.23). Even within the limited resolution of the five gages mounted on the beam, it is apparent that the strain drops off near the edges of the actuators. With no dominant dynamic effects, the induced strain distribution appears to be symmetric about the center of the actuators. The reduction in strain near the edges is believed to be due in part to the shear lag in the transfer of strain across the bonding layer. It is not believed to be due to the effects of actuator shear. In the finite element model it was shown that the shear lag of the actuator itself occurs only over a few actuator thicknesses near the edge of the actuator. The gages at $\bar{x}$ = $\pm$0.8, located 25 actuator thicknesses from the edges of the actuator, were not able to measure that effect.

Fig. 3.24 shows the distribution of strain in the actuators and structure for two static tests. In plots of the static strain data, the strains show no dynamic amplification. However, the same general shape of the curves is apparent. The Bernoulli-Euler predictions shown will be discussed in the next subsection. The

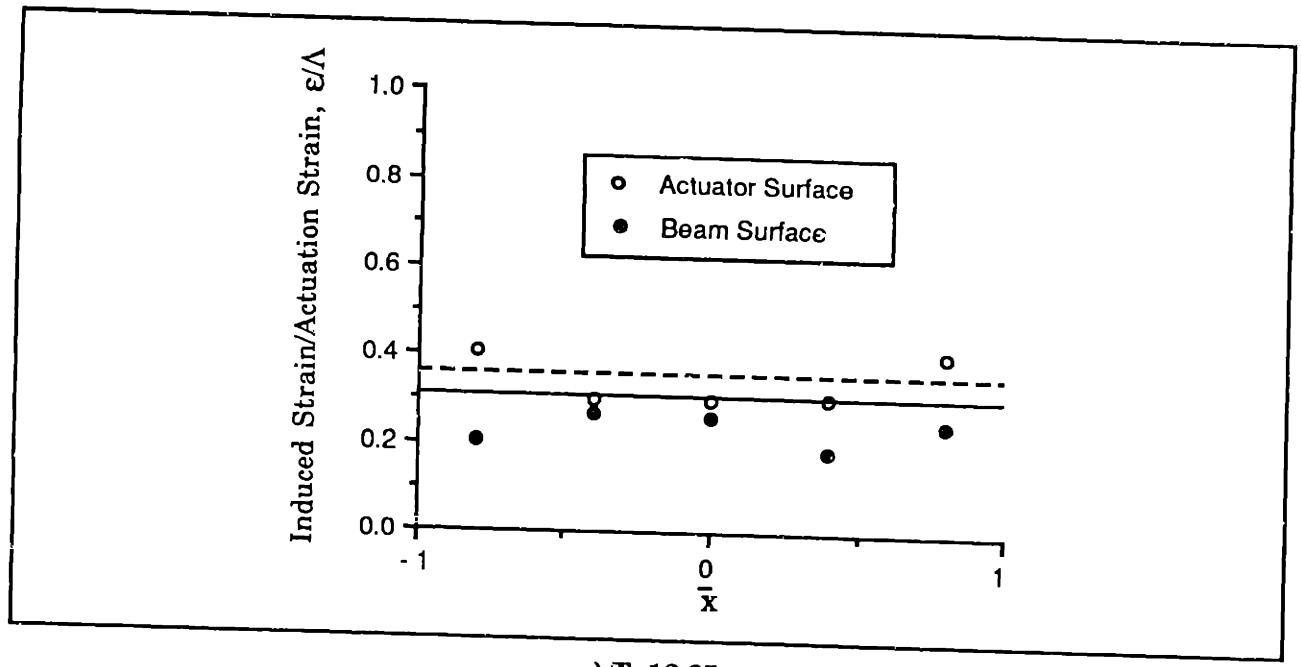

a) T=12.65

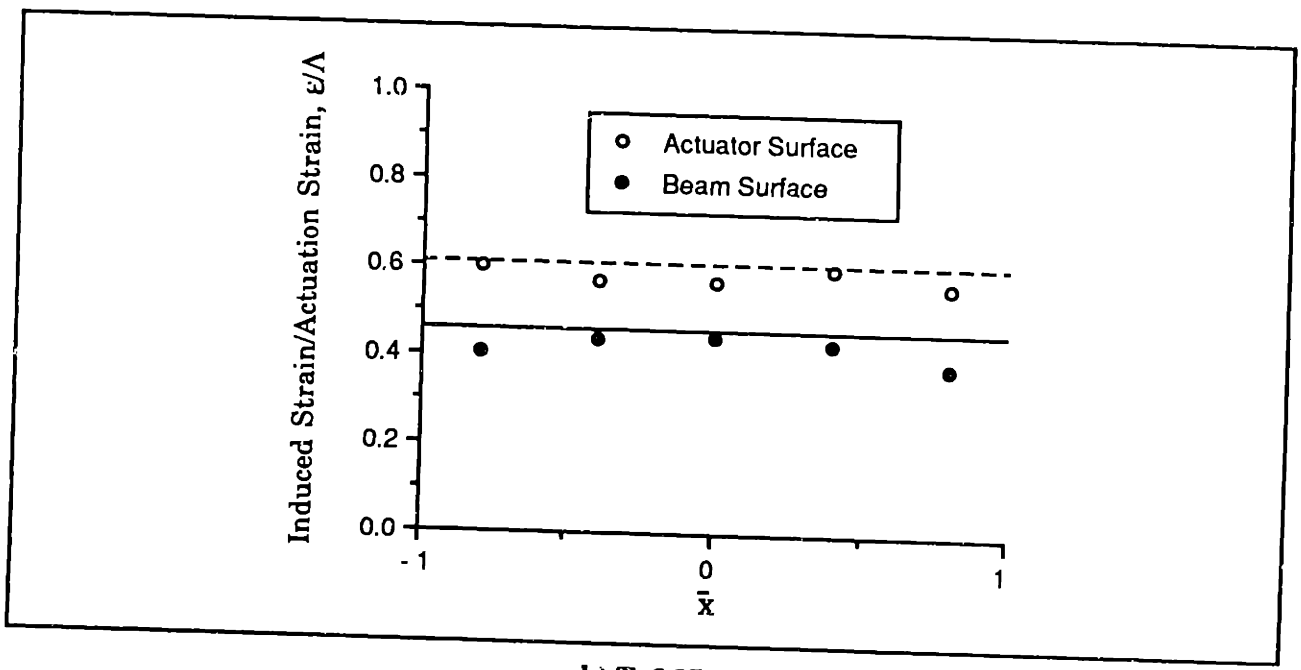

b) T=6.25

Figure 3.24: Static Induced Strains at Actuator and Structure Surface

static tests highlight the effect of the bonding layer. There is a clear drop in strain near the edges ($\bar{x} = \pm 0.8$) for both beams. The bond for the T=12.65 beam is worse as evidenced by the dropoff of strain in the structure near the edges. In addition, in static tests there is piezoelectric creep in the actuators. The piezoelectric creep was evident during measurement and the data shown were taken after several minutes at one DC field.

Hysteresis was also in evidence. In the thicker structure, with a worse bond, the structure did not exhibit hysteresis at nearly the same level as the actuators. However, for the thinner beam with a better bond, the hysteresis was present to nearly the same extent in both the beam and the actuator. The hysteresis loop aspect ratios for the beam strains were 6% and 9.5% for the two field levels. If the net strain in the actuators, which average 30.2μS and 67.8μS over the length and width of the actuator, are considered, a prediction of the aspect ratio may be made from Fig. 2.10. For those strain levels, aspect ratios of 9% and 14% are expected in free actuators. Thus, when the actuators are part of a structure the hysteresis is still present, but to a lesser extent.

Strain Prediction

In order to confirm the basic accuracy of the model of actuation, it was considered desirable to attempt to predict the absolute beam strains for both the static and dynamic tests. These predictions incorporate the nonlinear strain-field relation of the actuators discussed in Section 2.2, but do not include the effects of adhesive layer shear lag. For the dynamic cases, the experimentally determined damping ratio is also used in the amplitude estimation. The perfect bond Bernoulli-Euler bending model is used for both static and dynamic predictions.

For the static tests, the strain of the beam in the center of the actuators as measured by gage 4 was predicted. This was accomplished as follows. Equation 3.47 from the Bernoulli-Euler model is used to obtain an expression for the surface strain. Thus for the two test beams, with $\bar{E}$=1.111 and T=12.65 and T=6.25, the predicted strains are

$$\varepsilon_s^{surf} = .310\Lambda \quad \text{and} \quad \varepsilon_s^{surf} = .462\,\Lambda \tag{3.85}$$

and with the linear assumption of through-the-thickness strain, the average strains in the actuators are

$$\varepsilon_a^{avg} = .335\,\Lambda \quad \text{and} \quad \varepsilon_a^{avg} = .536\,\Lambda \tag{3.86}$$

A value (the small signal value $\Lambda=d_{31}E_3$ was used as a start point) is assumed for the actuation strain, Λ, and an induced strain can be predicted in the structure. That calculated induced strain is then used to determine a more accurate value for Λ, by selecting the appropriate d^*_{31} based on the level of induced strain from a

d^*_{31}-strain plot (see Fig. 2.7). This yields a better prediction and the process may be repeated until a value of induced strain is converged upon. For the cases here, no more than three iterations were required for convergence. The results of the predictions are shown in Table 3.1.

Table 3.1: Static Induced Strain Predictions and Data (Beam Specimens)

Thickness Ratio	Field (V/mm)	d* 31(pm/V)	Microstrain		Error
			Predicted	Data	
T=12.65	197.9	283	17.3	14.7	+17.7%
	393.7	312	38.1	32.6	+16.9%
	590.6	331	60.7	52.4	+15.8%
T=6.25	197.9	302	27.5	26.8	+2.6%
	393.7	344	62.6	60.1	+4.2%

The predictions for the thinner beam are more accurate, while the predicted strains for the thicker beam are significantly higher than the actual strains. This is believed to be due mainly to the losses from the adhesive layer. In all cases, the values for d^*_{31} shown in the table are considerably larger than the small signal value, d_{31}= 180pm/V.

A Bernoulli-Euler model with a finite bond was also fit to the low frequency data to determine the value of the shear parameter, Γ. For beam strain data at 0.5Hz and 0.1Hz for the T=12.65 and T=6.25 beams respectively, Γ was found to be equal to 12.5 and 9.3.

The prediction of the induced strain at the first bending resonance was accomplished with a dynamic model. Because the motion of the beam was greatly amplified beyond the static strain level, the total strain of the beam, as measured by gage 4, was used to predict the performance. It was assumed, based on the results of the previous chapter, that the mechanically-imposed strain did not affect the correct d^*_{31}. Therefore, the predicted piezoelectrically-induced strain level based on 10Hz free piezoceramic strain data was used to calculate the appropriate d^*_{31}.

The dynamic motion was modeled with a 5-mode Rayleigh-Ritz model. Such a model is similar to the plate models of the next chapter which are formulated in terms of kinetic and potential energy and solved approximately. The modes used were the first five exact cantilevered-free bending mode shapes for a uniform beam as represented by

$$\phi(\tfrac{x}{L}) = \cosh(\lambda_i \tfrac{x}{L}) - \cos(\lambda_i \tfrac{x}{L}) - \mu_i\left(\sinh(\lambda_i \tfrac{x}{L}) - \sin(\lambda_i \tfrac{x}{L})\right) \tag{3.87}$$

where λ_i and μ_i depend on the mode. Values for these coefficients are presented in Appendix E. The modal mass of the beam is

$$M_{ij} = \rho_s A_s l_s \int_{l_s} \phi_i \phi_j dx \tag{3.88}$$

where ρ_s is the density. Because the chosen modes are orthogonal, the 5x5 mass matrix is diagonal. The modal mass of the actuators was found to be less than 1% of the beam modal mass and was ignored. The 5x5 modal stiffness matrix of the beam is

$$K_{ij} = \frac{(EI)_s}{l_s^3} \int_{l_s} \phi_i'' \phi_j'' dx \tag{3.89}$$

Again, because of the selection of modes, the beam stiffness matrix is diagonal. The stiffness of the actuators is

$$KA_{ij} = \frac{2(EI)_a}{l_s^3} \int_{l_a} \phi_i'' \phi_j'' dx \tag{3.90}$$

The exact beam modes are not orthogonal over the length of the actuators. Therefore, the actuator stiffness matrix contains off-diagonal terms. The stiffness contribution of the actuators is 9% and 20% for the first mode for the thin and thick beams. The predicted first bending frequencies for the two beams were 21.5Hz and 11.8Hz, and the corresponding experimentally determined values were 21.7±0.1Hz and 11.2±0.1Hz.

The piezoelectric terms are incorporated in the modal forcing, Q. The modal forcing term is based on the second strain energy term in Eq. 3.32

$$Q = M_{\Lambda} \frac{\partial^2 w}{\partial x^2} \tag{3.91}$$

which can be rewritten

$$Q_j = \frac{(EA)_a (T + 1) t_a}{l_s} \Lambda \int_{l_a} \ddot{\phi_j} dx \tag{3.92}$$

The full width of the actuators was included in both the stiffness and forcing terms.

The equations of motion for the system are

$$(\boldsymbol{K} + \boldsymbol{KA})\boldsymbol{q} + \boldsymbol{M}\ddot{\boldsymbol{q}} = \boldsymbol{Q} \tag{3.93}$$

This matrix equation was solved by diagonalizing the stiffness matrix and obtaining the undamped residuals of the new 2nd, 3rd, 4th, and 5th modes at the first resonant frequency, and adding the damped resonant modal amplitude for the 1st mode

$$q_1 = \frac{1}{2\zeta} \frac{Q_1}{K_{11}} \tag{3.94}$$

where the damping ratio ζ was experimentally determined to be equal to 1.14% for the thicker beam and 0.96% for the thinner one at the amplitudes of concern. Thus, the model was essentially a 1-mode damped Rayleigh-Ritz model with four additional undamped modes added to more accurately capture the actual deflections. The surface strain at the location of gage 4 (x/L=.1607) was computed as

$$\varepsilon_s^{surf} = \left(\frac{t_s}{2}\right) q_i \phi_i'' \Big|_{x=.1607} \tag{3.95}$$

where the contributions of the five modes were summed to obtain the total strain. The predictions and data are shown in Table 3.2.

It was expected that the models would be overly stiff and would underestimate the actual strains. This is the case for the thinner beam (T=6.25). The prediction for the thicker beam (T=12.65) is higher because of greater losses

in the bond layer. In addition, because the actuators contribute a smaller fraction of the total stiffness, the chosen modes more easily represent the actual mode shape. The difference between the errors in the two beams is not as great as in the static case, because the piezoelectrically-induced strains are lower, adhesive bond layer creep is less prevalent, and some of the dynamic effect of the bonding layer loss is accounted for in the higher damping ratio of the thicker beam.

Table 3.2: First Mode Induced Strain Predictions and Data (Beam Specimens)

Thickness Ratio	Field (V/mm)	d* 31(pm/V)	Microstrain		Error
			Predicted	Data	
T=12.65	226	221	167.3	167.1	+0.1%
T=6.25	113	216	158.3	172.6	-8.3%

Experimental results for static and dynamic tests on two beam specimens have been presented. Evidence of the real piezoceramic properties discussed in Chapter 2 - nonconstant d_{31}, hysteresis, and creep - was found. The shear lag due to the presence of an adhesive bonding layer was evident, particularly in the T=12.65 beam. A Bernoulli-Euler model with a perfect bond assumption was accurate at predicting induced strain levels under the center of the actuator for both test specimens. The Bernoulli-Euler model with a finite bond layer included was used to fit data illustrating the shear lag due to the finite bond.

3.7 SUMMARY

In this chapter, three separate models of induced stain actuation for one-dimensional structures were developed. Results for the uniform strain model, adapted from Crawley and de Luis (1987), were presented. The model was found to be accurate in description of induced stretching, but inaccurate in description of induced bending, particularly for thin structures. Results for the Bernoulli-Euler model for general cross-section beams with embedded or surface-mounted actuators were derived. The Bernoulli-Euler model results for induced stretching were identical to those from the corresponding uniform strain model. The Bernoulli-Euler bending model, which included the full bending stiffness of the actuators, was judged to predict strains correctly. The results from an ADINA finite element model correlated well with the Bernoulli-Euler results for

prediction of induced strain, and highlighted the presence of material shear in the actuators and structure. This effect was judged to be significant only for low aspect ratio (length/thickness) actuators and thick beams, where the influence of shear on net induced displacement was greatest. The influence of a finite bonding layer between actuators and structure was characterized by a shear parameter, Γ. The bonding layer affected induced strain along the actuator length, net displacement, and energy transfer.

The optimal geometry for surface-mounted actuators for maximum strain energy transfer was derived. The relative efficiency of embedded and surface-mounted actuators was illustrated for inducing maximum curvature in a structure. It was shown that actuators embedded slightly below the surface of a structure are more efficient than surface-bonded actuators. Experimental results confirmed the accuracy of the Bernoulli-Euler bending model. Evidence of a finite bonding layer was presented, along with the real piezoelectric properties of the previous chapter. The static and dynamic strain amplitudes were predicted.

In the next chapter, the one-dimensional models will be extended to two-dimensional plate structures and compared with experimental results.

CHAPTER FOUR: TWO-DIMENSIONAL INDUCED STRAIN ACTUATION

4.0 INTRODUCTION

Induced strain actuation may be utilized in both one-dimensional beam-like structures and two-dimensional plate structures. In thin plate-like structures, relatively small inplane induced strains often correspond to larger out-of-plane deformations. In anisotropic plates, inplane extensional strains can induce stretching, shearing, bending, and twisting. Thus, induced strain actuators can be useful in a variety of shape and vibration control applications.

Both static and dynamic analysis of plates are well established disciplines (Timoshenko and Woinowsky-Krieger, 1959, and Leissa, 1969). The analysis of anisotropic (composite) plates through classical laminated plate theory is also well understood (Jones, 1975). Further, in the study of laminated plates, the inclusion of thermal or moisture effects is straightforward. These analytical methods necessary for representation of induced strain actuation of plates will be used to formulate the two-dimensional induced strain problem.

In this chapter, the objective is to extend the one-dimensional models of the previous chapter to the more general two-dimensional thin plate case. A more complete study, specifically devoted to both isotropic and anisotropic plates, was undertaken separately from the current study (Lazarus, 1989). In a third study (de Luis, 1989) focussing on strain-based control concepts, a plate-like graphite/epoxy structure containing 32 embedded piezoceramic actuators was constructed.

This chapter is organized in the same fashion as the previous one. In Section 4.1, the uniform strain model of Section 3.1 is extended to plates. In Section 4.2, a model of induced strain actuation is derived using classical laminated plate theory. The Bernoulli-Euler model of Section 3.2 is shown to be a one-dimensional specialized case of this model. In Section 4.3, the two models are briefly compared. In Section 4.4, the energy formulation of the plate problem is presented. It is shown in Section 4.5 that the energy formulation may be solved exactly for a limited number of static cases. The approximate approaches

necessary for most static and all dynamic problems are described. In Section 4.6, experiments involving aluminum plates are described and results presented. Finally, in Section 4.7, induced strain actuation of plate structures is summarized.

4.1 UNIFORM STRAIN MODEL

In this section, analytical models based on an assumed uniform extensional strain in the actuators will be derived for plates of arbitrary cross-section. The uniform strain plate model is based on the uniform strain beam model summarized in Section 3.1, and formulated by Crawley and de Luis (1987). The assumed strain distribution of Fig. 3.2 can be applied to the plate problem to model the normal strains in the x-z or y-z cross-sections. The plate geometry for surface mounted actuators is illustrated in Fig. 4.1.

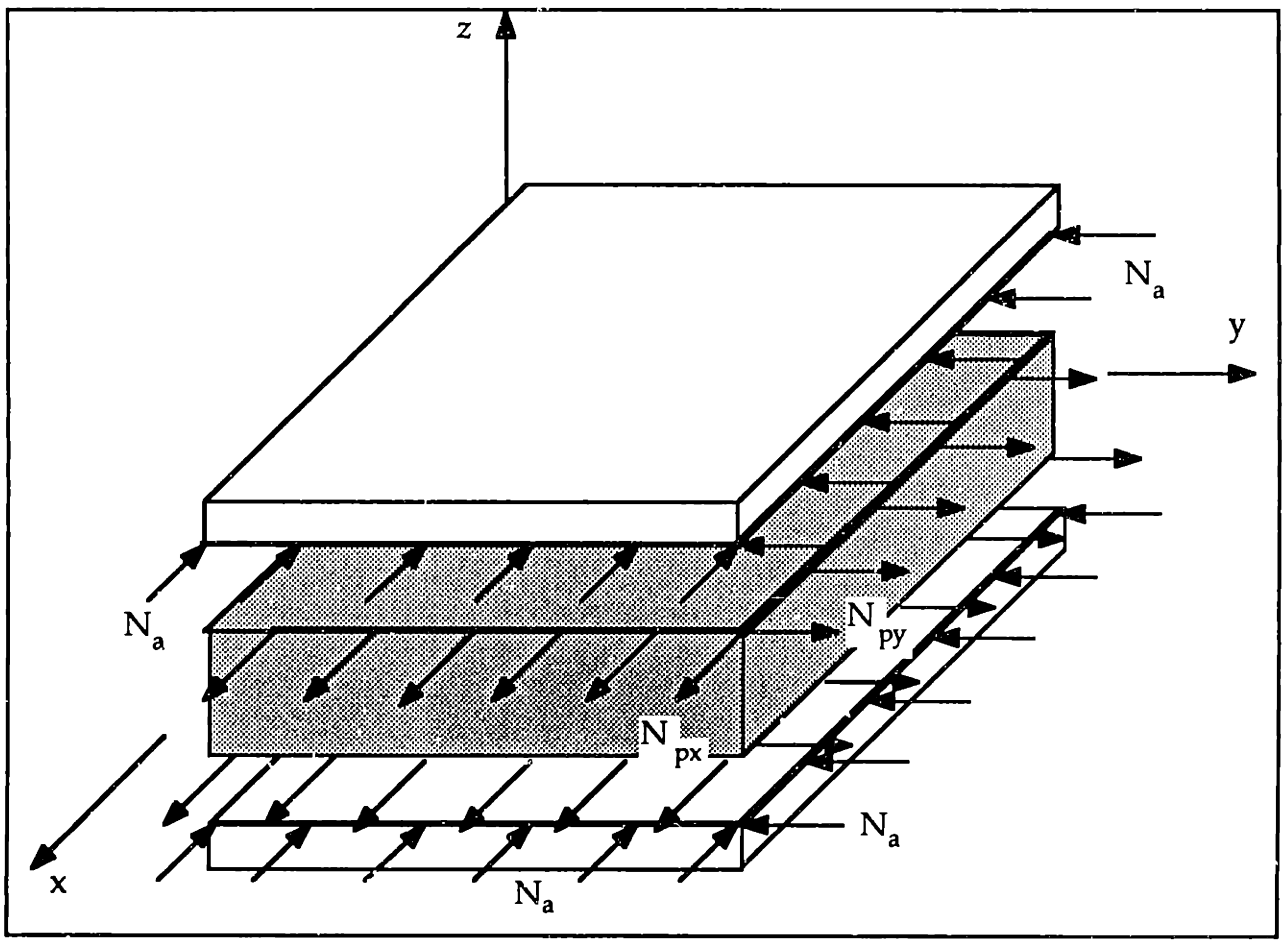

Figure 4.1: Uniform Strain Model Geometry Showing Induced Extension

A notation similar to that used in the previous chapter will be used for plates, where the subscript '*a*' refers to the actuators and the subscript '*s*' to the plate structure. The stress resultants, **N** and **M**, defined in plate theory as

$$\mathbf{N} = \int_z \sigma(z)dz \qquad \mathbf{M} = \int_z \sigma(z)z\,dz \tag{4.1}$$

and plate extensional and bending stiffness matrices, **A** and **D**,

$$\mathbf{A} = \int_z \mathbf{Q}(z)dz \qquad \mathbf{D} = \int_z \mathbf{Q}(z)z^2dz \tag{4.2}$$

will be used in the derivations below. The matrix **Q** represents the constitutive properties of a single layer. In the uniform strain model, it is assumed that the actuation and stiffness are symmetrically distributed about the neutral axis, *i.e.* the coupling stiffness matrix, **B=0**.

The solutions for uncoupled induced extensional and induced bending strain in the absence of external forces will now be derived. The uniform strain model is applicable only to surface mounted actuators, and the perfect bond assumption (Section 3.1) will be used here. The uniform strain model is strictly valid only for unconstrained plates whose surfaces are completely covered by actuators. In Section 4.5, a method for grafting this model to more realistic plate problems is outlined.

Extension

By analogy with the "pin forces" of the perfect bond beam model, it is possible to construct pin forces in a plate model. For induced extension, the distributed pin forces per unit length, N_{px}, N_{py}, and N_{pxy}, transmitted from perfectly-bonded surface-mounted actuators to a plate are in equilibrium with the stress resultants in the actuators and structure

$$\mathbf{N}_a = \mathbf{N}_p \tag{4.3}$$

$$\mathbf{N}_s = -2\mathbf{N}_p \tag{4.4}$$

The plate stress-strain relations for the actuators and a symmetric structure are

$$\varepsilon_a = \mathbf{A}_a^{-1}\mathbf{N}_a + \Lambda \tag{4.5}$$

$$\varepsilon_s = \mathbf{A}_s^{-1}\mathbf{N}_s \tag{4.6}$$

where Λ is the actuation strain vector

$$\Lambda = \begin{bmatrix} \Lambda_x \\ \Lambda_y \\ \Lambda_{xy} \end{bmatrix} \tag{4.7}$$

Substituting Eqs. 4.3 and 4.4 into Eqs. 4.5 and 4.6, and requiring displacement compatibility at the actuator-structure interfaces, gives a result for the pin forces

$$\mathbf{N}_p = -\left(2\mathbf{A}_s^{-1} + \mathbf{A}_a^{-1}\right)^{-1}\Lambda \tag{4.8}$$

and the induced strain (Eq. 4.5 or 4.6) is

$$\begin{aligned} \varepsilon &= 2\mathbf{A}_a^{-1}\left(2\mathbf{A}_s^{-1} + \mathbf{A}_a^{-1}\right)^{-1}\Lambda \\ &= 2(2\mathbf{I} + \psi_e)^{-1}\Lambda \end{aligned} \tag{4.9}$$

which is analogous to Eq. 3.15, where I is the 3x3 identity matrix, and a relative stiffness parameter *matrix*, comparable to Eq. 3.16, is defined as

$$\psi_e = \mathbf{A}_a^{-1}\mathbf{A}_s \tag{4.10}$$

Bending

In bending, a plate derivation analogous to Eqs. 3.1 through 3.14 for a beam structure proceeds as follows. The plate is assumed to be in pure bending and the actuators in uniform extension. The force resultants, M and N, in the structure and actuators are in equilibrium with the pin forces

$$\mathbf{M}_s = -\,t_s\mathbf{N}_p \tag{4.11}$$

$$\mathbf{N}_a = \mathbf{N}_p \tag{4.12}$$

The stress resultant-strain relations for the plate and actuators are

$$\varepsilon_p = z\,\kappa_p = \mathbf{D}_p^{-1}\mathbf{M} \tag{4.13}$$

$$\varepsilon_a = \mathbf{A}_a^{-1}\mathbf{N}_a + \Lambda \tag{4.14}$$

After enforcing compatibility at the actuator-plate interfaces, the pin forces are

$$\mathbf{N}_p = -\left(\mathbf{A}_a^{-1} + \frac{t_s^2}{2}\mathbf{D}_a^{-1}\right)^{-1}\Lambda \tag{4.15}$$

and the strains in the structure and upper actuator are

$$\varepsilon_s = z\,\kappa_s = zt_s\mathbf{D}_s^{-1}\left(\mathbf{A}_a^{-1} + \frac{t_s^2}{2}\mathbf{D}_a^{-1}\right)^{-1}\Lambda \tag{4.16}$$

$$\varepsilon_a = \frac{t_s^2}{2}\mathbf{D}_a^{-1}\left(\mathbf{A}_a^{-1} + \frac{t_s^2}{2}\mathbf{D}_a^{-1}\right)^{-1}\Lambda \tag{4.17}$$

Alternatively, the induced curvature is simply

$$\kappa_s = \frac{-12}{t_s}\left(\psi_b + 6\mathbf{I}\right)^{-1}\Lambda \tag{4.18}$$

where the relative stiffness parameter matrix is

$$\psi_b = \frac{12}{t_s^2}\mathbf{A}_a^{-1}\mathbf{D}_a \tag{4.19}$$

which is analogous to the scalar stiffness parameter of Eq. 3.10.

Results for Isotropic Plate

The results above are valid for any symmetric plate with surface-mounted actuators. For the specific case of an isotropic plate and actuators, the stiffnesses $\mathbf{A}_a$, $\mathbf{A}_s$, and $\mathbf{D}_s$ are

$$\mathbf{A}_a = \frac{E_a t_a}{1-\nu_a^2}\begin{bmatrix} 1 & \nu_a & 0 \\ \nu_a & 1 & 0 \\ 0 & 0 & \frac{1-\nu_a}{2} \end{bmatrix} \tag{4.20}$$

$$\mathbf{A}_s = \frac{E_s t_s}{1-\nu_s^2}\begin{bmatrix} 1 & \nu_s & 0 \\ \nu_s & 1 & 0 \\ 0 & 0 & \frac{1-\nu_s}{2} \end{bmatrix} \tag{4.21}$$

$$\mathbf{D}_s = \frac{E_s t_s^3}{12(1-\nu_s^2)}\begin{bmatrix} 1 & \nu_s & 0 \\ \nu_s & 1 & 0 \\ 0 & 0 & \frac{1-\nu_s}{2} \end{bmatrix} \tag{4.22}$$

where ν_s and ν_a are the Poisson's ratios of structure and actuators. The relative stiffness parameter matrix, ψ_e, for extension (Eq. 4.10) is

$$\psi_e = \frac{E_s t_s}{E_a t_a(1-\nu_s^2)}\begin{bmatrix} 1-\nu_a\nu_s & \nu_s-\nu_a & 0 \\ \nu_s-\nu_a & 1-\nu_a\nu_s & 0 \\ 0 & 0 & (1-\nu_s)(1+\nu_a) \end{bmatrix} \tag{4.23}$$

which is greatly simplified when $\nu_a=\nu_s$

$$\psi_e = \frac{E_s t_s}{E_a t_a}\begin{bmatrix} 1 & 0 & 0 \\ 0 & 1 & 0 \\ 0 & 0 & 1 \end{bmatrix} \tag{4.24}$$

For an isotropic plate and actuators the relative stiffness parameter matrix for bending, ψ_b, is identical to ψ_e.

The actuation strain vector, Λ (Eq. 4.7), for a typical isotropic induced strain actuator, contains no shear component and identical normal components. Therefore, it can be written

$$\Lambda = \begin{bmatrix} \Lambda \\ \Lambda \\ 0 \end{bmatrix} \tag{4.25}$$

When Eqs. 4.24 and 4.25 are placed in Eq. 4.9, the resulting induced stretching strain is

$$\varepsilon = 2\left(\left(2 + \frac{E_s t_s}{E_a t_a}\right)\mathbf{I}\right)^{-1}\begin{bmatrix} \Lambda \\ \Lambda \\ 0 \end{bmatrix} \tag{4.26}$$

or

$$\varepsilon_x = \varepsilon_y = \frac{2}{2 + \frac{E_s t_s}{E_a t_a}}\Lambda \qquad \gamma_{xy} = 0 \tag{4.27}$$

which is identical to the beam result for identical width structure and actuators (Eq. 3.15).

For the case of induced bending, the results are also similar to the one-dimensional model predictions. When Eqs. 4.24 and 4.25 are placed in Eqs. 4.16 and 4.17, the resulting strains are

$$\varepsilon_{x_s} = \varepsilon_{y_s} = \kappa_s z = \frac{6}{6 + \frac{E_s t_s}{E_a t_a}}\Lambda\left(\frac{2}{t_s}\right)z \qquad \gamma_{xy_s} = z\kappa_{xy_s} = 0 \tag{4.28}$$

$$\varepsilon_{x_a} = \varepsilon_{y_a} = \kappa_s\left(\frac{t_s}{2}\right) = \frac{6}{6 + \frac{E_s t_s}{E_a t_a}}\Lambda z \qquad \gamma_{xy_a} = \frac{t_s}{2}\kappa_{xy_s} = 0 \tag{4.29}$$

which are again identical to the beam results (Eq. 3.13) for b_s=b_a. It has been shown that for isotropic plate and actuators, the solutions for induced extensional and bending strain correctly reduce to the one-dimensional model results. Note that for isotropic actuators and structure, the two orthogonal induced strains, ε_x and ε_y, are uncoupled and identical.

4.2 LAMINATED PLATE MODEL

In this section, the strain induced in a plate by actuators embedded in or bonded to the surface of the plate will be derived. The development of this model is consistent with classical laminated plate theory and corresponds closely

to the Bernoulli-Euler beam model of Section 3.2. It is required that the plate and actuators are free of external loads. The solution of a problem which includes external loading is more easily developed with energy formulations (see Section 4.4).

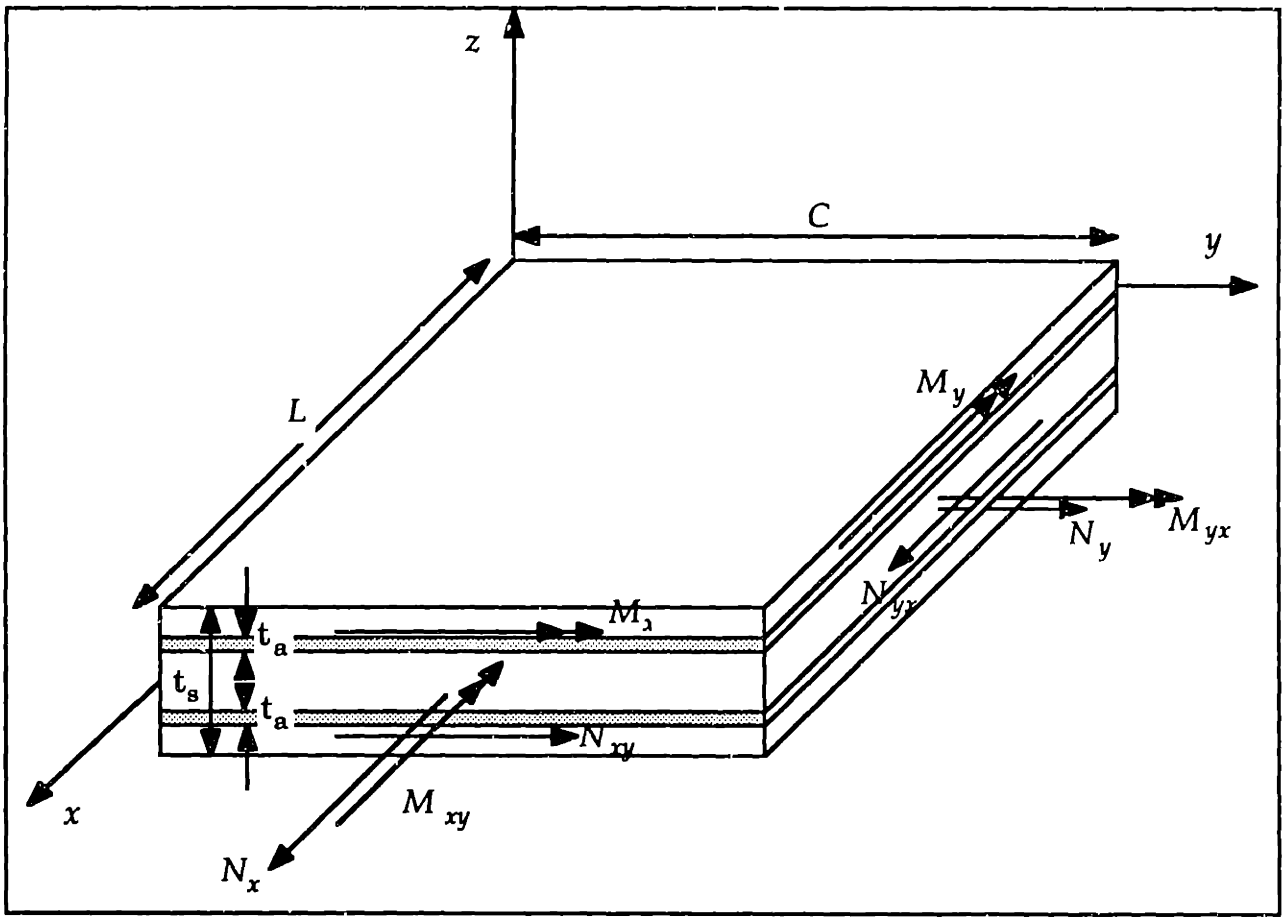

Figure 4.2: Laminated Plate Model Geometry and Resultant Definitions

Embedded Model

The induced strain due to actuators embedded at arbitrary locations through the plate thickness will now be developed. It is assumed that there are cutouts made in the structure to accommodate the actuators. Further, the bonds between actuators and plate are assumed to be 'perfect.' Since the actuators are set in place in the cure process, bonds of strength comparable to the interlaminar bond should be possible.

In plate theory (Jones, 1975), the total strain is

$$\varepsilon = \varepsilon^0 + z\,\kappa \tag{4.30}$$

where

$$\varepsilon = \begin{bmatrix} \varepsilon_x \\ \varepsilon_y \\ \gamma_{xy} \end{bmatrix} \qquad \varepsilon^0 = \begin{bmatrix} \varepsilon_x^0 \\ \varepsilon_y^0 \\ \gamma_{xy}^0 \end{bmatrix} \qquad \kappa = -\begin{bmatrix} w_{,xx} \\ w_{,yy} \\ 2w_{,xy} \end{bmatrix} \tag{4.31}$$

The generalized force-strain relations for a plate subject to actuation strain are

$$\begin{bmatrix} \mathbf{N} \\ \mathbf{M} \end{bmatrix} = \begin{bmatrix} \mathbf{A} & \mathbf{B} \\ \mathbf{B} & \mathbf{D} \end{bmatrix} \begin{bmatrix} \varepsilon^0 \\ \kappa \end{bmatrix} - \begin{bmatrix} \mathbf{N}_\Lambda \\ \mathbf{M}_\Lambda \end{bmatrix} \tag{4.32}$$

where **N** and **M** are defined in Eq. 4.1, the 3x3 total extensional, coupling, and bending stiffness matrices for the plate and actuators are

$$\mathbf{A} = \int_z \mathbf{Q}(z)dz \qquad \mathbf{B} = \int_z \mathbf{Q}(z)zdz \qquad \mathbf{D} = \int_z \mathbf{Q}(z)z^2dz \tag{4.33}$$

and the internal force resultants, created by the actuation strain Λ are

$$\mathbf{N}_\Lambda = \int_z \mathbf{Q}(z)\Lambda(z)dz \qquad \mathbf{M}_\Lambda = \int_z \mathbf{Q}(z)\Lambda(z)zdz \tag{4.34}$$

For the case of no external forces, the six induced strains and curvatures are determined by setting Eq. 4.32 equal to zero

$$\begin{bmatrix} \varepsilon^0 \\ \kappa \end{bmatrix} = \begin{bmatrix} \mathbf{A} & \mathbf{B} \\ \mathbf{B} & \mathbf{D} \end{bmatrix}^{-1} \begin{bmatrix} \mathbf{N}_\Lambda \\ \mathbf{M}_\Lambda \end{bmatrix} \tag{4.35}$$

From Eq. 4.35 it is clear that for unsymmetric plates ($\mathbf{B} \neq \mathbf{0}$) it is possible to induce inplane stretching and shearing by application of an actuation moment, $\mathbf{M}_\Lambda$, or out-of-plane bending or twisting with an actuation force, $\mathbf{N}_\Lambda$. In addition, for a symmetric but generally orthotropic laminate, it is possible to utilize extension-shearing coupling ($A_{16}, A_{26} \neq 0$) or bending-torsion coupling ($D_{16}, D_{26} \neq 0$). This coupling must be exploited to induce shearing or twisting when the actuation strain has no shear component (Eq. 4.25). Lazarus (1989) conducted experiments with $(+45_3/-45_3)$ and $(30_2/0)_s$ laminates to induce twisting due to coupling with extension and bending.

Results for Isotropic Plate

In order to compare the plate and beam models, specialization to the case of an isotropic plate with actuation symmetric about the neutral axis is required. Extension and bending may then be treated separately. For the case of extension, from Eq. 4.35, the inplane strain is

$$\boldsymbol{\varepsilon}^0 = \mathbf{A}^{-1}\mathbf{N}_\Lambda \tag{4.36}$$

the total extensional stiffness is

$$\mathbf{A} = \mathbf{A}_s + \mathbf{A}_a \tag{4.37}$$

where $\mathbf{A}_s$ and $\mathbf{A}_a$ are given by Eqs. 4.20 and 4.21. If it is assumed that the structure and actuators have identical Poisson's ratios ($\nu_a=\nu_a=\nu$), $\mathbf{A}$ simplifies to

$$\mathbf{A} = \frac{E_s(t_s - 2t_a) + E_a t_a}{1-\nu^2}\begin{bmatrix} 1 & \nu & 0 \\ \nu & 1 & 0 \\ 0 & 0 & \dfrac{1-\nu}{2} \end{bmatrix} \tag{4.38}$$

and the actuation force resultant, measured in force per unit length, is

$$\mathbf{N}_\Lambda = \frac{2E_a t_a}{1-\nu^2}\begin{bmatrix} 1 & \nu & 0 \\ \nu & 1 & 0 \\ 0 & 0 & \dfrac{1-\nu}{2} \end{bmatrix}\Lambda \tag{4.39}$$

Using an actuation strain (Eq. 4.25) which is typical, with $\Lambda_x=\Lambda_y=\Lambda$, $\mathbf{N}_\Lambda$ simplifies to

$$\mathbf{N}_\Lambda = \begin{bmatrix} N_x \\ N_y \\ N_{xy} \end{bmatrix} = \frac{2E_a t_a}{1-\nu}\begin{bmatrix} \Lambda \\ \Lambda \\ 0 \end{bmatrix} \tag{4.40}$$

Thus, the x and y components of Eqs. 4.38 and 4.40 are identical to Eqs. 3.32 and 3.33 except for the finite width term, b, and the $1-\nu$ and $1-\nu^2$ terms in the denominators representing the increased stiffness in plates. Placing Eqs. 4.38 and 4.40 into Eq. 4.36, the induced extensional strain is

$$\varepsilon^0 = \mathbf{A}^{-1}\mathbf{N}_\Lambda = \frac{2E_a t_a}{E_s(t_s - 2t_a) + E_a t_a}\begin{Bmatrix} \Lambda \\ \Lambda \\ 0 \end{Bmatrix} \tag{4.41}$$

or

$$\varepsilon_x^0 = \varepsilon_y^0 = \frac{2\Lambda}{2 + \psi_e} \qquad \gamma_{xy}^0 = 0 \tag{4.42}$$

where the scalar relative stiffness parameter is

$$\psi_e = \frac{A_s}{A_a} = \frac{E_s(t_s - 2t_a)}{E_a t_a} \tag{4.43}$$

which is identical to the definition of ψ_e for a beam (Eq. 3.35) except for the absence of a finite width term.

Under the same conditions, the solution to the bending problem is

$$\kappa = \mathbf{D}^{-1}\mathbf{M}_\Lambda \tag{4.44}$$

$$\mathbf{D} = \mathbf{D}_s + \mathbf{D}_a \tag{4.45}$$

$$= \frac{1}{1-\nu^2}\left\{E_s\left[\frac{t_s^3}{12} - t_a\left(d^2 + dt_a + \frac{t_a^3}{3}\right)\right] + 2E_a t_a\left(d^2 + dt_a + \frac{t_a^3}{3}\right)\right\}\begin{bmatrix} 1 & \nu & 0 \\ \nu & 1 & 0 \\ 0 & 0 & \frac{1-\nu}{2} \end{bmatrix} \tag{4.46}$$

$$\mathbf{M}_\Lambda = \frac{2E_a t_a}{1-\nu^2}\left(d + \frac{t_a}{2}\right)\begin{bmatrix} 1 & \nu & 0 \\ \nu & 1 & 0 \\ 0 & 0 & \frac{1-\nu}{2} \end{bmatrix}\Lambda \tag{4.47}$$

$$\kappa = \frac{2E_a t_a\left(d + \frac{t_a}{2}\right)}{\left\{E_s\left[\frac{t_s^3}{12} - t_a\left(d^2 + dt_a + \frac{t_a^3}{3}\right)\right] + 2E_a t_a\left(d^2 + dt_a + \frac{t_a^3}{3}\right)\right\}}\Lambda \tag{4.48}$$

$$\kappa_x = \kappa_y = \frac{2E_a t_a\left(d + \frac{t_a}{2}\right)}{\left\{E_s\left[\frac{t_s^3}{12} - t_a\left(d^2 + dt_a + \frac{t_a^3}{3}\right)\right] + 2E_a t_a\left(d^2 + dt_a + \frac{t_a^3}{3}\right)\right\}} \Lambda$$

$$\kappa_{xy} = 0 \tag{4.49}$$

which is identical to Eq. 3.40, except for the exclusion of the finite width term.

Surface Mounted Models

For surface-bonded actuators, Eq. 4.42 applies for extension, with

$$\psi_e = \frac{E_s t_s}{E_a t_a} \tag{4.50}$$

For bending, Eq. 4.49 applies, with $d=t_s/2$ and

$$\kappa_x = \kappa_y = \frac{6\left(1 + \frac{1}{T}\right)\Lambda\left(\frac{2}{t_s}\right)}{(6 + \psi) + \frac{12}{T} + \frac{8}{T^2}} \qquad \kappa_{xy} = 0 \tag{4.51}$$

where T is the ratio of the plate and actuator thicknesses

$$T = \frac{t_s}{t_a} \tag{4.52}$$

The predicted induced curvature in Eq. 4.51 is identical to the predicted beam curvatures for $b_s=b_a$ (Eq. 3.46).

The laminated plate model can be viewed as a generalization of the one-dimensional Bernoulli-Euler model of Section 3.2. It has been demonstrated that for isotropic and symmetric structure and actuators the solutions are identical.

4.3 Comparison of Models

From the previous two sections, it is apparent that the two plate models correctly reduce to the corresponding beam models. Thus, the comparisons for induced extensional strain (Fig. 3.7) and induced curvature (Fig. 3.8) which were

shown for identical width beam structure and actuators are applicable to plate structures as well. The two plate models predict identical induced extensional strains. The laminated plate model is more accurate than the uniform strain model for induced bending, particularly for thin plates.

The illustrations of the effects of finite stiffness bonding layers and material shear, shown for beams in the previous chapter, are applicable to plates as well. Expressions similar to Eqs. 3.61 and 3.62 may be written to predict the effect of finite stiffness bonding layers in both the x and y directions. A more complicated model must be used when shear or twist is induced in an elastically-coupled plate. The finite element model with material shear included could also be generalized to isotropic plates with surface-bonded actuators. Reductions in net displacement in the two directions are expected to be proportionally somewhat greater because of increased losses near corners of the actuators.

The more complicated nature of plates makes the laminated plate model more straightforward for use in design. This is particularly true for embedded actuators where only the laminated plate model is applicable. The extension, bending, and coupling may be solved simultaneously using the actuation force resultants, $\mathbf{N}_\Lambda$, and $\mathbf{M}_\Lambda$.

Either model provides an accurate description only in the absence of external forces over a free section of plate. In reality, the effect of the actuation strain depends strongly on the (static or dynamic) loading on and boundary conditions of the plate. Therefore, it is necessary to couple the simple induced strain models to more complete models which encompass the entire plate behavior. A more general approach, which often involves approximate solutions, is based on the energy formulations discussed in the next two sections.

4.4 ENERGY FORMULATION

In order to solve a realistic problem, the solutions for induced strain must be integrated with a more general structural model which includes the effects of external mechanical loading and boundary conditions. In determining deformations in both static and dynamic problems it becomes necessary to employ either an exact representation of global deformation or an approximate representation. The later is required for dynamic problems.

In the previous chapter, a five-mode Ritz model was used to predict dynamic motion of the beams. In the present section, the formal energy expressions for the plate problem will be derived. The consistency with the laminated plate model will be illustrated. Finally, the derivation will be specialized to the cases for which experimental results were obtained.

Potential and Kinetic Energy

The total energy consists of the sum of the potential energy and kinetic energy. In static problems, kinetic energy is not present. The potential energy is

$$U = \tfrac{1}{2}\int_V \varepsilon^T \mathbf{Q} \varepsilon dV - \int_V \varepsilon^T \mathbf{Q} \Lambda dV \tag{4.53}$$

where $\mathbf{Q}$ is the lamina stiffness matrix, Λ is the actuation strain vector, and the total strain vector, ε, is

$$\varepsilon = \varepsilon^0 + z\kappa \tag{4.54}$$

Placing the strain in the expression for strain energy and separating the integrations over the area and through the thickness yields

$$U = \tfrac{1}{2}\int_A \left\{ \varepsilon^{0^T} \int_z \mathbf{Q} dz\, \varepsilon^0 + \varepsilon^{0^T} \int_z \mathbf{Q} z dz\, \kappa + \kappa \int_z \mathbf{Q} z dz\, \varepsilon^0 + \kappa \int_z \mathbf{Q} z^2 dz\, \kappa \right\} dA$$

$$- \int_A \left\{ \varepsilon^{0^T} \int_z \mathbf{Q} \Lambda dz + \kappa^T \int_z \mathbf{Q} \Lambda z dz \right\} dA \tag{4.55}$$

which may be rewritten

$$U = \tfrac{1}{2}\int_A \left\{ \varepsilon^{0^T} \mathbf{A} \varepsilon^0 + \varepsilon^{0^T} \mathbf{B} \kappa + \kappa^T \mathbf{B} \varepsilon^0 + \kappa^T \mathbf{D} \kappa \right\} dA$$

$$- \int_A \left\{ \varepsilon^{0^T} \mathbf{N}_\Lambda + \kappa^T \mathbf{M}_\Lambda \right\} dA \tag{4.56}$$

where the extensional, coupling, and bending stiffness matrices $\mathbf{A}$, $\mathbf{B}$, and $\mathbf{D}$ (Eq. 4.33), and the actuation force resultants (Eq. 4.34), $\mathbf{N}_\Lambda$ and $\mathbf{M}_\Lambda$ are used. The first integral corresponds to the strain energy found in any anisotropic plate. The

second represents the effect of the induced strain actuation. The potential energy formulation contains the same terms used in the laminated plate model.

The kinetic energy in a plate is in general

$$T = \int_V \rho \, \dot{\mathbf{u}} \cdot \dot{\mathbf{u}} dV \tag{4.57}$$

where the velocity vector $\dot{\mathbf{u}}$ is

$$\dot{\mathbf{u}} = \frac{\partial}{\partial t} \begin{pmatrix} u \\ v \\ w \end{pmatrix} \tag{4.58}$$

or

$$\begin{aligned} \frac{\partial u}{\partial t} &= \frac{\partial u^0}{\partial t} - z \frac{\partial^2 w}{\partial x \partial t} \\ \frac{\partial v}{\partial t} &= \frac{\partial v^0}{\partial t} - z \frac{\partial^2 w}{\partial y \partial t} \\ \frac{\partial w}{\partial t} &= \frac{\partial w}{\partial t} \end{aligned} \tag{4.59}$$

so the kinetic energy is

$$\begin{aligned} T = & \int_V \rho \left(\frac{\partial w}{\partial t} \right)^2 dV \\ & + \int_V \rho \, z^2 \left\{ \left(\frac{\partial^2 w}{\partial x \partial t} \right)^2 + \left(\frac{\partial^2 w}{\partial y \partial t} \right)^2 \right\} dV \\ & + \int_V \rho \left\{ \left(\frac{\partial u^0}{\partial t} \right)^2 + \left(\frac{\partial v^0}{\partial t} \right)^2 \right\} dV \\ & - 2 \int_V \rho \, z \left\{ \left(\frac{\partial u^0}{\partial t} \frac{\partial^2 w}{\partial x \partial t} \right) + \left(\frac{\partial v^0}{\partial t} \frac{\partial^2 w}{\partial y \partial t} \right) \right\} \end{aligned} \tag{4.60}$$

where the first term, corresponding to the out-of-plane deflection, usually dominates. The second term, representing rotary inertia, is not important for thin plates. The third, representing time-varying inplane stretching deformation, is likely to be important only at high frequencies. The fourth term,

representing a coupling inertia, is only nonzero for mass which is not symmetrically distributed about the centroidal axis.

Thus, in most cases

$$T = \rho t_s \int_A \left(\frac{\partial w}{\partial t} \right)^2 dA \tag{4.61}$$

is an adequate representation of the kinetic energy. General expressions for the potential and kinetic energy have been presented. Solution methods for plate problems with various loadings and boundary conditions will be discussed next.

4.5 SOLUTION OF STATIC AND DYNAMIC PROBLEMS

In general, it will be necessary to use approximate methods, based on the energy expressions (Eqs. 4.56 and 4.60). The exact equations for induced strain from Sections 4.1 and 4.2 are applicable only in a special class of static problems. The alternatives for solution of static and dynamic problems, particularly those involving out of plane displacement, w, will now be presented.

Exact Solutions

For a plate which is completely unconstrained (*i.e.* all edges are "free"), it is possible to use the static solutions for induced strains in Sections 4.1 and 4.2 when actuation strain is uniformly applied over the entire area of the plate. In that case, there is no externally imposed strain. The exact solution is also valid in cases where the edges are constrained normal to the plate but free to move tangent to it. For induced bending or twisting, the plate must have constant curvature in order for the exact solutions to be valid.

Approximate Solutions

In all other cases, an approximate solution technique must be employed. These cases include all dynamic problems and all static problems excluding the special instances noted above. The necessary approximate solution motivates the energy formulation of the previous section. For static problems only the potential energy, U (Eq. 4.56), is used. For dynamic problems, the kinetic energy, T (Eq. 4.60 or 4.61), is also necessary.

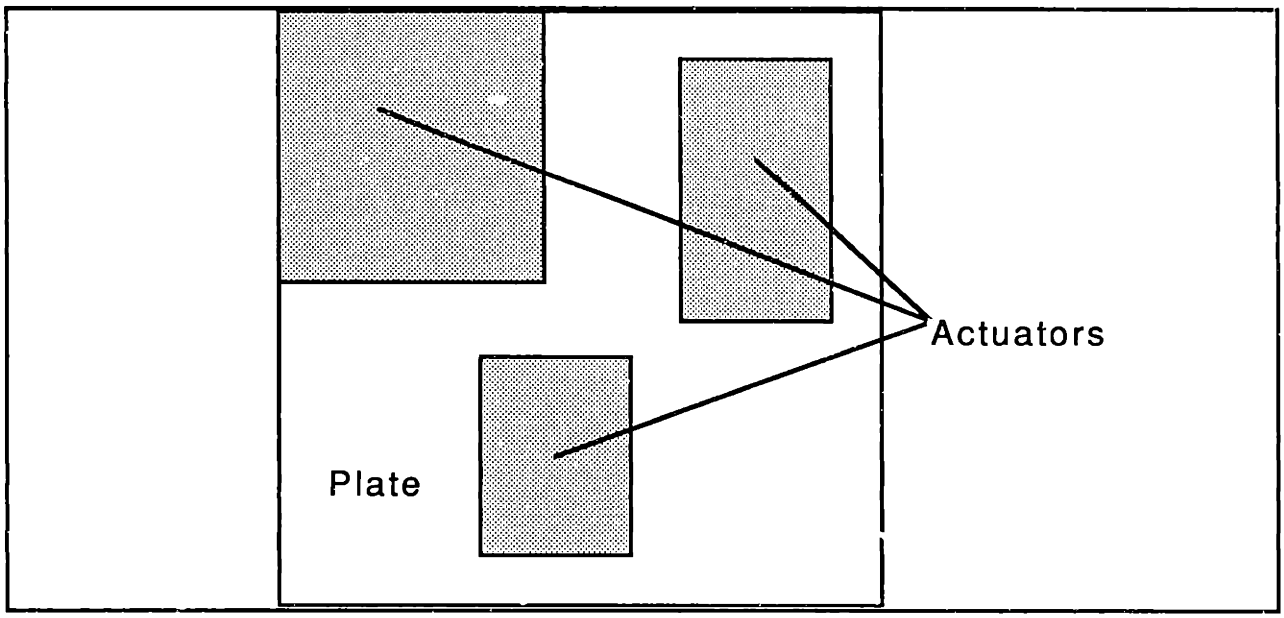

Figure 4.3: Actuation Distribution Requiring Approximate Static Solution

As an example of the need for approximate solutions, consider a plate with constant actuation strain applied over selected portions of its surface (Fig. 4.3). The exact solutions for induced strains (*e.g.* Eq. 4.41) are not valid because of the constraining effect of the uncovered plate area. The induced strain in the plate in the area of actuation strain application will be reduced. In addition, there will be nonzero strain induced in the uncovered areas, particularly near the actuation source.

In addition to the inaccurate representation of strain near the actuation sources, induced strain will be influenced by the boundary conditions. Thus, the exact model, which assumes that the induced strain is either zero (in the uncovered area) and constant (in the covered area) is not accurate. If the boundary conditions are varied (*i.e.* other than "free"), further constraints will be added, necessitating an approximate solution, even in the case of actuation strain uniformly distributed over the entire plate.

A typical static problem may be solved approximately by employing finite elements, boundary elements, finite differences, or an assumed modes Rayleigh-Ritz solution. Only the fourth method will be discussed here. For a Rayleigh-Ritz analysis, the expression for potential energy (Eq. 4.56) may be written as a function of the displacements u, v, and w.

$$U = U(u, v, w) \tag{4.62}$$

Each displacement is then written as a summation of modes

$$u = \bar{u}_i \alpha_i(x, y) \tag{4.63}$$

$$v = \bar{v}_i \beta_i(x, y) \tag{4.64}$$

$$w = \bar{w}_i \gamma_i(x, y) \tag{4.65}$$

The modal displacement vector, $\mathbf{q}$, is assembled from $\bar{u}$, $\bar{v}$, and $\bar{w}$. In many cases only the out-of-plane displacement w is important. The variation of the potential energy with respect to each of the modal displacements is required to be zero leading to a set of equations

$$\mathbf{K}\,\mathbf{q} = \mathbf{Q} \tag{4.66}$$

where the stiffness matrix, $\mathbf{K}$, is the usual stiffness matrix of both the plate and actuators, and is derived from the first term of Eq. 4.56. The modal forcing, $\mathbf{Q}$, results from the second term of Eq. 4.56, and is therefore directly proportional to the actuation strain, Λ. The modal displacements, $\mathbf{q}$, may be solved for and multiplied by the mode shapes to find the displacements. The accuracy in representation of the real induced displacements depends on both the number and the appropriateness of the chosen modes.

For dynamic applications, the problem is formulated in the same way as the static one with the addition of a modal kinetic energy term, so that the usual set of (undamped) equations

$$\mathbf{M}\ddot{\mathbf{q}} + \mathbf{K}\mathbf{q} = \mathbf{Q} \tag{4.67}$$

is obtained. All the information relating to the actuation strain is contained in the modal force vector, $\mathbf{Q}$. A damping matrix, C, may be added, and determined independently from the induced strain. Solution of Eq. 4.67, and assembling of the modes will yield the temporally- and spatially-varying displacements u, v, and w. An example of an approximate solution of the form of Eq. 4.67 is illustrated in the next section.

Based on the discussion above, it may be concluded that the expressions for induced strain in Section 4.2 have only limited use in predicting global

deformation. For all dynamic problems, and most static ones, formulation of potential and kinetic energy expressions will lead directly to approximate solutions. In addition, in such formulations, additional external inputs may be readily accommodated in the stiffness and mass matrices. Thus, an energy formulation is strongly recommended.

4.6 EXPERIMENTS AND RESULTS

In order to verify analytical formulations, a set of simple dynamic experiments was conducted. In this section, the design, apparatus, and results of those experiments will be presented. The approximate method used to determine the extent of the induced deflections in one test will be described.

Design

The design of a plate structure incorporating induced strain actuation requires several decisions, including choice of actuator material, whether to embed or place the actuators on the surface, and the layout of the actuators. The actuation strain distribution depends on the intended purpose of that actuation. For shape control, a large network of independent actuators is desirable. For vibration control of specific dynamic modes, it is desirable to distribute the actuation such that maximum influence is exerted on those modes.

A concept which allows modal control is that of a "modal actuator." Such an actuator has been constructed for a beam (Lee and Moon, 1987) Unfortunately, it is not possible to construct such an actuator for a plate. Any actuator will exert influence over multiple modes. In particular, an actuator which is cut to coincide with the strain shape of the exact first bending mode of a cantilevered plate, will only partially succeed. If it is assumed that the actuator does not change the stiffness and mass properties of the plate, it will not affect any of the higher spanwise bending modes, because they are by definition orthogonal. However, when a bidirectional induced strain actuator, such as a piezoceramic, is used, chordwise bending modes will be excited as well. If multiple modes must be controlled, other modal actuators may be constructed, or a distributed network of actuators may be used.

The purpose of this study was to verify the models of two-dimensional induced strain actuation. Therefore, it was determined that a simple actuator

arrangement could be used to exert authority on various modes. The arrangement, consisting of two curvature actuators, allowed excitation of spanwise and chordwise bending, and with a reversal of input to one actuator, excitation of torsion.

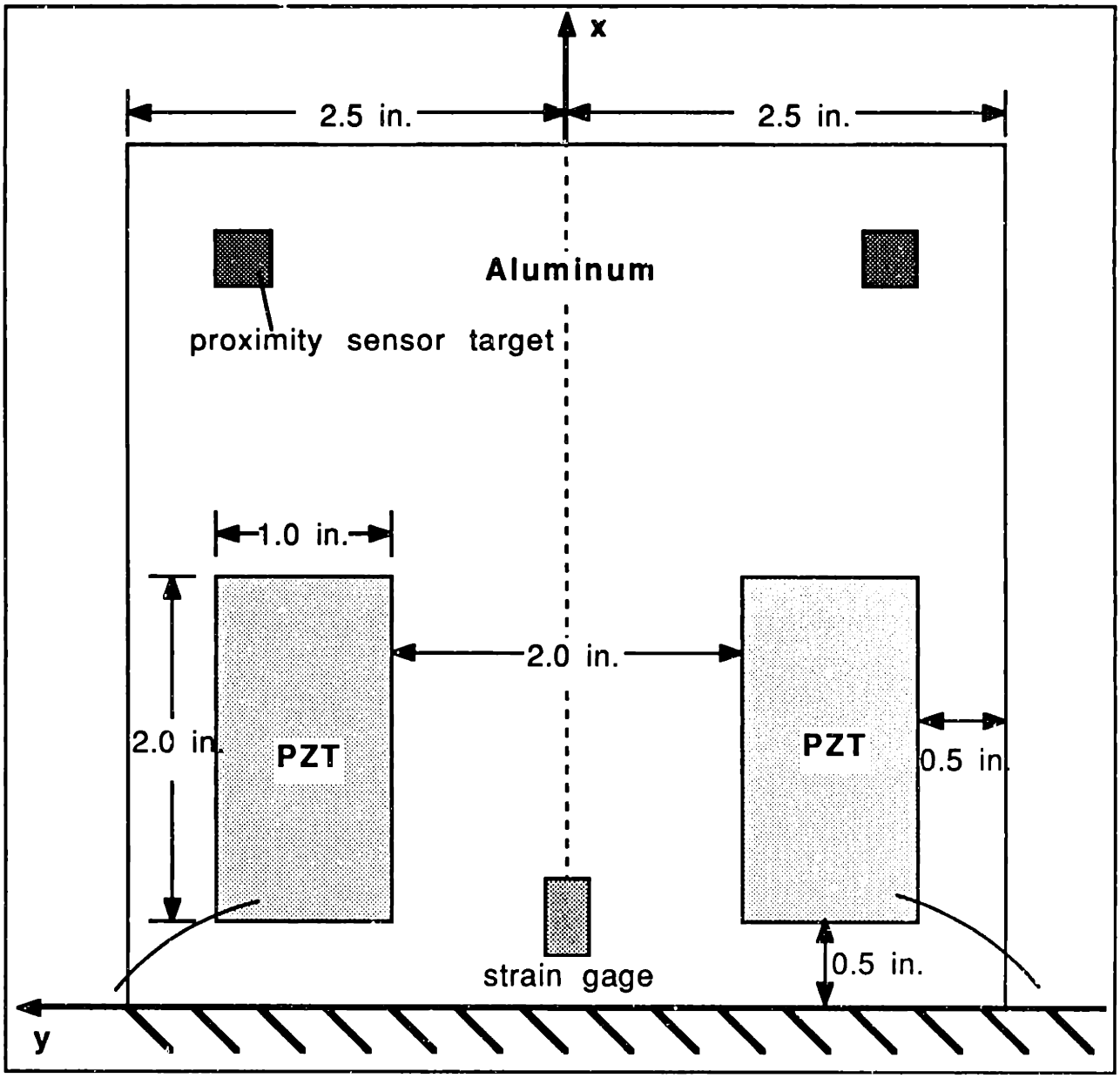

Figure 4.4: Plate Test Specimen

The actuators were located near the base of the clamped plate, at points of highest strain in the first bending and first torsion modes, in order to exert maximum influence over those modes.

Apparatus

An aluminum test specimen with surface-mounted PZT actuators was constructed (Fig. 4.4). The plate was cut from 2024 aluminum, and had exposed dimensions 5 in. by 5 in. (aspect ratio = 1) by 1/32 in. thick. An additional 4 by 5 in. of material was clamped. Two pairs of Piezoelectric Products G-1195 PZT piezoceramics, with dimensions 1 x 2 inches, were bonded to the plates with Emerson Cuming Amicon epoxy. The aluminum plate was used as an electrical ground in the experiments. Therefore, a small quantity of conductive epoxy (Emerson and Cuming Eccobond 83-C) was placed at the center of the the actuator plate interface. Two actuators were bonded to one side of the plate, then, in a separate cure, the other two actuators were bonded to the other side of the plate. The specimen was instrumented with a strain gage in the center (y=0) of the plate 1/2 inch from the base, and with steel proximity sensor targets near the upper corners.

A sinusoidal input voltage was supplied to the actuator pairs in order to induce curvature in the plate. When the actuators were strained in phase, the net effect was to excite modes symmetric about the y=0 axis (*i.e.* spanwise and symmetric chordwise bending modes). When the actuators were strained 180 degrees out-of-phase, the net effect was to excite antisymmetric modes (i.e. torsion and antisymmetric chordwise bending). Data were measured for the first torsion and first spanwise bending modes.

For the purpose of correlating the approximate analytical model, measurements of deflection at the first bending resonance were made with the two magnetic proximity sensors. In order to predict the amplitude of motion, damping measurements were made. The plate was excited at resonance then the excitation was cut off and the plate allowed to ring down. An amplitude-dependent damping ratio was then determined using a least squares fitting program. Because of nonlinear structural and air damping, the damping ratio was higher at higher amplitudes.

The plate was excited for field levels up to 30 V/mm peak, corresponding to peak tip deflections of approximately one plate thickness. Above this level the amplitude of vibration approached the saturation of the proximity sensors. In

addition, at the small amplitudes, the linear plate model could be considered accurate.

Results

In order to accurately predict the amplitude of vibration, it was necessary to include several mode shapes. In a Rayleigh-Ritz model, stiffness, mass, and forcing must be represented (Eq. 4.67). For the chosen arrangement of actuators (Fig. 4.4), all three quantities are discontinuous at the actuator locations. There-

Table 4.1: Assumed Mode Shapes for Rayleigh-Ritz Plate Model

Mode number	$\phi(x)$	$\varphi(y)$
1 - 5	$\cosh(\lambda_i \frac{x}{L}) - \cos(\lambda_i \frac{x}{L}) - \mu_i(\sinh(\lambda_i \frac{x}{L}) - \sin(\lambda_i \frac{x}{L}))$ (λ_i, μ_i, defined in Appendix E)	1
6	$\cosh(\lambda_1 \frac{x}{L}) - \cos(\lambda_1 \frac{x}{L}) - \mu_1(\sinh(\lambda_1 \frac{x}{L}) - \sin(\lambda_1 \frac{x}{L}))$	$(\frac{y}{c})^2$
7	$\cosh(\lambda_2 \frac{x}{L}) - \cos(\lambda_2 \frac{x}{L}) - \mu_2(\sinh(\lambda_2 \frac{x}{L}) - \sin(\lambda_2 \frac{x}{L}))$	$(\frac{y}{c})^2$
8	$\begin{cases} 0 & x < a_1 \\ \frac{1}{l^2}(x - a_1)^2 & a_1 \le x \le a_2 \\ \frac{1}{l^2}(a_2 - a_1)^2 + \frac{1}{l^2}(a_2 - a_1)(x - a_2) & x > a_2 \end{cases}$	1
9		$(\frac{y}{c})^2$
10		$\begin{cases} 0 & \lvert y \rvert < b_1 \\ \frac{1}{c^2}(\lvert y \rvert - b_1) & b_1 \le \lvert y \rvert \le b_2 \\ \frac{1}{c^2}(b_2 - b_1)^2 + \frac{1}{c^2}(b_2 - b_1)(\lvert y \rvert - b_2) & \lvert y \rvert > b_2 \end{cases}$

fore, in an assumed modes model, it is useful to include some modes which are discontinuous.

The experimental first bending mode was used to evaluate the approximate model. A total of ten modes were assumed in the Rayleigh-Ritz model. Table 4.1 lists the assumed mode shapes. Each mode shape consists of x and y components

$$\gamma_i(x, y) = \phi_i(x)\varphi_i(y) \tag{4.68}$$

Since the piezoceramics produced equal actuation strains in all directions in the plane, it was necessary to include some chordwise dependence in y through $\varphi_i(y)$.

The first five modes used were the exact cantilevered-free beam modes in x, with no chordwise variation. Modes 6 and 7 included the addition of asymmetric, parabolic (constant curvature) chordwise deformation to the first

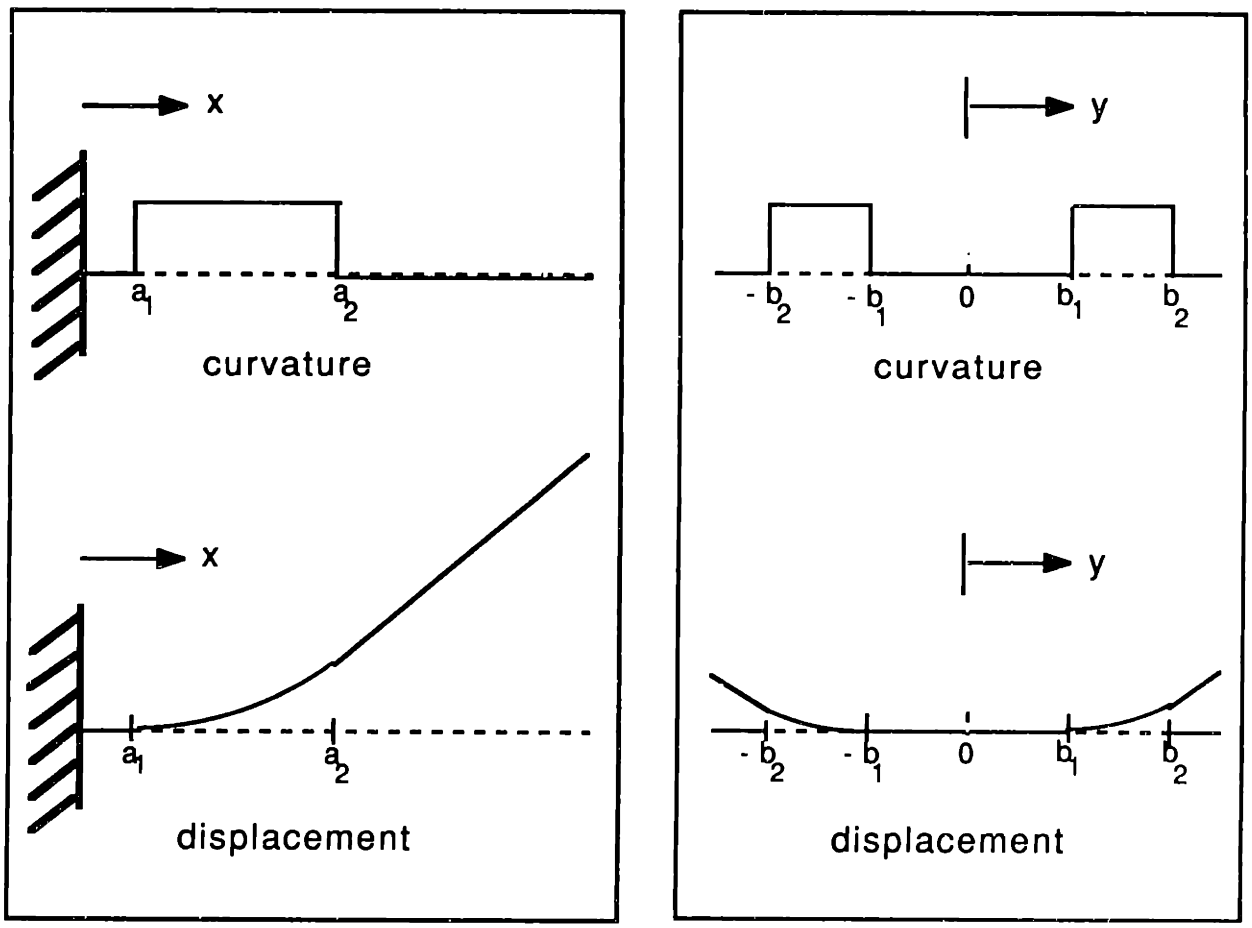

a) Spanwise Modes 8, 9, and 10

b) Chordwise Mode 10

Figure 4.5: Assumed 'Exact Static' Mode Shapes

two cantilevered-free bending modes. Modes 8, 9, and 10 assume the exact static mode as predicted by the laminated plate model in x. That is, a constant curvature, κ_x, is assumed at the actuator locations, and zero curvature elsewhere (Fig. 4.5a). This assumption for curvature leads to displacements which are zero up to a_1, parabolic from a_1 to a_2, and linear from a_2 to the tip of the plate. In the chordwise direction, the three assumed mode shapes in modes 8, 9, and 10 are constant, parabolic, and the "exact static" (Fig. 4.5b) modes. The static mode shapes were necessary to accurately represent the discontinuities in strain and stiffness which occur at the actuator edges, particularly in the modal stiffness and forcing.

The total modal stiffness, mass, and forcing matrices, based on the potential and kinetic energy expressions of Eqs. 4.56 and 4.61 were defined as follows for the isotropic plate and actuators

$$K_{ij} = \int_A \Big\{ D_{11}\gamma_{i,xx}\gamma_{j,xx} + D_{22}\gamma_{i,yy}\gamma_{j,yy} + 4D_{66}\gamma_{i,xy}\gamma_{j,xy} + D_{12}\left(\gamma_{i,xx}\gamma_{j,yy} + \gamma_{i,yy}\gamma_{j,xx}\right)\Big\} dA \tag{4.69}$$

$$M_{ij} = \int_A \gamma_i \, m \, \gamma_j \, dA \tag{4.70}$$

$$Q_j = \int_A M_A\left(\gamma_{j,xx} + \gamma_{j,yy}\right) dA \tag{4.71}$$

where the bending stiffness, D, mass density, m, and actuation moment, M_A, all are discontinuous at the edges of the actuators. The integrals over the plate and the actuators were actually done separately. A 16-point Gaussian integration in both x and y directions was used. The same integration scheme was used for both the plates and actuators. The number of integration points was considered adequate. For the integration of all continuous modes and integration over the actuators, there was no detectable difference between the numerical and exact integrations, where the exact results were available. Since the discontinuous modes (ϕ_8, ϕ_9, ϕ_{10}, and φ_{10}) are continuous over the actuator areas, all numerical integrations over the actuators were nearly exact. The integration of the discontinuous modes over the plate was still highly accurate. For the curvature

of modes ϕ_8, ϕ_9, and ϕ_{10}, for example, the numerical integration gave a result roughly 1.5% above the exact value.

Based on the model, the predicted first mode frequency was 48.6 Hz. The measured frequency was 44.3 Hz. The discrepancy is due in part to the exclusion of the two proximity targets present near the tip of the plate from the model. The effect of these masses was to lower the natural frequency of the plate, but not alter the mode shape.

The model was run using the small-signal d_{31} value for G-1195, *i.e.* d_{31}=180pm/V. The field levels applied (<30V/mm), and the values of induced strain (<3μS) were so low that the use of d_{31} was justified. Since the Rayleigh-Ritz model was linear, it was run just once, for an actuation strain of Λ=1μS. Then, the Λ corresponding to each applied field was used to determine actual predicted displacement.

Table 4.2: First Mode Bending Predictions and Data (Plate)

Field (V/mm)	Damping Ratio (%)	Displacement(w/t)		Error
		Predicted	Data	
2.78	.656	.107	.094	+14.0%
5.57	.676	.207	.188	+10.2%
8.35	.697	.304	.286	+6.2%
11.1	.718	.394	.383	+2.8%
13.9	.738	.479	.474	+0.9%
16.7	.755	.562	.554	+1.3%
19.5	.772	.641	.632	+1.4%
22.3	.787	.718	.704	+2.0%
25.1	.801	.794	.769	+3.4%
27.8	.815	.867	.833	+4.2%

Table 4.2 shows the electric field, damping ratio used in the model, and the predicted and measured displacements and error. The damping ratio was determined from the ringdown data. Even for relatively small displacements in

the test, there was significant increase in the damping ratio over the amplitude range tested. The increased damping is believed to be due to both aerodynamic damping and increased damping at the clamp. The displacements shown are normalized by plate thickness. The displacements measured at the two corners of the plate differed by no than 1.2% over the entire field range. An average value is reported here. There is excellent agreement between the predictions and the measured data (Fig. 4.6).

If d^*_{31} had been used in place of d_{31} the predicted amplitudes would have been slightly (<5%) higher for the larger input fields. It is believed that the shear parameter, Γ (Section 3.4) was large enough to justify the perfect bond assumption. It is possible that the experimental amplitudes were decreased by a few percent because of the finite stiffness bonds.

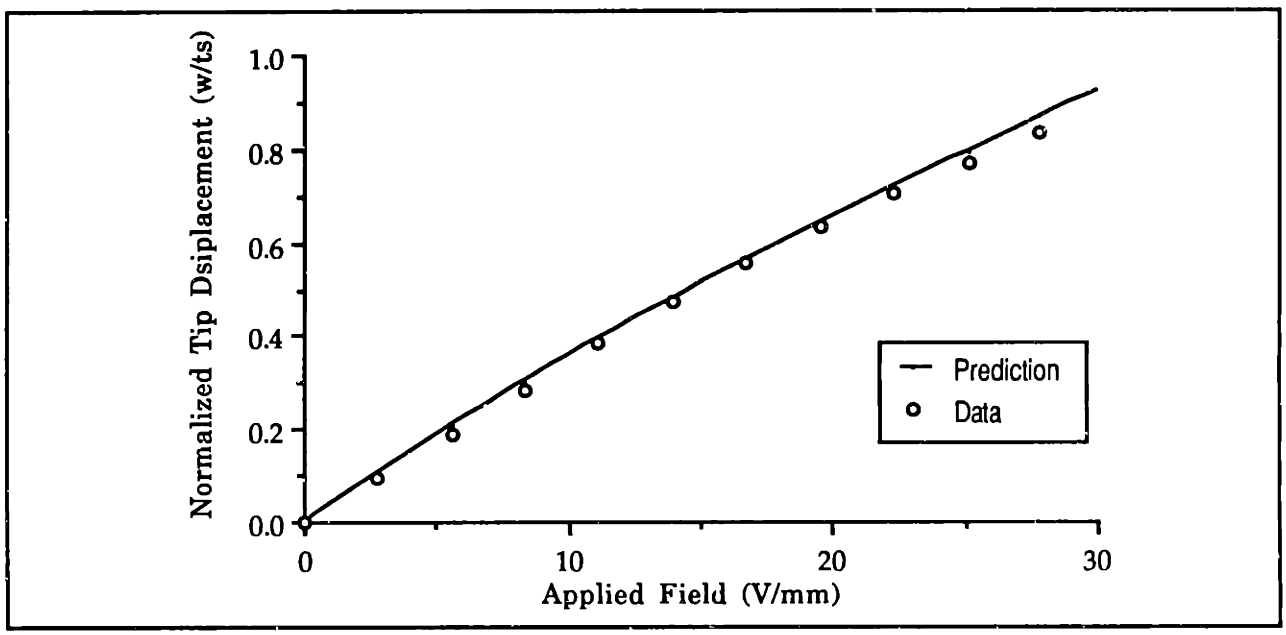

Figure 4.6: Measured and Predicted Plate Tip Displacement in First Bending vs. Applied Electric Field

4.7 CONCLUSIONS

Induced strain actuation of two-dimensional plate structures is a generalization of induced strain actuation of one-dimensional structures. It has been demonstrated that the uniform strain and laminated plate models presented can be specialized to the one-dimensional uniform strain and Bernoulli-Euler models of the previous chapter. The laminated plate model is preferred because of its greater accuracy and wider applicability.

In order to solve realistic problems with distributed actuation and general boundary conditions, an energy formulation is necessary. Energy terms representing the influence of actuation strain appear in the potential energy expression. In an approximate Rayleigh-Ritz solution to a problem formulated in terms of energy, the actuation strain terms are included in the modal forcing.

An experiment using one cantilevered-free-free-free plate and surface-mounted PZT actuators was conducted. Using a ten-mode Rayleigh-Ritz model which included several discontinuous mode shapes, the tip deflection at the first bending resonance was predicted accurately. Approximate solution of the plate problem for arbitrarily distributed actuation and general boundary conditions is also possible.

CHAPTER FIVE: CONCLUSIONS AND RECOMMENDATIONS

Conclusions

Mechanical models of generalized induced strain actuation of one- and two-dimensional structures have been developed without reference to the specific actuation strain mechanism used. The actuation strain produced by one type of material, piezoceramics, has been characterized in greater depth.

The detailed characterization of piezoceramic actuation strain highlighted the "nonideal" features of that type of actuation strain. However, the presence of nonidealities does not cause piezoceramics to be viewed as actuators which are overly difficult to use. Instead, the recognition of realistic properties will reduce uncertainty and improve performance. The significant advantages of piezoceramic induced strain actuation, including a high bandwidth, and other advantages associated with all induced strain actuators, such as the development of intelligent structures, outweigh the relatively minor nonidealities presented here.

Based on tests conducted mainly for one type of PZT piezoceramic, several guidelines for the use of piezoceramics were established. The property of piezoelectricity is lost when a piezoceramic depoles. Therefore, steps can be taken to avoid high stresses and temperatures, and fields above the coercive field. When a piezoceramic is depoled, it is possible to repole it *in situ*.

The basic nonlinearity in the field-strain relation causes a strain larger than that predicted using the single strain constant, d_{31}. The use of a variable coefficient, d^*_{31}, which depends on induced strain, yields a more accurate representation.

The hysteresis present between field and strain can be reduced by careful material selection. For vibration problems, hysteresis can be mostly eliminated by use of charge control. In static problems, hysteresis is likely to be a greater concern.

Piezoelectric creep was found to be present. As a result of creep, d^*_{31} varied with frequency, but only by 15% over a four-decade frequency range, and

the variation was not detectable for frequencies over 100 Hz. The influence of creep is most important in static problems.

All nonidealities were reduced at low strain levels, which may be typical of stiffness-limited structures and precision actuation. A careful characterization of piezoceramic actuators is useful, and will aid in predicted performance of a complicated system employing piezoceramic induced stain actuation.

Three separate models of induced strain actuation for one-dimensional structures have been developed. The models are not limited to the use of piezoceramics as the actuation. The uniform strain model, adapted from Crawley and de Luis (1987), was found to be accurate in description of induced stretching, but inaccurate in description of induced bending, particularly for thin structures. Results for the Bernoulli-Euler model for generalized cross-sections, with embedded or surface-mounted actuators, were derived. Based on comparison with more detailed finite element models, and experiments, the Bernoulli-Euler bending model was judged to accurately predict extensional and bending deformations.

A series of static and dynamic experiments on two cantilevered-free beam specimens with surface-mounted actuators was conducted. The strain-dependent d^*_{31} was employed to accurately predict the induced strains and deflections. A Rayleigh-Ritz model was used in the prediction of dynamic amplitudes. Further, some evidence of a finite stiffness bonding layer, as well as piezoceramic creep and hysteresis was observed.

The finite element models highlighted the presence of material shear in the actuators and structure. The deviation in net displacement from the simple Bernoulli-Euler model was judged to be significant for shorter, thicker actuators, and for thick beams, where the influence of material shear was greatest. The influence of a finite bonding layer between the actuators and structure was characterized by a shear parameter, Γ. The deviation from the perfectly-bonded model was significant for shorter actuators, and for less stiff bonding layers. Based on these models it can be inferred that if Γ is greater than 20, and the length to thickness ratio of the actuator is greater than 100, the finite shear effects can be ignored, and the simple Bernoulli-Euler model accurately predicts the beam deformations.

Two-dimensional models of induced strain actuation were developed. The uniform strain plate model, applicable only to surface-mounted actuation, was shown to be a generalization of the one-dimensional model. Similarly, the laminated plate model, applicable to both surface-mounted and embedded actuation, specialized to the one-dimensional Bernoulli-Euler model. The laminated plate model is preferred for design because of its greater accuracy and ease of use. That model is consistent with an energy formulation of the plate problem including the effect of actuation strain. It was shown that in most practical problems, the energy formulation is required. Exact solutions to this problem are available only for a limited number of static problems.

An experiment was conducted to validate the basic model of two-dimensional induced strain actuation, as well as the approximate solution of the energy formulation. A Rayleigh-Ritz model, employing several mode shapes discontinuous in strain, provided an accurate prediction of dynamic test results. Based on the energy formulation, an accurate model can be developed for arbitrary boundary conditions and actuation distribution.

The use of actuation strain has been shown to be easily and accurately analyzed with simple models. Piezoceramic actuation strain was characterized in greater detail. A similar characterization of actuation strain due to phenomena other than piezoelectricity could also be carried out. The generalized induced strain actuation models developed in this study are valid for any type of actuation strain.

Recommendations

Since only a single type of PZT piezoceramic (Piezoelectric Products G-1195) was used in most of the experiments in this study, some characteristics which were measured may be present to a greater or lesser extent in other materials or compositions. Therefore, a broader, more complete study of different piezoceramic compositions is desirable.

In this study, piezoceramic actuation strain was characterized and used. There are several other sources of actuation strain. Detailed characterizations of electrostrictive and magnetostrictive materials, including measurement of other properties, such as temperature dependence and power consumption, for comparison with the piezoceramic characterization are recommended.

Although the nonlinearities found in piezoceramic actuation strain were not prohibitive, their presence is in general not preferred. The guidelines for addressing the "nonideal" properties presented in this study are only a first step. Development of comprehensive analytical modeling and electronic hardware strategies for linearizing piezoceramic actuation strain are therefore recommended.

The plate models presented are based on the standard plate theory for which analysis programs have been developed. Induced strain actuation should be viewed as part of the design of an intelligent structure, rather than an addition after design. Therefore, models of induced strain actuation should be integrated with a laminated plate analysis software package for use as a design tool

Although structural control was not directly addressed in this study, it is the objective for which induced strain actuation is designed. Further development of control formulations and strategies which make use of the unique properties of induced strain actuation is therefore recommended.

Finally, if induced strain actuation is integrated into structures, several unique long-term utility issues must be addressed. These include: strength, fatigue, and fracture of actuator materials; actuator degradation due to aging; the influence of embedded actuators on structural integrity and longevity; and implications of actuation performance changes for control design.

REFERENCES

Chapter 1

Berlincourt, D.A., Curran, D.R., and Jaffe, H., 1964, "Piezoelectric and Piezomagnetic Materials and Their Function in Transducers", *Physical Acoustics*, W. Mason, ed., Vol.1, Ch. 3.

Bryant, M.D. and Keltie, R.F., "A Characterization of the Linear and Nonlinear Dynamic Performance of a Practical Piezoelectric Actuator," *Sensors and Actuators*, 9(1986) pp. 95-114.

Burke, S., and Hubbard, J.E., 1987, "Active Vibration Control of a Simply-Supported Beam Using a Spatially-Distributed Actuator," *IEEE Control Systems Magazine*, Vol. 7, No. 6, 1987.

Butler, J.L., 1988, "Application Manual for Design of Magnetostrictive Transducers," Edge Technologies, Inc., Extrema Division, N. Marshfield, MA.

Crawley, E.F. and de Luis, J., 1987, "The Use of Piezoelectric Actuators as Elements of Intelligent Structures," *AIAA Journal*, Vol. 25, No. 10, Oct., 1987, AIAA Paper 86-0878.

Crawley, E.F., de Luis, J., Hagood, N.W., and Anderson, E.H., 1988, "Development of Piezoceramic Technology for Applications in Control of Intelligent Structures," presented at American Control Control Conference, Atlanta, June, 1988.

Cross, L.E., *et al.*, 1980, "Electrostrictive Behavior of Lead Magnesium Niobate -based Dielectrics," *Ferroelectrics*, 1980, Vol. 27.

Cross, L.E., *et al.*, 1987, "Piezoelectric and Electrostrictive Materials for Transducer Applications," Pennsylvania State University, University Park Materials Laboratory, 1985-1987.

de Luis, 1989, "Design and Implementation of Optimal Controllers for Intelligent Structures Using Infinite Order Structural Models," PhD Thesis, MIT, Cambridge, MA.

Edberg, D.L., 1987, "Control of Flexible Structures by Applied Thermal Gradients," AIAA Journal, Vol. 25, No. 6, June, 1987.

Fanson, J.L, and Caughey, T.K., 1987, "Positive Position Feedback Control for Large Space Structures, AIAA Paper 87-0902.

Forward, R.L., and Swigert, C.J., 1981, "Electronic Damping of Orthogonal Bending Modes in a Cylindrical Mast - Theory," *Journal of Spacecraft and Rockets*, Jan./Feb., 1981.

Hagood, N.W., and Crawley, E.F., 1988, "Development and Experimental Verification of Damping Enhancement Methodologies for Space Structures," Space Systems Laboratory Report, SSL 18-88, MIT, Cambridge, MA.

Hanagud, S., Obal, M.W., and Calise, A.J., 1987, "Optimal Vibration Control by the Use of Piezoceramic Sensors and Actuators," AIAA Paper 87-0959, Apr., 1987.

Jaffe, B., Cook, W.R., and Jaffe, H., 1971, *Piezoelctric Ceramics*, Academic Press, New York.

Martin, G.E., 1974, "Dielectric, Elastic, and Piezoelectric Losses in Piezoelectric Materials," *Proceedings of 1974 Ultrasonics Symposium*, Milwaukee, WI.

Newcomb, C.V. and Flinn, I., 1982, "Improving the Linearity of Piezoelectric Ceramic Actuators," *Electronics Letters*, Vol. 18, No.11, pp. 442-444.

Rogers, C.A., Liang, C., and Jia, J., 1989, "Behavior of Shape Memory Alloy Reinforced Composite Plates," AIAA Paper 89-1389.

Schetky, L., 1979, "Shape Memory Alloys," *Scientific American*, Vol. 241, 1979.

Shimizu, K., *et al.*, "Pseudoelasticity and Shape Memory Effects," *International Metals Review*, Vol. 31, No. 3, 1986, pp. 93-114.

Uchino, K., 1986, "Electrostrictive Actuators: Materials and Applications," American Ceramic Society Bulletin, Vol. 65, No. 4, April, 1986.

Chapter 2

Adam, Winfried, Tichy, Jan, and Kittinger, Erwin, 1988, "The Different Sets of Electrical, Mechanical, and Electromechanical Third-order Constants for Quartz," *J. Applied Physics*, 64(5), pp. 2556-2562.

Berlincourt, D.A., Curran, D.R., and Jaffe, H., 1964, "Piezoelectric and Piezomagnetic Materials and Their Function in Transducers", *Physical Acoustics*, W. Mason, ed., Vol.1, Ch. 3.

Bondarenko, A.A., Karas', N.I., and Ulitko, A.F., 1982, "Methods for Determining the Vibrational Dissipation Characteristics of Piezoceramic Structural Elements," Soviet Applied Mechanics, pp. 175-179.

Bryant, M.D. and Keltie, R.F., "A Characterization of the Linear and Nonlinear Dynamic Performance of a Practical Piezoelectric Actuator," *Sensors and Actuators*, 9(1986) pp. 95-114.

Cady, W.G., 1964, *Piezoelectricity*, Dover, New York.

Chen, P.J. and Montgomery, S.T., 1980, "A Macroscopic Theory for the Existence of the Hysteresis and Butterfly Loops in Ferroelectricity," *Ferroelectrics*, 23(1980), pp. 199-207.

Comstock, R.H., 1981, "Charge Control of Piezoelectric Actuators to Reduce Hysteresis Effects," U.S. Patent 4263527, Draper Laboratories, Cambridge, MA.

Crawley, E.F., Warkentin, D.J., and Lazarus, K.B., 1988, "Feasibility Analysis of Piezoelectric Devices," MIT Space Systems Laboratory Report 5-88, Cambridge, MA.

Crawley, E.F. and de Luis, J., 1987, "The Use of Piezoelectric Actuators as Elements of Intelligent Structures," *AIAA Journal*, Vol. 25, No. 10, AIAA Paper 86-0878.

de Luis, J. and Crawley, E.F., 1985, "The Use of Piezoceramics as Distributed Actuators in Flexible Space Structures," MIT Space Systems Laboratory Report 20-85, Cambridge, MA.

Doroshenko, V.A. and Ugryumova, M.A., 1978, "Influence of Strong Uniaxial and Biaxial Compression on the Properties of PZT-type Piezoelectric Ceramics," *Soviet Physics: Acoustics*, Vol. 24(4), pp. 345-346.

IEEE Std. 176-1978, *IEEE Standard on Piezoelectricity.*

Jaffe, B., Cook W.R., and Jaffe, H., 1971, *Piezoelectric Ceramics*, Academic Press, New York.

Jones, R. M., 1975, *Mechanics of Composite Materials*, Scripta, Wahington, D.C.

Lazarus, K.B., 1989, "Induced Strain Actuation of Anisotropic Plates," S.M. Thesis, MIT, Cambridge, MA.

Martin, G.E., 1974, "Dielectric, Elastic, and Piezoelectric Losses in Piezoelectric Materials," *Proceedings of 1974 Ultrasonics Symposium*, Milwaukee, WI.

Mason, W.P., 1950, *Piezoelectric Crystals and Their Application to Ultrasonics*, Van Nostrand, New York.

Newcomb, C.V. and Flinn, I., 1982, "Improving the Linearity of Piezoelectric Ceramic Actuators," *Electronics Letters*, Vol. 18, No.11, pp. 442-444.

Piezoelectric Products company literature, Cambridge, MA.

Smits, J. G., 1976, "Iterative Method for Accurate Determination of the Real and Imaginary Parts of the Materials Coefficients of Piezoelectric Ceramics," *IEEE Trans. on Sonics and Ultrasonics*, Vol. SU-23, No.6, pp. 393-402.

Spangler, R.L., 1989, "Piezoelectric Actuators for Helicopter Rotor Control," S.M. Thesis, MIT, Cambridge, MA.

Tiersten, H.F., 1969, *Linear Piezoelectric Plate Vibrations*, Plenum Press, New York.

Chapter 3

Crawley, E.F. and de Luis, J., 1987, "The Use of Piezoelectric Actuators as Elements of Intelligent Structures," *AIAA Journal*, Vol. 25, No. 10, AIAA Paper 86-0878.

de Luis, J. and Crawley, E.F., 1985, "The Use of Piezoceramics as Distributed Actuators in Flexible Space Structures," MIT Space Systems Laboratory Report 20-85, Cambridge, MA.

IEEE Std. 176-1978, *IEEE Standard on Piezoelectricity.*

Rivello, Robert, 1969, *Theory and Analysis of Flight Structures*, McGraw-Hill, New York.

Chapter 4

Crawley, E.F. and de Luis, J., 1987, "The Use of Piezoelectric Actuators as Elements of Intelligent Structures," *AIAA Journal*, Vol. 25, No. 10, AIAA Paper 86-0878.

de Luis, 1989, "Design and Implementation of Optimal Controllers for Intelligent Structures Using Infinite Order Structural Models," PhD Thesis, MIT, Cambridge, MA.

Jones, R. M., 1975, *Mechanics of Composite Materials*, Scripta, Wahington, D.C.

Lazarus, K.B., 1989, "Induced Strain Actuation of Anisotropic Plates," S.M. Thesis, MIT, Cambridge, MA.

Lee, C.K., and Moon, F.C., 1987, "Piezoelectric Laminates for Torsional and Bending Modal Control: Theory and Experiment," PhD dissertation, Cornell University.

Leissa, Arthur W., 1969, *Vibration of Plates*, NASA SP-160.

Timoshenko, S., and Woinowsky-Kreiger, 1959, Theory of Plates and Shells, McGraw Hill, New York.

Appendices

ANSI/IEEE Std. 180-1986, *IEEE Standard of Definitions of Primary Ferroelectric Terms.*

Berlincourt, D.A., Curran, D.R., and Jaffe, H., 1964, "Piezoelectric and Piezomagnetic Materials and Their Function in Transducers", *Physical Acoustics*, W. Mason, ed., Vol.1, Ch. 3.

Blevins, Robert D., 1979, *Formulas for Natural Frequency and Mode Shape*, Robert E. Krieger Publishing Company.

Hagood, N.W., and von Flotow, A., 1989, "Damping of Structural Vibrations with Piezoelectric Materials and Passive Electrical Networks," *Proceedings of Damping '89 Conference*, West Palm Beach, Feb. 1989.

IEEE Std. 176-1978, *IEEE Standard on Piezoelectricity.*

Mason, W.P., "An Electrical Representation of a Piezoelectric Crystal Used as a Tranducer," *Proceedings of the Institute of Radio Engineers*, Vol. 23, Number 10, Oct. 1935.

APPENDIX A: NOTE ON PIEZOELECTRIC TERMINOLOGY

The terms *piezoelectric, piezoceramic,* and *ferroelectric* are often used interchangeably and carelessly. Occasional confusion may result. As a means of clarification, the material hierarchy will be briefly outlined. Most of the terminology was developed for crystals, but the word material is inserted for generality.

The term piezoelectric is the broadest. In the linear theory, when an electric field is applied along certain directions in a piezoelectric material, the material is strained by an amount proportional to the applied field. A subgroup of piezoelectric materials are those which possess a nonvanishing electric dipole moment per unit volume and are therefore called *polar*.

Polar materials are *pyroelectric,* because of the "appearance of an electric charge at the surface of a polar material when uniform heating or cooling changes the polarization."* *Ferroelectrics* are a subgroup of the polar materials. They are therefore both pyroelectric and piezoelectric. A ferroelectric material "exhibits, over some range of temperature, a spontaneous electric *polarization that can be reversed or reoriented by the application of an electric field.*"* This distinguishes ferroelectrics from more general pyroelectrics. Ferroelectrics can lose that property at a temperature called the Curie Point.

A *ferroelectric ceramic* is a ferroelectric material in ceramic form. It is an aggregate of ferroelectric single crystal grains (sometimes called crystallites). The macroscopic properties of ceramics are significantly different from those of the constituent crystallites.

The materials used and analyzed in this study are most accurately termed ferroelectric ceramics. The term *piezoceramic,* however, is no less general, and, because of its common usage, is used throughout the text.

* ANSI/IEEE Std 180-1986, "IEEE Standard of Definitions of Primary Ferroelectric Terms"

APPENDIX B: IMPEDANCE AND ELECTRICAL MODELS

Equivalent impedance and electrical circuit models of piezoelectricity are based on electrical representation of the coupled electrical and mechanical problems. Often, an equivalent circuit model is used in resonant (and ultrasonic) applications. This type of model is consistent with the basic piezoelectric constitutive relations. It was first suggested by Mason (1935) and has been improved on and generalized many times since.

The origin of impedance and equivalent circuit models is best seen by a derivation of the models directly from the constitutive relations. This derivation makes use of the wave equation. The following is based on Berlincourt, *et al.* (1964) where the derivation is carried out for other piezoelectric coefficients (*e.g.* strain parallel to the applied electric field, d_{33}) as well.

For the case where the concern is with strain perpendicular to the applied field (*i.e.* d_{31}), the constitutive relations (Eq. 2.3) reduce to two equations

$$\begin{aligned} S_1 &= s_{11}^E T_1 + d_{31} E_3 \\ D_3 &= d_{31} T_1 + \varepsilon_{33}^T E_3 \end{aligned} \tag{B.1}$$

The one-dimensional wave equation is

$$\rho \frac{\partial^2 u}{\partial t^2} dx_1 dx_2 dx_3 = \frac{\partial T_1}{\partial x} dx_1 dx_2 dx_3 \tag{B.2}$$

where u is the displacement in the x_1 direction. From the first of Eqs. B.1, the stress may be rewritten

$$T_1 = \frac{1}{s_{11}^E} S_1 - \frac{d_{31}}{s_{11}^E} E_3 \tag{B.3}$$

where the strain is

$$S_1 = \frac{\partial u_1}{\partial x_1} \tag{B.4}$$

With the relations of Eqs. B.3 and B.4, Eq. B.2 may be rewritten

$$\rho \frac{\partial^2 u_1}{\partial t^2} = \frac{1}{s_{11}^E} \frac{\partial^2 u_1}{\partial x_1^2} - \frac{d_{31}}{s_{11}^E} \frac{\partial^2 E_3}{\partial x_1^2} \tag{B.5}$$

If it is assumed that the piezoelectric is covered by a single electrode, the electric field does not vary over the length, that is

$$\frac{\partial E_3}{\partial x_1} = 0 \tag{B.6}$$

so the wave equation reduces to

$$\frac{\partial^2 u_1}{\partial t^2} = \frac{1}{\rho s_{11}^E} \frac{\partial^2 u_1}{\partial x_1^2} = (v^E)^2 \frac{\partial^2 u_1}{\partial x_1^2} \tag{B.7}$$

where v^E is the velocity of the longitudinal traveling waves for constant electric field. If the electric field is assumed to be sinusoidal in time

$$E_3 = E_0 e^{j\omega t} \tag{B.8}$$

the solution for the displacement has the form

$$u_1 = \left(A \sin\left(\frac{\omega x_1}{v^E}\right) + B \cos\left(\frac{\omega x_1}{v^E}\right)\right) e^{j\omega t} \tag{B.9}$$

which requires two boundary conditions for solution. For a stress-free bar these are

$$T_1\Big|_{x=0} = 0 \qquad T_1\Big|_{x=l} = 0 \tag{B.10}$$

Placing Eqs. B.8 and B.9 into B.3 and applying Eq. B.10 gives solutions for the unknowns A and B, so the displacement u_1 is

$$u_1 = \frac{v^E}{\omega}\left[\sin\left(\frac{\omega x_1}{v^E}\right) + \frac{\left(\cos\left(\frac{\omega l}{v^E}\right) - 1\right)}{\sin\left(\frac{\omega l}{v^E}\right)}\cos\left(\frac{\omega x_1}{v^E}\right)\right] d_{31} E_0 e^{j\omega t} \tag{B.11}$$

In order to write the equivalent electrical impedance (or its inverse, the admittance) it is necessary to write expressions for the current and voltage. The admittance is then

$$\frac{1}{Z} = \frac{I}{V} = \frac{w\int_0^l \dot{D}_3 dx}{\int_0^t E_3 dz} \tag{B.12}$$

where w is the width of the bar and the electric displacement is

$$D_3 = \left\{\varepsilon_{33}^T\left(1 - k_{31}^2\right) + \varepsilon_{33}^T k_{31}^2\left[\cos\left(\frac{\omega x}{v^E}\right) - \frac{\left(\cos\left(\frac{\omega l}{v^E}\right) - 1\right)}{\sin\left(\frac{\omega l}{v^E}\right)}\sin\left(\frac{\omega x}{v^E}\right)\right]\right\} E_0 e^{j\omega t} \tag{B.13}$$

where the electromechanical coupling coefficient is defined as

$$k_{31}^2 = \frac{d_{31}^2}{s_{11}^E \varepsilon_{33}^T} \tag{B.14}$$

The admittance may then be simplified to

$$\frac{1}{Z} = j\omega \frac{lw}{t}\varepsilon_{33}^T\left\{\left(1 - k_{31}^2\right) + k_{31}^2 \frac{\tan\left(\frac{\omega l}{2v^E}\right)}{\left(\frac{\omega l}{2v^E}\right)}\right\} \tag{B.15}$$

For low frequencies ($\omega << l/v^E$) the second term can be ignored, and the impedance is

$$Z = \frac{t}{j\omega\varepsilon_{33}^T A} = \frac{1}{j\omega C^T} \tag{B.16}$$

which is just the equivalent (stress-free) impedance of a capacitor.

The basic equivalent circuit for a piezoelectric is apparent from the equations above. By solving for the unknowns A and B in Eq. B.9 in terms of the velocities, $\dot{u}_1$, and using Eq. B.1, the relevant mechanical and electrical quantities at the three (one electrical and two mechanical) terminal ports can be determined, for constant stress and constant field.

The equivalent circuit usually presented (first by Mason, 1935) is valid for an unloaded piezoelectric near a mechanical resonance. where N is the "turns ratio" of the electrical-to-mechanical transformer, and C_m, L_m and R_m, represent the electrical equivalent of the mechanical stiffness, mass, and damping. Electrical and mechanical boundary conditions can be applied at the two sides of the circuit. An alternate "lumped parameter equivalent circuit" does not include a transformer (Fig. B.2, IEEE Std. 176-1978). Additional *RLC* branches may be included for representation of closely spaced modes.

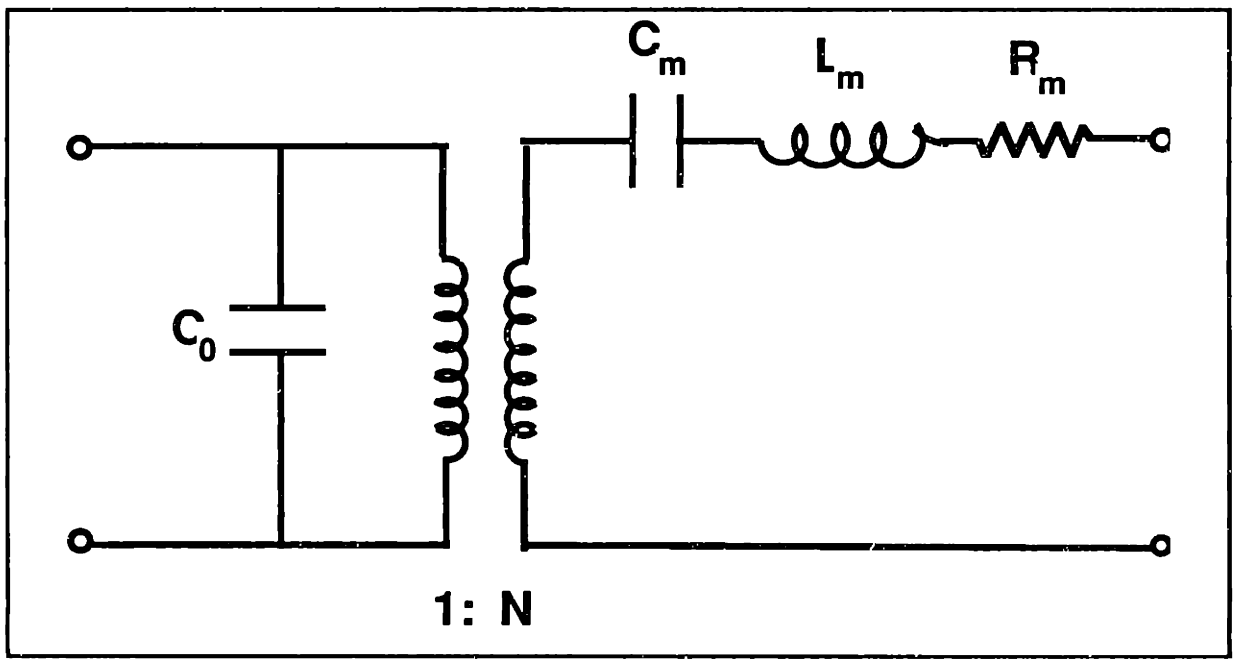

Figure B.1: Equivalent Circuit Model of Piezoelectric with Electromechanical Transformer Valid Near an Isolated Mechanical Resonance

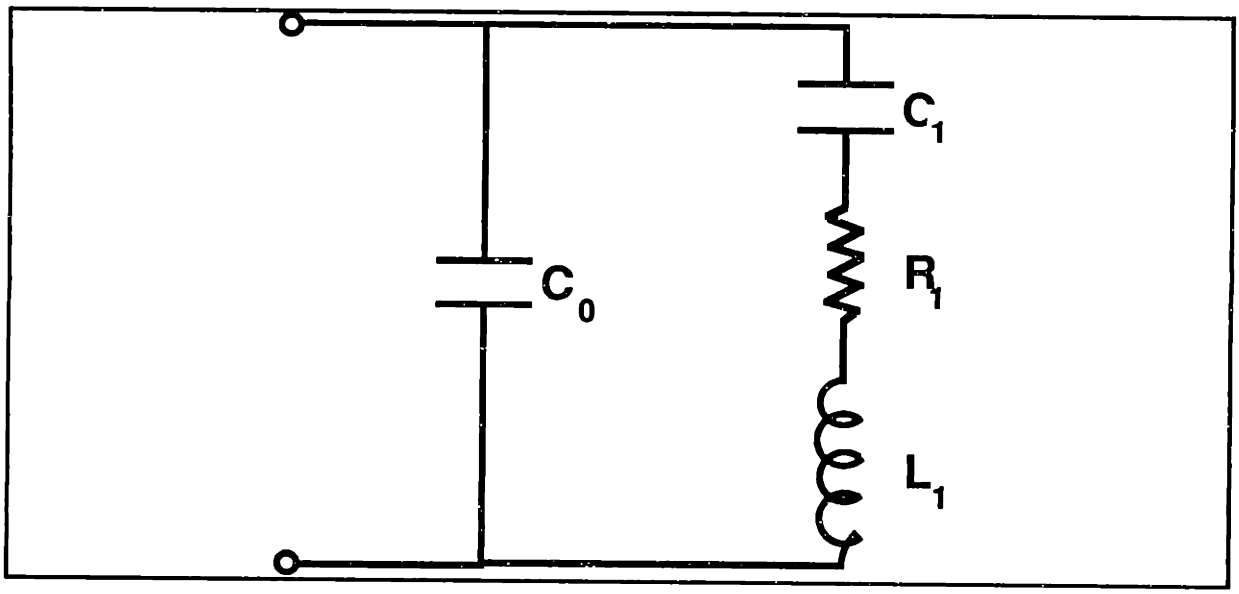

Figure B.2: Equivalent Circuit Model of Piezoelectric Valid Near an Isolated Mechanical Resonance

An even simpler electrical representation eliminates the mechanical part of the circuit. It was shown above (Eq. B.16) that this model is valid only at low frequencies.

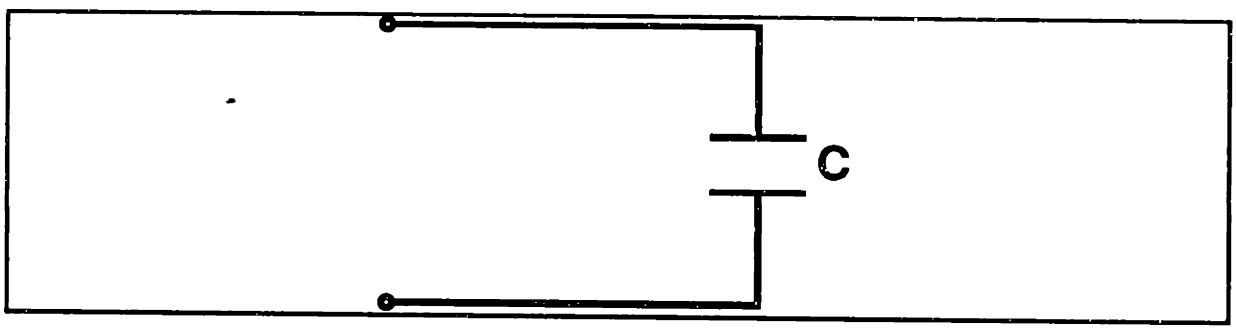

Figure B.3: Pure Capacitance Low Frequency Model of a Piezoelectric

This representation was used for prediction of passive damping of beams of the type in Section 3.6 when the piezoceramics provided a path for conversion from mechanical to electrical energy. When a resistor is shunted across the piezoelectric in Fig. B.4, energy may be dissipated in that resistor. To first order, when the resistance of the shunting resistor is equivalent to the impedance of the piezoceramic (Eq. B.16), the impedances are "matched" and the maximum energy is dissipated. Hagood and von Flotow (1989) contains a detailed analysis of both resistor and resistor plus inductor shunted structures utilizing piezoceramics.

APPENDIX C: PIEZOELECTRIC CONSTITUTIVE RELATIONS

In this appendix, the full tensor piezoelectric constitutive relations will be presented. The relations between mechanical, dielectric, and piezoelectric coefficients will be given. An example of the thermodynamic state form of the relations will be shown, and the importance of electrical and mechanical boundary conditions will be illustrated. In that illustration, the electromechanical coupling coefficient will be defined.

Piezoelectric Constitutive Relations

The full tensor piezoelectric constitutive relations can be written in the following four ways

$$\begin{aligned} D_i &= d_{ikl} T_{kl} + \varepsilon^T_{ik} E_k \\ S_{ij} &= s^E_{ijkl} T_{kl} + d_{kij} E_k \end{aligned} \tag{C.1}$$

$$\begin{aligned} D_i &= e_{ikl} S_{kl} + \varepsilon^S_{ik} E_k \\ T_{ij} &= c^E_{ijkl} S_{kl} - e_{kij} E_k \end{aligned} \tag{C.2}$$

$$\begin{aligned} E_i &= - g_{ikl} T_{kl} + \beta^T_{ik} D_k \\ S_{ij} &= s^D_{ijkl} T_{kl} + g_{kij} D_k \end{aligned} \tag{C.3}$$

$$\begin{aligned} E_i &= - h_{ikl} S_{kl} + \beta^S_{ik} D_k \\ T_{ij} &= c^D_{ijkl} S_{kl} - h_{kij} D_k \end{aligned} \tag{C.4}$$

where the coefficients are

E	Electric field	D	Electric displacement
S	Mechanical strain	T	Mechanical stress
c	Elastic stiffness	s	Elastic compliance
ε	Permittivity (dielectric coefficient)	β	Impermittivity

d,e,g,h Piezoelectric coefficients

and the superscripts refer to electrical and mechanical boundary conditions

$()^E$ constant electric field (closed or short circuit)
$()^D$ constant electric displacement (open circuit)
$()^T$ constant stress (free)
$()^S$ constant strain (clamped)

The relations used in Chapter 2 are the contracted notation for (C.1) above. That is

$$\begin{aligned} D_i &= d_{ij} T_j + \varepsilon_k^T E_k \\ S_i &= s_{ij}^E T_j + d_{kj} E_k \end{aligned} \tag{C.5}$$

The elastic, dielectric, and piezoelectric coefficients are not all defined independently. The definitions are given by the following relations

$$\begin{aligned} c_{pr}^E s_{qr}^E &= \delta_{pq} & c_{pr}^D s_{qr}^D &= \delta_{pq} \\ \beta_{ik}^S \varepsilon_{jk}^S &= \delta_{ij} & \beta_{ik}^T \varepsilon_{jk}^T &= \delta_{ij} \\ c_{pq}^D &= c_{pq}^E + e_{kp} h_{kq} & s_{pq}^D &= s_{pq}^E - d_{kp} g_{kq} \\ \varepsilon_{ij}^T &= \varepsilon_{ij}^S + d_{iq} e_{jq} & \beta_{ij}^T &= \beta_{ij}^S - g_{iq} h_{jq} \\ e_{ip} &= d_{iq} c_{qp}^E & h_{ip} &= g_{iq} c_{qp}^D \\ g_{ip} &= \beta_{ik}^T d_{kp} & d_{ip} &= \varepsilon_{ik}^T g_{kp} \end{aligned} \tag{C.6}$$

where δ is the Kroenecker delta.

Thermodynamic State Representation

The thermodynamic formulation of (C.5) is written

$$D = \left(\frac{\delta D}{\delta T}\right)_E T + \left(\frac{\delta D}{\delta E}\right)_T E$$
$$S = \left(\frac{\delta S}{\delta T}\right)_E T + \left(\frac{\delta S}{\delta E}\right)_T E \qquad \text{(C.7)}$$

The definition of d as the change in electric displacement with stress at constant field or the change in strain with field at constant stress is apparent in the way the relations are written. It is interesting to note that elastic modulus has the logical definition of change in strain per change in stress (for constant field here) when considered this way. The complete set of elastic, dielectric, and piezoelectric constants have similarly sensible definitions.

Electrical and Mechanical Boundary Conditions and the Electromechanical Coupling Coefficient

The relations between open-circuit and closed-circuit mechanical coefficients, and free and clamped electrical coefficients will be illustrated for actuation using d_{31}. The basic relations (C.5) for field applied in the x_3 direction inducing strain in the x_1 direction are

$$D_3 = d_{31} T_1 + \varepsilon_3^T E_3$$
$$S_1 = s_{11}^E T_1 + d_{31} E_3 \qquad \text{(C.8)}$$

If E_3 is eliminated from the upper equation and inserted in the lower one

$$S_1 = s_{11}^E T_1 + \frac{d_{31}}{\varepsilon_3^T}(D_3 - d_{31} T_1)$$
$$= s_{11}^E \left(1 - \frac{d_{31}^2}{\varepsilon_3^T s_{11}^E}\right) T_1 + g_{31} D_3 \qquad \text{(C.9)}$$

The transverse *electromechanical coupling factor* k_{31}, for a piezoelectric material is defined as

$$k_{31} = \frac{d_{31}}{\sqrt{\varepsilon_3^T s_{11}^E}} \tag{C.10}$$

In a similar manner, the longitudinal and shear coupling coefficients are

$$k_{33} = \frac{d_{33}}{\sqrt{\varepsilon_3^T s_{33}^E}} \tag{C.11}$$

$$k_{15} = \frac{d_{15}}{\sqrt{\varepsilon_1^T s_{55}^E}} \tag{C.12}$$

Making use of Eq. C.10, the strain can be written

$$S_1 = s_{11}^D T_1 + g_{31} D_3 \tag{C.13}$$

where the quantity multiplying the stress, T_1, is the open circuit compliance, s^D, which is related to the short-circuit compliance by

$$s_{11}^D = s_{11}^E \left(1 - k_{31}^2\right) \tag{C.14}$$

In a similar fashion it can be shown that

$$c_{11}^E = c_{11}^D \left(1 - k_{31}^2\right) \tag{C.15}$$

$$\varepsilon_3^S = \varepsilon_3^T \left(1 - k_{31}^2\right) \tag{C.16}$$

$$\beta_3^T = \beta_3^S \left(1 - k_{31}^2\right) \tag{C.17}$$

The value for k is different in each direction and also varies with frequency. A typical value for k_{31}, which couples electrical energy in the x_3 direction to inplane mechanical energy is 0.3. This means, for example, that a piezoceramic is roughly 10% stiffer when its electrodes are not electrically connected, compared to when they are short-circuited.

APPENDIX D: MANUFACTURER'S SPECIFICATIONS FOR G-1195

Free dielectric constants	$\varepsilon_{33}^{T}/\varepsilon_{0}$	1700
	$\varepsilon_{11}^{T}/\varepsilon_{0}$	1700
Dielectric loss tangent	$\tan(\delta)$	.015
Density	ρ	7650 kg/m^3
Curie Temperature	T_c	360 C
Piezoelectric strain constants	d_{33}	360 pm/V
	d_{31}	-180 pm/V
	d_{15}	540 pm/V
Young's moduli	c_{33}^{E}	49 GPa
	c_{11}^{E}	63 GPa
	c_{55}^{E}	22 GPa
Tensile strength	F_{tu}	77 MPa
Compressive strength	F_{cu}	> 500 MPa
Coercive Field (60 Hz)	E_c	1200 V/mm

APPENDIX E: EXACT CANTILEVERED-FREE BEAM MODE SHAPES

The first five exact cantilevered-free beam modes were used in Rayleigh-Ritz analyses in Chapters 3 and 4. The mode shapes are represented analytically by

$$\phi\left(\tfrac{x}{L}\right) = \cosh\left(\lambda_i \tfrac{x}{L}\right) - \cos\left(\lambda_i \tfrac{x}{L}\right) - \mu_i\left(\sinh\left(\lambda_i \tfrac{x}{L}\right) - \sin\left(\lambda_i \tfrac{x}{L}\right)\right) \qquad \text{(E.1)}$$

where the coefficients λ_i and μ_i are given by (Blevins, 1979)

Table E.1: Cantilevered-Free Mode Shape Parameters

Mode Number	λ_i	μ_i
1	1.87510407	0.734095514
2	4.69409113	1.018467319
3	7.85475744	0.999224497
4	10.99554073	1.000033553
5	14.13716839	0.999998550
$i > 5$	$(2i - 1)\frac{\pi}{2}$	≈ 1.0

The natural frequencies (in Hertz) are

$$f_i = \frac{\lambda_i^2}{2\pi L^2}\sqrt{\frac{EI}{m}} \qquad \text{(E.2)}$$

where m is the mass per unit length, E is the Young's modulus, I is the area moment of inertia of the beam about its neutral axis, and L is the length of the beam.